

NEW TECHNIQUES IN DYNAMIC ANALYSIS OF STRUCTURES: SPECTRAL
ELEMENT METHOD, TRAVELLING WAVE METHOD AND ENERGY FLUX

by

Nilgün Merve Çağlar

B.S., Civil Engineering, Istanbul Technical University, 2010

M.S., Structural Engineering, Istanbul Technical University, 2014

Submitted to the Kandilli Observatory and
Earthquake Research Institute in partial fulfillment of
the requirements for the degree of
Doctor of Philosophy

Graduate Program in Earthquake Engineering
Boğaziçi University

2018

NEW TECHNIQUES IN DYNAMIC ANALYSIS OF STRUCTURES: SPECTRAL
ELEMENT METHOD, TRAVELLING WAVE METHOD AND ENERGY FLUX

APPROVED BY:

Prof. Dr. Erdal Şafak
(Thesis Supervisor)

Prof. Dr. Sinan Akkar

Prof. Dr. Ayşe Edinçliler

Prof. Dr. Kadir Güler

Assoc. Prof. Dr. Abdullah Necmettin Gündüz

DATE OF APPROVAL: 05.07.2018

ACKNOWLEDGEMENTS

First and foremost I would like to express my sincere gratitude to my supervisor, Prof. Dr. Erdal Şafak for guiding and supporting me over the years. He has set an example of excellence as a researcher, mentor, instructor, and role model. He consistently allowed this paper to be my own study but steered me in the right direction whenever he thought I needed it.

I would especially like to thank my amazing parents Nesrin and Zeki Çağlar, my sister Özge Çağlar Yılmaz for providing me with unfailing support and continuous encouragement throughout my years of study and through the process of researching and writing this thesis. Many thanks to my little nephew, Ayaz Yılmaz, for cheering me up all the time from the day he came into my life.

Finally, I would like to thank and dedicate this thesis to my grandfather, Fahri İnce. It was him who was there for me whenever I needed. Although it has been years since you have passed, I still take your lessons with me, every day.

ABSTRACT

NEW TECHNIQUES IN DYNAMIC ANALYSIS OF STRUCTURES: SPECTRAL ELEMENT METHOD, TRAVELLING WAVE METHOD AND ENERGY FLUX

The Spectral Element Method (SEM), Travelling Wave Method (TWM), and the Energy Flux are robust techniques to calculate the dynamic response of the structures, which are all based on the exact solution of the governing differential equations. In the formulation of these methods, either elementary or higher order element theories can be adopted. Since they use the exact solution, the inertia terms are implemented properly. An element without any discontinuity can be modeled as a single element. Thus, the number of degrees of freedoms (DOFs) decreases considerably, providing significant reduction in the problem size and the computation time. High-frequency wave modes, which are the modes more sensitive to small changes in the dynamic characteristics of the structure, can be captured more accurately with these methods. The matrix equations for the dynamic response of two and three-dimensional structures can easily be formed by assembling the element response matrices derived from the SEM, TWM and Energy Flux approach. All the formulations are given in frequency domain. Therefore, damping and SSI (Soil-Structure Interaction) effects can be incorporated more accurately, because many element-level damping properties and foundation impedance functions are frequency dependent. The propagation path of the disturbance within the structure, as well as the dissipated and reflected waves and energies can be tracked. This gives more insight into the dynamic behavior and the energy absorption capacity of the structure. Since they are very accurate in high frequencies, these methods also provide more powerful tools for system identification and damage detection. Most of the small and invisible damages in structures are hidden in high frequencies.

ÖZET

YAPILARIN DİNAMİK ANALİZİ İÇİN YENİ YÖNTEMLER: SPEKTRAL ELEMAN METODU, YÜRÜYEN DALGA METODU VE ENERJİ AKISI

Spektral Eleman Metodu (Spectral Element Method (SEM)), Yürüyen Dalga Metodu (Travelling Wave Method (TWM)) ve Enerji Akısı (Energy Flux), yapıların dinamik davranışı ve dinamik özelliklerinin belirlenmesi için kullanılacak, diferansiyel denklemin kesin çözümüne dayalı yöntemlerdir. Bu yöntemler hem basit hem de yüksek mertebeli eleman teorileri kullanılarak formülize edilebilmektedir. Söz konusu yöntemlerde, diferansiyel denklemin kesin çözümü kullanıldığından dolayı, atalet kuvvetleri uygun şekilde tanımlanabilmektedir. Herhangi bir süreksizliğin olmadığı elemanlar, yekpare olarak modellenenir. Bu sayede, tanımlanan serbestlik derecelerinin sayısı ve analiz süresi önemli derecede azalmaktadır. Yapının dinamik karakteristiğindeki değişimlere daha duyarlı olan yüksek frekanslı dalga modları, bu yöntemler ile elde edilebilmektedir. İki ve üç boyutlu yapıları oluşturan elemanlar, SEM, TWM ve Enerji Akısı analizlerindeki matris birleştirme prosedürünün geçerliliği ile kolayca birleştirilebilmektedir. Birçok sönümleme özelliğinin frekansa bağlı olmasından dolayı yapısal sönüm, bu yöntemler kullanılarak daha doğru olarak modellenenir. Yapı Zemin Etkileşimi (SSI) de yukarıda bahsedilen yöntemler ile uygulanabilmektedir. Zeminin rijitlik ve sönüm özelliklerini yansıtan Temel Empedans Fonksiyonlarının (Foundation Impedance Functions (FIF)) frekansa bağlı olmasından dolayı, frekans alanında oldukça etkili olan SEM, TWM ve Enerji Akısı yöntemleri, Yapı Zemin Etkileşimi analizlerinde daha kullanışlı olmaktadır. TWM ve Enerji Akısı yöntemleri kullanılarak yapıya uygulanan etkinin yapı içerisindeki yayılımı takip edilebilmektedir. Bu sayede, sönümlenen, yansıyan ve komşu elemana iletilen dalganın/enerji akısının oranı ve yapının dinamik özelliklerine ait detaylı bilgi elde edilebilmektedir.

TABLE OF CONTENTS

ACKNOWLEDGEMENTS	iii
ABSTRACT	iv
ÖZET	v
LIST OF FIGURES	viii
LIST OF SYMBOLS	xv
LIST OF ACRONYMS/ABBREVIATIONS	xx
1. INTRODUCTION	1
2. FORMULATION OF GOVERNING DIFFERENTIAL EQUATIONS OF MOTION	4
2.1. Rod Theories	5
2.1.1. Elementary Rod Theory	6
2.1.2. Love Rod Theory	7
2.1.3. Mindlin-Herrmann Rod Theory	8
2.1.4. Three-Mode Rod Theory	9
2.2. Beam Theories	11
2.2.1. Bernoulli-Euler Beam Theory	12
2.2.2. Timoshenko Beam Theory	13
3. SPECTRAL ELEMENT METHOD	15
3.1. Spectral Element for Rod Elements	17
3.1.1. Elementary Rod Theory	19
3.1.2. Love Rod Theory	20
3.1.3. Mindlin-Herrmann Rod Theory	21
3.1.4. Three-Mode Rod Theory	22
3.1.5. Comparison of the Rod Theories	24
3.2. Spectral Element for Beam Elements	28
3.2.1. Bernoulli-Euler Beam Theory	29
3.2.2. Timoshenko Beam Theory	31
3.2.3. Comparison of the Beam Theories	32
3.3. Assemblage of Spectral Element Matrices	36

3.4. Numerical Example	39
4. TRAVELLING WAVE METHOD	47
4.1. Longitudinal Wave Propagation	49
4.1.1. Elementary Rod Theory	49
4.1.2. Love Rod Theory	50
4.1.3. Mindlin-Herrmann Rod Theory	50
4.1.4. Three-Mode Rod Theory	51
4.2. Flexural Wave Propagation	52
4.2.1. Bernoulli-Euler Beam Theory	53
4.2.2. Timoshenko Beam Theory	53
4.3. Evaluation of Scattering and Generation Matrices	54
4.4. Assemblage of Waveguides	57
4.5. Numerical Example	59
5. ENERGY FLUX	65
5.1. Transmission and Reflection Coefficients	66
5.2. Input Energy Flux	84
5.3. Assemblage Procedure	84
6. SOIL STRUCTURE INTERACTION	87
6.1. Coupling the Soil and the Structure	89
6.2. Numerical Examples	91
7. CONCLUSIONS	98
REFERENCES	100

LIST OF FIGURES

Figure 2.1.	Properties of a rod element and forces acting on a segment of a rod.	5
Figure 2.2.	Properties of a beam element and forces acting on a segment of a beam.	11
Figure 3.1.	General procedure for SEM.	17
Figure 3.2.	Exact displacements and traction distributions on a cross section [12].	18
Figure 3.3.	Spectrum relation for Elementary, Love, Mindlin-Herrmann and Three-mode rod theories.	26
Figure 3.4.	Dispersion relationship for elementary, Love, Mindlin-Herrmann and Three-mode rod theories.	27
Figure 3.5.	k_{11} values according to conventional, theoretical, Elementary, Love and Mindlin-Herrmann rod theories.	28
Figure 3.6.	Exact displacements and traction distributions on a cross section [12].	29
Figure 3.7.	Spectrum relationship for Bernoulli-Euler and Timoshenko beam theories.	33
Figure 3.8.	Dispersion relationship for Bernoulli-Euler and Timoshenko beam theories.	34

Figure 3.9.	k_{11} values according to conventional, theoretical, Bernoulli-Euler and Timoshenko beam theories.	35
Figure 3.10.	Time domain representation of applied base acceleration.	39
Figure 3.11.	Frequency domain representation of applied base acceleration.	40
Figure 3.12.	Geometry and DOFs numbers of the example structure.	41
Figure 3.13.	FAS of the response at DOF= 52 between 0-50 Hz.	41
Figure 3.14.	FAS of the response at DOFs 50 between 0-10 Hz.	42
Figure 3.15.	FAS of the response at DOF= 52 between 10-15 Hz.	42
Figure 3.16.	FAS of the response at DOF= 52 between 15-20 Hz.	43
Figure 3.17.	Band pass filtered between 0.1-5 Hz. time domain response at DOF= 52 between 5-20 sec.	44
Figure 3.18.	Band pass filtered between 15-20 Hz. time domain response at DOF= 52 between 5-20 sec.	44
Figure 3.19.	Variation in base shear with respect to time (between 8-17 sec.).	45
Figure 3.20.	Variation in base shear with respect to time (between 17-26 sec.).	45
Figure 3.21.	Variation in base shear with respect to time (between 26-35 sec.).	46
Figure 3.22.	Variation in base shear with respect to time (between 35-44 sec.).	46

Figure 4.1.	General procedure for TWM.	49
Figure 4.2.	Sample joint.	55
Figure 4.3.	Travelling waves through an element.	58
Figure 4.4.	FAS of the response at DOF= 52 between 0-50 Hz.	60
Figure 4.5.	FAS of the response at DOF= 52 between 0-10 Hz.	61
Figure 4.6.	FAS of the response at DOF= 52 between 10-15 Hz.	61
Figure 4.7.	FAS of the response at DOF= 52 between 15-20 Hz.	62
Figure 4.8.	Band pass filtered between 0.1-5 Hz. time domain response at DOF= 52 between 5-20 sec.	62
Figure 4.9.	Band pass filtered between 15-20 Hz. time domain response at DOF= 52 between 5-20 sec.	63
Figure 4.10.	Variation in base shear with respect to time (between 8-17 sec.). .	63
Figure 4.11.	Variation in base shear with respect to time (between 17-26 sec.).	64
Figure 4.12.	Variation in base shear with respect to time (between 26-35 sec.).	64
Figure 5.1.	Energy flux between collinear rods.	67
Figure 5.2.	Energy flux between collinear beams.	68
Figure 5.3.	Reflected and transmitted waves at an L joint.	72

Figure 5.4.	Absolute value of the real part of the reflection and transmission coefficients of longitudinal energy flux at an L joint (undamped case).	73
Figure 5.5.	Absolute value of the real part of the reflection and transmission coefficients of far-field energy flux at an L joint (undamped case).	73
Figure 5.6.	Absolute value of the real part of the reflection and transmission coefficients of near-field energy flux at an L joint (undamped case).	74
Figure 5.7.	Absolute value of the real part of the reflection and transmission coefficients of longitudinal energy flux at an L joint (damped case).	75
Figure 5.8.	Absolute value of the real part of the reflection and transmission coefficients of far-field energy flux at an L joint (damped case).	75
Figure 5.9.	Absolute value of the real part of the reflection and transmission coefficients of near-field energy flux at an L joint (damped case).	76
Figure 5.10.	Transmitted and reflected waves at a T joint corresponding to the incident wave from the first element.	76
Figure 5.11.	Absolute value of the real part of the reflection and transmission coefficients of longitudinal energy flux at a T joint (undamped case).	77
Figure 5.12.	Absolute value of the real part of the reflection and transmission coefficients of far-field energy flux at a T joint (undamped case).	77
Figure 5.13.	Absolute value of the real part of the reflection and transmission coefficients of near-field energy flux at a T joint (undamped case).	78

Figure 5.14.	Absolute value of the real part of the reflection and transmission coefficients of longitudinal energy flux at a T joint (damped case).	79
Figure 5.15.	Absolute value of the real part of the reflection and transmission coefficients of far-field energy flux at a T joint (damped case).	79
Figure 5.16.	Absolute value of the real part of the reflection and transmission coefficients of near-field energy flux at a T joint (damped case).	80
Figure 5.17.	Transmitted and reflected waves at a cross joint corresponding to the incident wave from the first element.	80
Figure 5.18.	Absolute value of the real part of the reflection and transmission coefficients of longitudinal energy flux at a cross joint (undamped case).	81
Figure 5.19.	Absolute value of the real part of the reflection and transmission coefficients of far-field energy flux a cross joint (undamped case).	81
Figure 5.20.	Absolute value of the real part of the reflection and transmission coefficients of near-field energy flux at a cross joint (undamped case).	82
Figure 5.21.	Absolute value of the real part of the reflection and transmission coefficients of longitudinal energy flux at a cross joint (damped case).	82
Figure 5.22.	Absolute value of the real part of the reflection and transmission coefficients of far-field energy flux at a cross joint (damped case).	83
Figure 5.23.	Absolute value of the real part of the reflection and transmission coefficients of near-field energy flux at a cross joint (damped case).	83

Figure 5.24.	Energy flux through an element.	85
Figure 6.1.	Normalized stiffness terms.	89
Figure 6.2.	Normalized damping terms.	89
Figure 6.3.	Representation of soil-structure system.	90
Figure 6.4.	Frequency domain response at DOF= 52 calculated from the first SEM model with and without considering SSI.	92
Figure 6.5.	Frequency domain response at DOF= 52 calculated from the second SEM model with and without considering SSI.	92
Figure 6.6.	Time domain response at DOF= 52 calculated from the first SEM model with and without considering SSI.	93
Figure 6.7.	Time domain response at DOF= 52 calculated from the second SEM model with and without considering SSI.	93
Figure 6.8.	Base shear in the time domain calculated from the first SEM model with and without considering SSI.	94
Figure 6.9.	Base shear in the time domain calculated from the second SEM model with and without considering SSI.	94
Figure 6.10.	Frequency domain response at DOF= 52 calculated from the first TWM model with and without considering SSI.	95
Figure 6.11.	Frequency domain response at DOF= 52 calculated from the second TWM model with and without considering SSI.	95

Figure 6.12. Time domain response at DOF= 52 calculated from the first TWM model with and without considering SSI. 96

Figure 6.13. Time domain response at DOF= 52 calculated from the second TWM model with and without considering SSI. 96



LIST OF SYMBOLS

A	Area of the section
a_0	Dimensionless frequency
B	Half-width of the foundation
c	Phase velocity
c_g	Group velocity
C_i	Constant related to the i^{th} mode
C_j, K_{j2}	Radiation damping coefficient
\mathbf{d}_i	Part of system of waveguide equation, which relates incoming wave amplitudes to generalized displacements
\mathbf{d}_o	Part of system of waveguide equation, which relates outgoing wave amplitudes to generalized displacements
E	Young's modulus of the material
E_d	Complex Young's modulus
\mathbf{EF}_{in}	Input energy flux
F	Resultant in the longitudinal direction
\mathbf{F}	Generalized force vector
\mathbf{f}_i	Part of system of waveguide equation, which relates incoming wave amplitudes to generalized forces
\mathbf{f}_o	Part of system of waveguide equation, which relates outgoing wave amplitudes to generalized forces
\hat{F}	Spectral representation of resultant in the longitudinal direction
$\hat{\mathbf{F}}_k$	Vector of known resultants at member ends
$\hat{\mathbf{F}}_u$	Vector of unknown resultants at member ends
\hat{F}_1, \hat{F}_2	Spectral representation of the resultant in the longitudinal direction at member ends
\tilde{F}	Wave domain representation of resultant in the longitudinal direction
G	Shear modulus of the material
\mathbf{G}	Generation matrix

$\hat{g}_{B1}(x), \dots, \hat{g}_{B4}(x)$	Spectral representation of the shape functions related to the beam element
$\hat{g}_{R1}(x), \hat{g}_{R2}(x)$	Spectral representation of the shape functions related to the rod element
h	Height of the element
I	Second moment of inertia
\mathbf{I}	Identity matrix
J	Polar moment of area
\mathbf{K}	Stiffness matrix
k_B	Wavenumber related to the adopted beam theory
K_h	Impedance function in the longitudinal direction
K_{hr}	Coupling term of the impedance function
$k_i(\omega)$	Wavenumber related to the i^{th} mode
K_j, K_{j1}	Frequency dependent dynamic stiffness
k_R	Wavenumber related to the adopted rod theory
K_r	Impedance function for rocking
K_{sj}	Static stiffness
K_v	Impedance function in the vertical direction
K_1, K_2	Adjustable parameters
$\hat{\mathbf{K}}$	Spectral element matrix in local coordinates
$\hat{\mathbf{K}}_g$	Spectral element matrix in global coordinates
L	Length of the member
\mathcal{L}	Differential operator
M	Resultant moment
\mathcal{M}	Inertial operator
\hat{M}	Spectral representation of resultant moment
\tilde{M}	Wave domain representation of resultant moment
\hat{M}_1, \hat{M}_2	Spectral representation of the resultant moment at member ends
\mathbf{P}	Permutation matrix
\mathbf{P}_{EF}	Permutation matrix of energy flux
\mathbf{Q}	Prescribed force vector

q_v	Distributed transverse load
$q(x, t)$	externally applied body force per unit volume
q_ϕ	Distributed torque
\hat{q}	Spectral representation of externally applied body force
\hat{Q}	Spectral representation of resultant due to Poisson's effect
\tilde{Q}	Wave domain representation of resultant due to Poisson's effect
r	Distance from the centroid of the cross section
$\mathbf{r}_{\mathbf{EF}ij}$	Reflection matrix of energy flux
R_i	Amplitude ratios
\mathbf{r}_{ij}	Reflection matrix
\mathbf{S}	Scattering matrix
$\mathbf{S}_{\mathbf{EF}}$	Scattering matrix of energy flux
\mathbf{ST}	System transmission matrix
$\mathbf{ST}_{\mathbf{EF}}$	System transmission matrix of energy flux
\hat{S}	Spectral representation of resultant due to parabolic distribution of the longitudinal displacement
\tilde{S}	Wave domain representation of resultant due to parabolic distribution of the longitudinal displacement
T	Kinetic energy
\mathbf{T}	Rotation matrix
$\mathbf{t}_{\mathbf{EF}ij}$	Transmission matrix of energy flux
\mathbf{t}_{ij}	Transmission matrix
U	Potential energy
\mathbf{U}	Generalized displacement vector
\mathbf{u}_i	Vector of incoming wave amplitudes
\mathbf{u}_o	Vector of outgoing wave amplitudes
\mathbf{u}_R	Vector of right propagating wave amplitudes
\mathbf{u}_L	Vector of left propagating wave amplitudes
u_R	Amplitude of right propagating longitudinal wave
u_L	Amplitude of left propagating longitudinal wave
$\tilde{u}(x)$	Wave domain representation of longitudinal displacement

\mathbf{U}_{EFi}	Vector of amplitudes of incoming energy flux
\mathbf{U}_{EFo}	Vector of amplitudes of outgoing energy flux
$\mathbf{U}_{\text{EFnet}}$	Vector of amplitudes of net energy flux
U_{FFM}	Translational component of the free field motion
U_{FIM}	Translational component of the foundation input motion
$u(x, t)$	Displacement in the longitudinal direction
\dot{u}	First derivative of longitudinal displacement with respect to time
\ddot{u}	Second derivative of longitudinal displacement with respect to time
\dot{u}_T	Transverse velocity
$\hat{\mathbf{u}}_{\mathbf{k}}$	Vector of known displacements at member ends
\hat{u}_n	Spatially dependent Fourier coefficient
$\hat{\mathbf{u}}_{\mathbf{u}}$	Vector of unknown displacements at member ends
\hat{u}_1, \hat{u}_2	Spectral representation of the longitudinal displacement at member ends
$\bar{u}(x, y)$	Deformation field in the longitudinal direction
V	Resultant in the transverse direction
$v(x, t)$	Displacement in the transverse direction
V_s	Shear wave velocity
\dot{v}	First derivative of transverse displacement with respect to time
\hat{V}	Spectral representation of resultant in the transverse direction
\tilde{V}	Wave domain representation of resultant in the transverse direction
$\tilde{v}(x)$	Wave domain representation of transverse displacement
$\bar{v}(x, y)$	Deformation field in the transverse direction
\hat{V}_1, \hat{V}_2	Spectral representation of the resultant in the transverse direction at member ends
α	Vector of support conditions
β	Vector of displacement boundary conditions
γ_{xy}	Shear strain
δ	Prescribed displacement vector

Δx	Infinitesimally small segment
ε_T	Transverse strain
$\varepsilon_{xx}, \varepsilon_{yy}$	Axial strain
ζ	Damping ratio
λ, μ	Lamé constants
ν	Poisson's ratio
ρ	Mass density per unit volume
σ_{xx}, σ_{yy}	Axial stress
τ_{xy}	Shear stress
ϕ_{FIM}	Rotational component of the foundation input motion
$\phi(x)$	Parabolic distribution of the axial displacement, Slope of the section
$\dot{\phi}$	First derivative of the slope of the section with respect to time
$\hat{\phi}$	Spectral representation of parabolic distribution of the axial displacement, Spectral representation of the slope of the section
$\tilde{\phi}$	Wave domain representation of parabolic distribution of the axial displacement, Wave domain representation of the slope of the section
$\psi(x)$	Vertical contraction
$\dot{\psi}$	First derivative of vertical contraction with respect to time
$\hat{\psi}$	Spectral representation of vertical contraction
$\tilde{\psi}(x)$	Wave domain representation of vertical contraction
ω_c	Cut-off frequency
ω_n	Circular frequency related to the n^{th} mode

LIST OF ACRONYMS/ABBREVIATIONS

DFT	Discrete Fourier Transformation
DOFs	Degrees of Freedoms
FAS	Fourier Amplitude Spectra
FEM	Finite Element Method
FIF	Foundation Impedance Functions
GDEM	Governing Differential Equation Motion
SEM	Spectral Element Method
SSI	Soil-Structure Interaction
TWM	Travelling Wave Method

1. INTRODUCTION

Traditionally, Finite Element Method (FEM) is utilized to carry out dynamic analysis of structures. However, in medium to high frequency range, FEM does not able to capture the dynamic response accurately. FEM is formulated based on the frequency independent shape functions, which are obtained from the weak form of the governing differential equations and the inertial loads are concentrated at member ends. In order to improve the accuracy of the response in FEM, the mesh size used in the modeling must be smaller than the shortest wavelength. In other words, the response at frequencies with wavelengths that are smaller than the mesh size (i.e., high frequencies) cannot be calculated accurately. Therefore, to account for such high frequency responses, the number of elements and the number of the degrees of freedoms (DOFs) in the FEM model should be increased substantially.

Spectral Element Method (SEM) is a robust and alternative method to FEM for calculating the dynamic response and identifying the dynamic characteristics of engineering structures. SEM is formulated based on the frequency dependent shape functions, which are determined from the exact solution of the differential equation of an element. In literature, it is referred as the exact method, as it uses the exact solutions to the wave equations and considers inertial forces directly [1]. Since each component of the structure is seen as a waveguide and can be assembled using a matrix analogy to FEM, complex structures can be handled. Unlike the conventional FEM, high-frequency wave modes, which are the modes more sensitive to small changes in the dynamic characteristics of the structure, can be captured without dividing elements into small sized segments. Thus, the number of elements and the number of DOFs are decreased substantially [2].

Travelling Wave Method (TWM) also yields accurate results in medium to high frequency range, and the propagation path of the disturbance can be tracked. In contrast to SEM, base excitation can be applied without making any assumptions since the boundary conditions can be directly imposed into the system of equation in

wave propagation solutions.

Energy flux is a dynamic measure of energy, which is defined as the kinetic energy due to seismic shaking multiplied by the propagation velocity of seismic waves. It gives the amount of seismic energy transmitted per unit time through a cross-section of a medium [3]. In this manner, characteristics of energy flow and dissipation throughout the structure with respect to frequency can be obtained. Energy flux propagates as the waves travel through the waveguides. As in the wave propagation formulation, at the discontinuities, some portion of the incident energy transmitted into the adjacent members and some part is reflected. The reflection and transmission coefficients for the energy flux are independent of the direction of the propagation. The sum of the reflected and transmitted energy flux is equal to the incident energy flux due to the principle of conservation of energy.

Another advantage of SEM, TWM and Energy Flux is that Soil-Structure Interaction (SSI) effects can easily be incorporated in the analysis. SSI represents the influence of soil flexibility around the foundation on the response of a structure, and can change the dynamic response substantially [4]. It is a critical factor controlling damage during earthquakes. SSI must be considered in the analysis of structures founded on soft soils. Foundation Impedance Functions (FIF), which represent the stiffness and damping properties of the soil-foundation system, are frequency dependent. Although, impedance functions can be approximated in time domain in the form of recursive filters [4], it is much easier to incorporate them in the frequency domain directly in SEM analysis.

This thesis covers the applications of the SEM and TWM approaches in dynamic analysis of the plane frame structures with and without considering soil structure interaction. Additionally, Energy Flux approach is introduced as an alternative methodology that can be used in the dynamic analysis of engineering structures.

The second chapter presents a brief information about the techniques that are used to develop the governing differential equations of the motion (GDEM) of the

elements. Afterwards, GDEM for one dimensional elements based on various theories with different complexities are derived. These equations are used in the following three chapters.

Third chapter introduces derivation of spectral element matrices of one dimensional elements according to the Fourier based SEM. This chapter also covers a literature survey on SEM and the procedure for assembling spectral element matrices of arbitrary oriented members. A numerical example is presented, which compares the dynamic response of a plane frame structure calculated from SEM and FEM.

The TWM is presented in the fourth chapter. The method and the previous studies are briefly outlined. A general procedure to derive propagation, reflection and transmission relations, which allows to adopt various engineering theories for one dimensional elements is presented. A numerical example is attached to simulate the variation in the dynamic response of a plane frame structure based on FEM and TWM.

In the fifth chapter, an energy-based approach, Energy Flux, for the dynamic analysis of structures is introduced. The reflection and transmission coefficients at various types of structural joints are derived based on elementary theories. The application of this method on plane frame structures is presented.

Chapter six gives a brief information about the Soil-Structure Interaction (SSI) analysis and discusses some examples of existing FIFs. The integration of SSI in SEM and TWM methods is presented.

2. FORMULATION OF GOVERNING DIFFERENTIAL EQUATIONS OF MOTION

The mathematical expressions that relate the dynamic displacements to the applied dynamic forces are called as Governing Differential Equations of Motion (GDEM). Since the equilibrium and compatibility concepts of mechanics of the structures involve forces and displacements, respectively, they must be satisfied by the GDEM. The most important and the most challenging part of the dynamic analysis of structures is the formulation of GDEM [5]. The most common approaches to derive GDEM are direct equilibration using d'Alembert's principle, principle of virtual displacements, variational approach (Hamilton's principle) and Lagrange's equations of motion.

The equilibrium condition states that the sum of the internal and external forces, or moments, are equal to zero at each joint and each node of the structure. The compatibility condition indicates that the displacements of two nodes are equal if they are connected at the same joint.

In direct equilibrium approach, the equation of motion represents the Newton's second law and the inertial forces represent the d'Alembert's principle. Newton's second law states that, the force is equal to the product of the mass and acceleration. According to the d'Alembert's principle, developed internal force is proportional to the mass and its acceleration. For simple systems, direct equilibrium approach is the most convenient method to express the GDEM. However, as the degrees of freedoms (DOFs) and the number of masses connected to each other increase, this method becomes cumbersome. In such cases, equation of motion may be obtained more conveniently using principle of virtual displacements. In accordance with this method, the work done by the virtual displacements are equal to zero if a system is in equilibrium. Hamilton's principle and Lagrange's equations of motion are classified as energy-based approaches since both uses kinetic and potential energy terms to evaluate the GDEM.

2.1. Rod Theories

A rod is a structural element, which can only resist loads in its axial direction. Since stresses are developed in the axial direction of the member, deformations are formed along the same direction.

Figure 2.1 shows the material and geometric properties of a rod and the forces acting on an infinitesimally small rod segment. E is the Young's modulus of the material, A is the area of the section, ρ is the mass density per unit volume, ν is the Poisson's ratio, L is the length of the member, $q(x, t)$ is the externally applied body force per unit volume, F is the resultant in the longitudinal direction and $u(x, t)$ is the displacement in the longitudinal direction.

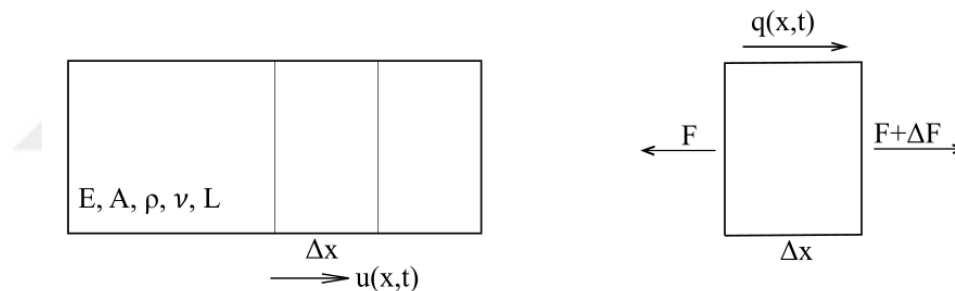


Figure 2.1. Properties of a rod element and forces acting on a segment of a rod.

Four main theories with different complexities exist in the literature for the longitudinal vibration of rod elements. The simplest one is the *Elementary Rod Theory*, which can be found in the book by Doyle [6]. *Love Rod Theory* is the modified version of elementary rod theory, developed by Love [7]. *Mindlin-Herrmann Rod Theory* can be considered as the improved version of the Love rod theory, which is proposed by Mindlin and Herrmann [8]. The most complex one is the *Three-Mode Rod Theory*, which was developed by Viktorow [9]. Generally Elementary or Love rod theories are utilized in structural analysis, since Mindlin-Herrmann and Three-mode theories introduce additional DOFs. According to Krawczuk, Grabowska and Palacz [10], Love theory will be sufficient to obtain accurate dynamic response up to the frequencies that represent the very high modes.

2.1.1. Elementary Rod Theory

Elementary rod theory assumes that only axial force $F(x, t)$ is acting through each section, and considers only the axial deformations and longitudinal wave motions. According to this theory, stresses and deflections developed in the section are in axial direction and uniformly distributed along the neutral axis. The contribution of the transverse motion to the stresses due to Poisson's effect is neglected. The axial strain in an infinitesimally small segment with length Δx is calculated as:

$$\varepsilon_{xx} = \frac{\partial u}{\partial x} \quad (2.1)$$

The internal forces developed under the effect of the applied external load is:

$$F + \Delta F - F + q\Delta x = \rho A \Delta x \ddot{u} \quad (2.2)$$

Since the material is assumed to be linear, Hooke's law gives the stress as,

$$\sigma_{xx} = E\varepsilon_{xx} = E \frac{\partial u}{\partial x} \quad (2.3)$$

The resultant axial force is calculated as,

$$F = \int \sigma_{xx} dA = EA \frac{\partial u}{\partial x} \quad (2.4)$$

By means of compatibility, equilibrium and constitutive behavior, the differential equation of the motion for a rod element based on Elementary rod theory is calculated as:

$$EA \frac{\partial^2 u}{\partial x^2} = \rho A \frac{\partial^2 u}{\partial t^2} - q \quad (2.5)$$

2.1.2. Love Rod Theory

Love rod theory assumes that, a rod element deforms along its axial direction and also contracts due to the Poisson's effect. As a consequence of the contraction, each point along the element has a transverse component of velocity. Thus, the kinetic energy of the element is affected by an additional term related to the particle velocity in transverse direction. The strain energy of the element is the same as for the elementary rod theory. The transverse strain and the particle velocity in transverse direction is derived as,

$$\varepsilon_T = -\nu \frac{\partial u}{\partial x} \quad (2.6)$$

$$\dot{u}_T = -\nu r \frac{\partial \dot{u}}{\partial x} \quad (2.7)$$

where, ε_T is the transverse strain, \dot{u}_T is the transverse velocity, ν is the Poisson's ratio and r is the distance from the centroid of the cross section. The expressions given in Equations 2.8 and 2.9 below represent the derivation of the potential and kinetic energies. In these equations, U stands for the potential energy, T is for kinetic energy and J is the polar moment of area.

$$U = \frac{1}{2} \int_0^L EA \left(\frac{\partial u}{\partial x} \right)^2 dx \quad (2.8)$$

$$T = \frac{1}{2} \int_0^L \rho \left[A\dot{u}^2 + \nu^2 J \left(\frac{\partial \dot{u}}{\partial x} \right)^2 \right] dx \quad (2.9)$$

The governing differential equation of the motion based on the Love rod theory is derived by means of Hamilton's principle as follows,

$$EA \frac{\partial^2 u}{\partial x^2} + \nu^2 \rho J \frac{\partial^2 \ddot{u}}{\partial x^2} = \rho A \frac{\partial^2 u}{\partial t^2} - q \quad (2.10)$$

2.1.3. Mindlin-Herrmann Rod Theory

Mindlin-Herrmann rod theory is an improved version of the Love rod theory, in which, in addition to the axial and transverse strains, the shear deformations due to the transverse displacements are considered. Unlike the Love rod theory, an extra DOF related to the lateral contraction is introduced. The shear deformation is independent from the axial deformations and non-uniform distribution of the longitudinal displacement is ignored. Thus, the deformation field can be expressed as,

$$\bar{u}(x, y) \approx u(x) \quad (2.11)$$

$$\bar{v}(x, y) \approx \psi(x)y \quad (2.12)$$

In Eq. 2.12, $\psi(x)$ stands for the vertical contraction. The following expression stands for the 2D stresses assuming the state of plane stress,

$$\sigma_{xx} = (2\mu + \lambda) \left(\frac{\partial \bar{u}}{\partial x} + \nu \frac{\partial \bar{v}}{\partial y} \right) \quad (2.13)$$

$$\sigma_{yy} = (2\mu + \lambda) \left(\frac{\partial \bar{v}}{\partial y} + \nu \frac{\partial \bar{u}}{\partial x} \right) \quad (2.14)$$

$$\tau_{xy} = \mu \left(\frac{\partial \bar{u}}{\partial y} + \frac{\partial \bar{v}}{\partial x} \right) \quad (2.15)$$

In equations 2.13 to 2.15, λ and μ are the Lamé constants, which are defined as,

$$\lambda = \frac{\nu E}{(1 + \nu)(1 - 2\nu)} \quad (2.16)$$

$$\mu = \frac{E}{2(1 + \nu)} \quad (2.17)$$

Potential and kinetic energies of the section is derived as follows,

$$U = \frac{1}{2} \int_0^L \left\{ (2\mu + \lambda) A \left[\left(\frac{\partial u}{\partial x} \right)^2 + \psi^2 \right] + 2\lambda A \frac{\partial u}{\partial x} \psi + \mu I \left(\frac{\partial \psi}{\partial x} \right)^2 \right\} dx \quad (2.18)$$

$$T = \frac{1}{2} \int_0^L \left(\rho A \dot{u}^2 + \rho I \dot{\psi}^2 \right) dx \quad (2.19)$$

The GDEM based on Mindlin-Herrmann rod theory is derived using the equations 2.18 and 2.19 for potential and kinetic energies, respectively and utilizing the Hamilton's principle as,

$$\frac{\partial}{\partial x} \left[(2\mu + \lambda)A \frac{\partial u}{\partial x} \right] + \lambda A \frac{\partial \psi}{\partial x} = \rho A \frac{\partial^2 v}{\partial t^2} - q \quad (2.20)$$

$$\frac{\partial}{\partial x} \left[\mu I K_1 \frac{\partial \psi}{\partial x} \right] - (2\mu + \lambda) A \psi - \lambda A \frac{\partial u}{\partial x} = \rho I K_2 \frac{\partial^2 \psi}{\partial t^2} \quad (2.21)$$

In Eq. 2.21, I is the second moment of inertia, K_1 and K_2 are the adjustable parameters that are chosen to give the best correspondence between the waveguide theory and the 2-D theory [11]. These parameters can be calculated using the equations 2.22 and 2.23 which are given below [12],

$$K_1 = \frac{12}{\pi^2} \quad (2.22)$$

$$K_2 = K_1 \left(\frac{1 + \nu}{0.87 + 1.12\nu} \right)^2 \quad (2.23)$$

The rod theories mentioned earlier can be recovered by setting the parameters appropriately. For instance, elementary rod theory is recovered by setting the term $\mu I K_1 = 0$ and $\rho I K_2 = 0$ and replacing ψ in terms of u .

2.1.4. Three-Mode Rod Theory

Three-mode rod theory is the most complex rod theory when compared to the theories presented earlier. The theory considers the longitudinal displacement, Poisson's ratio effect and the parabolic distribution of the longitudinal displacement along the cross section. In addition to Mindlin-Herrmann rod theory, a new DOF related to the parabolic distribution of the axial displacement is introduced. As a result, three degrees of freedom, one longitudinal and two rotational, exist at each node of the rod

element. The deformation field is expressed as:

$$\bar{u}(x, y) \approx u(x) + \phi(x)h \left(1 - 12\frac{y^2}{h^2}\right) \quad (2.24)$$

$$\bar{v}(x, y) \approx \psi(x)y \quad (2.25)$$

In Eq. 2.24, $\phi(x)$ stands for the parabolic distribution of the axial displacement, h is for the height of the rod element. The corresponding strains and stresses to these deformations are expressed in the equations from 2.26 to 2.28 and from 2.29 to 2.31, respectively.

$$\varepsilon_{xx} = \frac{\partial u}{\partial x} + \frac{\partial \phi}{\partial x} h \left(1 - 12\frac{y^2}{h^2}\right) \quad (2.26)$$

$$\varepsilon_{yy} = \psi \quad (2.27)$$

$$\gamma_{xy} = \left(-24\frac{\phi y}{h} + \frac{\partial \psi}{\partial x}\right) y \quad (2.28)$$

$$\sigma_{xx} = (2\mu + \lambda) \left[\frac{\partial u}{\partial x} + \frac{\partial \phi}{\partial x} h \left(1 - 12\frac{y^2}{h^2}\right) \right] + \lambda \psi \quad (2.29)$$

$$\sigma_{yy} = (2\mu + \lambda) \psi + \lambda \left[\frac{\partial u}{\partial x} + \frac{\partial \phi}{\partial x} h \left(1 - 12\frac{y^2}{h^2}\right) \right] \quad (2.30)$$

$$\tau_{xy} = \mu y \left(-24\frac{\phi y}{h} + \frac{\partial \psi}{\partial x}\right) \quad (2.31)$$

Potential and kinetic energies are calculated as follows,

$$U = \frac{1}{2} \int_0^L \left\{ (2\mu + \lambda) A \left[\left(\frac{\partial u}{\partial x}\right)^2 + \frac{4}{5} h^2 \left(\frac{\partial \phi}{\partial x}\right)^2 + \psi^2 \right] + 2\lambda A \frac{\partial u}{\partial x} \psi + \mu I \left(\frac{\partial \psi}{\partial x} - 24\frac{\phi}{h}\right)^2 \right\} dx \quad (2.32)$$

$$T = \frac{1}{2} \int_0^L \left(\rho A \dot{u}^2 + \rho A \frac{4}{5} h^2 \dot{\phi}^2 + \rho I \dot{\psi}^2 \right) dx \quad (2.33)$$

The governing differential equation of motion for the Three-Mode rod theory is derived using the definitions given in equations 2.32 and 2.33 for potential and kinetic

energies, respectively, and utilizing the Hamilton's principle as:

$$\frac{\partial}{\partial x} \left[(2\mu + \lambda) A \frac{\partial u}{\partial x} \right] + \lambda A \frac{\partial \psi}{\partial x} = \rho A \frac{\partial^2 u}{\partial t^2} - q \quad (2.34)$$

$$\frac{\partial}{\partial x} \left(\mu I \frac{\partial \psi}{\partial x} \right) - (2\mu + \lambda) A \psi - \lambda A \frac{\partial u}{\partial x} - 2\mu A h \frac{\partial \phi}{\partial x} = \rho I \frac{\partial^2 \psi}{\partial t^2} \quad (2.35)$$

$$\frac{\partial}{\partial x} \left[(2\mu + \lambda) I \frac{\partial \phi}{\partial x} \right] - 5\mu A \phi + \frac{10}{48} \mu A h \frac{\partial \psi}{\partial x} = \rho I \frac{\partial^2 \phi}{\partial t^2} \quad (2.36)$$

2.2. Beam Theories

A beam is a structural element that supports bending moments and shear forces developed due to the applied transverse loads. Figure 2.2 shows the material and geometric properties of a beam and the forces acting on an infinitesimally small beam segment. E is the Young's modulus of the material, I is the second moment of the area, ρ is the mass density per unit volume, A is the area of the section, ν is the Poisson's ratio, L is the length of the member, $q(x, t)$ is the externally applied body force per unit volume and $v(x, t)$ is the deflection of the centerline. The resultant forces and moments are represented by V and M , respectively.

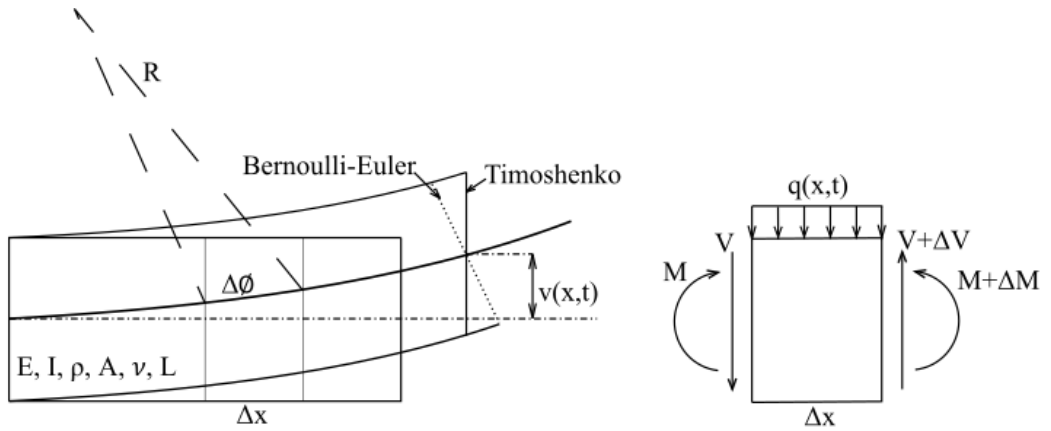


Figure 2.2. Properties of a beam element and forces acting on a segment of a beam.

Flexural response of a beam is commonly defined based on the Bernoulli-Euler and Timoshenko beam theories. The evolution of the Bernoulli-Euler beam theory dates to 18th century. Rayleigh beam theory is an improved version of the Bernoulli-Euler beam

theory, which accounts for the effects of the rotational inertia. The Timoshenko beam theory [13] considers the effects of both shear deformations and rotational inertia.

2.2.1. Bernoulli-Euler Beam Theory

Bernoulli-Euler beam theory, which is also referred as the engineer's beam theory or classical beam theory, assumes that only bending moment $M(x, t)$ and shear forces $V(x, t)$ are acting through each section. The theory accounts only for flexural deformations and flexural wave motions. Although transverse shear forces are considered, any shear deformations due to it is neglected. Since shear deformation through the thickness is neglected, vertical displacements, $v(x, t)$, can be assumed to be nearly constant and the stress state is uniaxial along the thickness. Thus, the assumption of “*plane sections remain plane*” is valid. The slope, $\phi(x, t)$, of the section can be obtained by differentiating the transverse displacement, $v(x, t)$, with respect to spatial coordinates. According to the small deflection theory, deformation field of the Bernoulli-Euler beam is expressed as follows,

$$\bar{u}(x, y) \approx -y\phi(x) \quad (2.37)$$

$$\bar{v}(x, y) \approx v(x) \quad (2.38)$$

The nonzero strains due to the deformations are calculated as,

$$\varepsilon_{xx} = -y \frac{\partial^2 v}{\partial x^2} \quad (2.39)$$

The stress, calculated according to the Hooke's law, is given in as

$$\sigma_{xx} = -Ey \frac{\partial^2 v}{\partial x^2} \quad (2.40)$$

The equilibrium conditions give that

$$\frac{\partial V}{\partial x} = \rho A \frac{\partial^2 v}{\partial t^2} - q_v \quad (2.41)$$

$$\frac{\partial M}{\partial x} + V = -q_\phi \quad (2.42)$$

The resultant moment is calculated as

$$M = \int -\sigma_{xx} y dA = EI \frac{\partial^2 v}{\partial x^2} \quad (2.43)$$

The equation of the motion is obtained by substituting Eq. 2.43 into the equilibrium conditions for shear force and moment, which are given by the equations 2.41 and 2.42 as follows

$$EI \frac{\partial^4 v}{\partial x^4} + \rho A \frac{\partial^2 v}{\partial t^2} = q \quad (2.44)$$

2.2.2. Timoshenko Beam Theory

Timoshenko beam theory accounts for the effects of shear deformation and rotational inertia. The assumptions made in the Bernoulli-Euler beam theory are valid, except the one that assumes plane sections remain plane after deformation. Since the shear deformation is introduced, plane sections do not remain plane after deformation. The displacement field is expressed as the displacement field related to Bernoulli-Euler beam theory. The strains and the stresses are expressed as follows,

$$\varepsilon_{xx} = -y \frac{\partial^2 v}{\partial x^2} \quad (2.45)$$

$$\varepsilon_{yy} = 0 \quad (2.46)$$

$$\gamma_{xy} = -\phi + \frac{\partial v}{\partial x} \quad (2.47)$$

$$\sigma_{xx} = -Ey \frac{\partial \phi}{\partial x} \quad (2.48)$$

$$\tau_{xy} = G \left(-\phi + \frac{\partial v}{\partial x} \right) \quad (2.49)$$

Total strain energy and kinetic energy can be calculated using following equations,

$$U = \frac{1}{2} \int_0^L \left[EI \left(\frac{\partial \phi}{\partial x} \right)^2 + GA \left(\phi - \frac{\partial v}{\partial x} \right)^2 \right] dx \quad (2.50)$$

$$T = \frac{1}{2} \int_0^L \rho \left(I \dot{\phi}^2 + A \dot{v}^2 \right) dx \quad (2.51)$$

The equations of the motion, obtained by using the Hamilton's principle, is given as

$$GAK_1 \left[\frac{\partial^2 v}{\partial x^2} - \frac{\partial \phi}{\partial x} \right] = \rho A \frac{\partial^2 v}{\partial t^2} - q \quad (2.52)$$

$$EI \left(\frac{\partial^2 \phi}{\partial x^2} \right) + GAK_1 \left(\frac{\partial v}{\partial x} - \phi \right) = \rho IK_2 \frac{\partial^2 \phi}{\partial t^2} \quad (2.53)$$

In equations 2.52 and 2.53 GAK_1 is the shear stiffness of the section and K_1 and K_2 are adjustable parameters for shear and rotational inertia. In case of Bernoulli Euler beam, $GAK_1 = \infty$ and $\rho IK_2 = 0$, which ensures the assumptions for the shear deformations and rotational inertia. Besides the Bernoulli-Euler beam theory, Rayleigh beam theory can also be obtained by setting $GAK_1 = \infty$. It is recommended to select values of $K_1 = \pi^2/12$ and $K_2 = 1$ for a rectangular cross-section [12].

3. SPECTRAL ELEMENT METHOD

Dynamic analysis of structures is generally carried out using Finite Element Method (FEM). In medium to high frequency range, FEM cannot capture the dynamic response accurately. FEM is formulated based on the frequency independent shape functions, which are obtained from the weak form of the governing differential equations and the inertial loads are concentrated at member ends. In order to improve the accuracy of the response in FEM, the mesh size used in modeling must be smaller than the shortest wavelength. In other words, the response at frequencies with wavelengths that are smaller than the mesh size (i.e., high frequencies) cannot be calculated accurately. Therefore, to account for such high frequency responses, the number of elements and the number of the degrees of freedoms (DOFs) in the FEM model should be increased substantially.

Spectral Element Method (SEM) is a robust and alternative method to FEM for calculating the dynamic response and identifying the dynamic characteristics of engineering structures. SEM is formulated based on the frequency dependent shape functions, which are determined from the exact solution of the differential equation of an element. In literature, it is referred as the exact method, as it uses the exact solutions to the wave equations and considers inertial forces directly [1]. Since each component of the structure is seen as a waveguide and can be assembled using a matrix analogy to FEM, complex structures can be handled. Unlike the conventional FEM, high-frequency wave modes, which are the modes more sensitive to small changes in the dynamic characteristics of the structure, can be captured without dividing elements into small sized segments. Thus, the number of elements and the number of DOFs are decreased substantially [2].

In his pioneering study, Doyle applied SEM to wave propagation in structures [14]. He derived spectral element matrices for rod, beam, plate elements and for bounded and unbounded media. Gopalakrishnan [15], expanded the field of use of this method by producing spectral element matrices related to higher order element theories and

tapered elements. Moreover, he also introduced the super spectral element, which combines the SEM and FEM. Gopalakrishnan, Martin and Doyle [2], presented a matrix methodology to handle frame structures. Krawczuk, Grabowska and Palacz [10] applied SEM to four different rod theories and compared them. Rizzi and Doyle [16,17] applied this method to bounded and unbounded media.

In SEM, the time domain governing differential equation of motion (GDEM), which is given by Eq. 3.1, is converted into frequency domain via Discrete Fourier Transformation (DFT).

$$\mathcal{L}(u) + \mathcal{M}(\ddot{u}) = q \quad (3.1)$$

In Eq. 3.1, \mathcal{L} is the differential operator, \mathcal{M} is the inertial operator, double dot is the second derivative with respect to time and q is the externally applied body force. The solution to the Eq. 3.1 is represented as,

$$u(x, t) = \sum_n \hat{u}_n(x, \omega_n) e^{i\omega_n t} \quad (3.2)$$

In Eq. 3.2, \hat{u}_n is the spatially dependent Fourier coefficient and ω_n is the circular frequency. Then, the GDEM in the frequency domain is obtained as,

$$\mathcal{L}\hat{u}_n(x) - \omega_n^2 \mathcal{M}\hat{u}_n(x) = \hat{q} \quad (3.3)$$

The homogenous solution to the wave equation is given in Eq. 3.4. For brevity, the subscripts n will be omitted.

$$\hat{u}(x) = \sum_{i=1}^p e^{(-ik_i(\omega)x)} C_i \quad (3.4)$$

$k_i(\omega)$ is the wavenumber of the i^{th} mode, which is one of the distinct roots of the characteristic equation of the wave equation. C_i is the constant related to the i^{th} mode. The general solution must satisfy both the geometric and natural boundary

conditions at both ends of a member, which corresponds to $x = 0$ and $x = L$ for an element with length L .

The frequency dependent shape functions are obtained from the Eq. 3.4 using the geometric and natural boundary conditions related to the both end nodes of the element. By virtue of these dynamic shape functions, the dynamic stiffness matrices are constructed. Since the dynamic stiffness matrices are frequency dependent, they must be evaluated at each frequency within the interested frequency interval. Basic steps of the general procedure for SEM is illustrated in Figure 3.1.

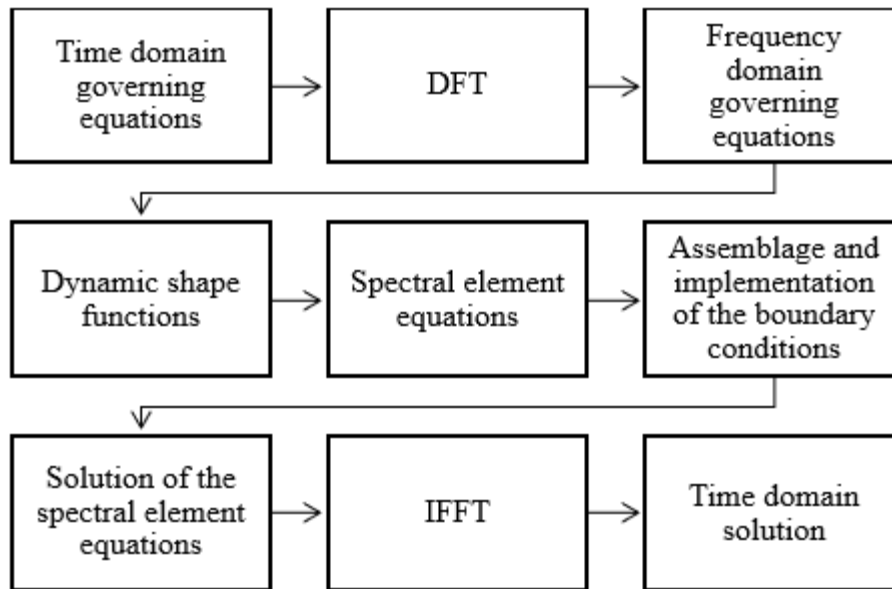


Figure 3.1. General procedure for SEM.

Additional information about the construction of the dynamic stiffness matrices can be found in the following sections.

3.1. Spectral Element for Rod Elements

Spectral element matrices for rod elements are obtained based on the elementary, Love, Mindlin-Herrmann and Three-Mode rod theories. The time domain GDEMs related to these theories are defined in Section 2.1 Rod Theories.

The need for higher order rod theories results from the inadequacy of elementary rod theory to capture an accurate dynamic response, if the element is deep and/or the frequency of interest is large. Doyle [12], derived the exact displacements and tractions under the effect of 20 kHz narrowband pulse, which is presented in Figure 3.2. In this figure, each line corresponds to a different time. The longitudinal displacements follow a parabolic path in contrast to the assumption made in the Elementary rod theory. The transverse displacements are almost linear. As a result, the higher order rod theories yield more accurate results since the stresses and strains are computed based on more realistic assumptions.

Even though, exact displacements and tractions prove that the higher order rod theories are necessary in the dynamic analysis of deep elements at higher frequencies, higher order rod theories have their drawbacks due to the generated additional modes, which are not considered in the standard analysis of structures. As stated by the Krawczuk, Grabowska and Palacz [10], Love rod theory seems to be the most practical theory, which can be used in the dynamic analysis up to the highest vibration frequencies, because it does not introduce additional vibration modes and compatible with the first mode of the both Mindlin-Herrmann and Three- Mode theories.

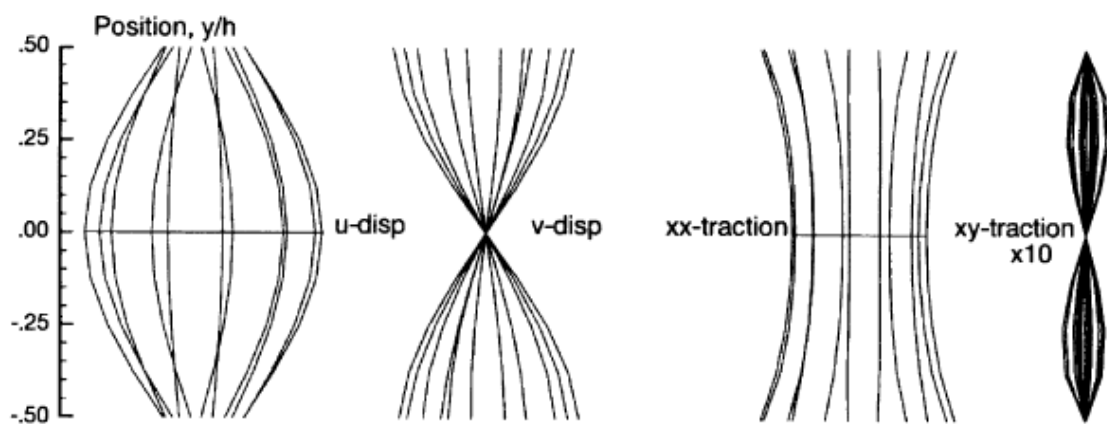


Figure 3.2. Exact displacements and traction distributions on a cross section [12].

3.1.1. Elementary Rod Theory

Time domain GDEM is given by Eq. 2.5. The spectral representation of this equation is:

$$EA \frac{d^2 \hat{u}}{dx^2} + \rho A \omega^2 \hat{u} = -\hat{q} \quad (3.5)$$

The longitudinal displacement at any arbitrary point of the element using the wave solution is derived as,

$$\hat{u}(x) = A e^{-ik_R x} + B e^{-ik_R(L-x)} \quad (3.6)$$

The first term in Eq. 3.6 stands for the forward-moving wave and the second term for the backward-moving wave, x represents the location of the arbitrary point, L is the element length and k_R is the wavenumber. The wavenumber is calculated as:

$$k_R = \sqrt{(\omega^2 \rho A) / (EA)} \quad (3.7)$$

The nodal displacements at i^{th} and j^{th} end of the structure referred as \hat{u}_1 and \hat{u}_2 , and are derived by substituting the related x values into Eq. 3.6. Thus, frequency dependent shape functions, which are represented by $\hat{g}_{R1}(x)$ and $\hat{g}_{R2}(x)$ are computed as

$$\begin{aligned} \hat{u}(x) &= \begin{bmatrix} \hat{g}_{R1}(x) & \hat{g}_{R2}(x) \end{bmatrix} \begin{Bmatrix} \hat{u}_1 \\ \hat{u}_2 \end{Bmatrix} \\ &= \begin{bmatrix} e^{-ik_R x} & e^{-ik_R(L-x)} \end{bmatrix} \begin{bmatrix} 1 & e^{-ik_R L} \\ e^{-ik_R L} & 1 \end{bmatrix}^{-1} \begin{Bmatrix} \hat{u}_1 \\ \hat{u}_2 \end{Bmatrix} \end{aligned} \quad (3.8)$$

The spectral element matrix is obtained by using the relation between the axial

force and the axial displacement as

$$\begin{Bmatrix} \hat{F}_1 \\ \hat{F}_2 \end{Bmatrix} = \begin{Bmatrix} -\hat{F}(0) \\ \hat{F}(L) \end{Bmatrix} = EA \begin{bmatrix} -\hat{g}'_{R1}(0) & -\hat{g}'_{R2}(0) \\ \hat{g}'_{R1}(L) & \hat{g}'_{R2}(L) \end{bmatrix} \begin{Bmatrix} \hat{u}_1 \\ \hat{u}_2 \end{Bmatrix} \quad (3.9)$$

In Eq. 3.9, the prime stands for the first derivative of the shape functions with respect to the spatial coordinate. The dynamic stiffness matrix is a square and symmetric matrix. In case of undamped structures, it is real valued. For damped structures, the elements of the matrix are complex valued.

3.1.2. Love Rod Theory

Time domain GDEM is given by Eq. 2.10. The spectral representation of this equation is:

$$EA \frac{d^2 \hat{u}}{dx^2} - \omega^2 \nu^2 \rho J \frac{d^2 \hat{u}}{dx^2} + \omega^2 \rho A \hat{u} = -\hat{q} \quad (3.10)$$

The longitudinal displacement at any arbitrary point of a rod element is derived as,

$$\hat{u}(x) = Ae^{-ik_R x} + Be^{-ik_R(L-x)} \quad (3.11)$$

The first term in Eq. 3.11 stands for the incident wave and the second term for the reflected wave. k_R is the wavenumber, which is obtained from the characteristic equation as

$$k_R = \sqrt{\frac{\omega^2 \rho A}{EA - \omega^2 \nu^2 \rho J}} \quad (3.12)$$

The dynamic stiffness matrix for a rod element based on the Love rod theory is

obtained using a procedure analogous to the elementary rod theory and is found as

$$\begin{Bmatrix} \hat{F}_1 \\ \hat{F}_2 \end{Bmatrix} = \begin{Bmatrix} -\hat{F}(0) \\ \hat{F}(L) \end{Bmatrix} = \begin{bmatrix} EA \begin{bmatrix} -\hat{g}'_{R1}(0) & -\hat{g}'_{R2}(0) \\ \hat{g}'_{R1}(L) & \hat{g}'_{R2}(L) \end{bmatrix} \\ +\nu^2 \rho \omega^2 J \begin{bmatrix} \hat{g}_{R1}(0) & \hat{g}_{R2}(0) \\ -\hat{g}_{R1}(L) & -\hat{g}_{R2}(L) \end{bmatrix} \end{bmatrix} \begin{Bmatrix} \hat{u}_1 \\ \hat{u}_2 \end{Bmatrix} \quad (3.13)$$

The stiffness matrix is complex, square and symmetric.

3.1.3. Mindlin-Herrmann Rod Theory

Time domain GDEM for Mindlin-Herrmann rod theory is given by the equations Eq. 2.20 and 2.21. The matrix form of the spectral representation is:

$$\begin{bmatrix} -T_1 k_R^2 + \rho A \omega^2 & -i k_R T_2 \\ i k_R T_2 & -T_3 k_R^2 - T_1 + \rho I K_2 \omega^2 \end{bmatrix} \begin{Bmatrix} \hat{u} \\ \hat{\psi} \end{Bmatrix} = \begin{Bmatrix} 0 \\ 0 \end{Bmatrix} \quad (3.14)$$

where, T_1 , T_2 and T_3 are calculated as:

$$T_1 = (2\mu + \lambda) A; \quad T_2 = \lambda A; \quad T_3 = \mu I K_1 \quad (3.15)$$

Setting determinant equal to zero gives the characteristic equation, which will be used to obtain wavenumbers. Equation 3.14 given above yields to two-mode pairs. Wavenumbers k_{R1} and k_{R2} in equations Eq. 3.16 and 3.17 stand for the first and second mode pairs, respectively. An additional term is introduced in the wave solution of the Mindlin-Herrmann rod theory due to the second propagating mode, which arises due to the Poisson's effect. Thus, the displacements are derived as:

$$\hat{u}(x) = AR_1 e^{-ik_{R1}x} + BR_2 e^{-ik_{R2}x} - CR_1 e^{-ik_{R1}(L-x)} - DR_2 e^{-ik_{R2}(L-x)} \quad (3.16)$$

$$\hat{\psi}(x) = Ae^{-ik_{R1}x} + Be^{-ik_{R2}x} + Ce^{-ik_{R1}(L-x)} + De^{-ik_{R2}(L-x)} \quad (3.17)$$

The first two terms of the equations 3.16 and 3.17 stand for the incident waves and the last two terms for the reflected waves. R_1 and R_2 represent the amplitude ratios and calculated as follows,

$$R_i = \frac{ik_{Ri}\lambda A}{-(2\mu + \lambda) Ak_{Ri}^2 + \rho A\omega^2} \quad (3.18)$$

The shape functions for the longitudinal displacement and the displacement related to Poisson's ratio effect are derived by substituting boundary conditions into Eqs. 3.16 and 3.17. The stiffness matrix is constructed as it is done for the previous rod theories using the relation between force and displacement, which is given as:

$$\hat{F} = (2\mu + \lambda) A \frac{\partial \hat{u}}{\partial x} + \lambda A \hat{\psi} \quad (3.19)$$

$$\hat{Q} = \mu I K_1 \frac{\partial \hat{\psi}}{\partial x} \quad (3.20)$$

The explicit form of the stiffness matrix of Mindlin-Herrmann rod can be found in the paper by Krawczuk et al. [10].

3.1.4. Three-Mode Rod Theory

The time-domain GDEM for the Three-Mode rod theory is given by the equations 2.34 to 2.36. The matrix form of the spectral representation is given as

$$\begin{bmatrix} T_4 & -ik_R\lambda A & 0 \\ ik_R\lambda A & T_5 & 2ik_R\mu Ah \\ 0 & -\frac{10}{48}i\mu Ah & T_6 \end{bmatrix} \begin{Bmatrix} \hat{u} \\ \hat{\psi} \\ \hat{\phi} \end{Bmatrix} = \begin{Bmatrix} 0 \\ 0 \\ 0 \end{Bmatrix} \quad (3.21)$$

where,

$$\begin{aligned} T_4 &= -(2\mu + \lambda) Ak_R^2 + \rho A\omega^2 \\ T_5 &= -\mu I k_R^2 - (2\mu + \lambda) A + \rho I \omega^2 \\ T_6 &= -(2\mu + \lambda) I k_R^2 - 5\mu A + \rho I \omega^2 \end{aligned}$$

Wavenumbers k_{R1} , k_{R2} and k_{R3} representing the generated three-modes can be found by solving the characteristic equation. The displacements are derived using the formulations given below,

$$\begin{aligned} \hat{u}(x) = & AR_4e^{-ik_{R1}x} + BR_5e^{-ik_{R2}x} + CR_6e^{-ik_{R3}x} \dots \\ & +DR_4e^{-ik_{R1}(L-x)} + ER_5e^{-ik_{R2}(L-x)} + FR_6e^{-ik_{R3}(L-x)} \end{aligned} \quad (3.22)$$

$$\begin{aligned} \hat{\psi}(x) = & AR_1e^{-ik_{R1}x} + BR_2e^{-ik_{R2}x} + CR_3e^{-ik_{R3}x} \dots \\ & -DR_1e^{-ik_{R1}(L-x)} - ER_2e^{-ik_{R2}(L-x)} - FR_3e^{-ik_{R3}(L-x)} \end{aligned} \quad (3.23)$$

$$\begin{aligned} \hat{\phi}(x) = & Ae^{-ik_{R1}x} + Be^{-ik_{R2}x} + Ce^{-ik_{R3}x} \dots \\ & +De^{-ik_{R1}(L-x)} + Ee^{-ik_{R2}(L-x)} + Fe^{-ik_{R3}(L-x)} \end{aligned} \quad (3.24)$$

The first three terms of the equations 3.22, 3.23 and 3.24 stand for the incident waves and the last three terms for the reflected waves. $R_1 \dots R_6$ represent the amplitude ratios and calculated as follows,

$$R_i = \frac{(2\mu + \lambda)Ik_{Ri}^2 + 5\mu A - \rho I\omega^2}{-\frac{10}{48}i\mu Ah} \quad (3.25)$$

where, $i = 1, 2, 3$

$$R_i = \frac{ik_{Rj}\lambda A}{-(2\mu + \lambda)Ak_{Rj}^2 + \rho A\omega^2} R_j \quad (3.26)$$

where, $i = 4, 5, 6$ and $i = 1, 2, 3$. Dynamic stiffness matrix of a rod element based on the Three-Mode theory is derived similar to the Mindlin-Herrmann rod theory, by using the force and displacement relations given by the following equations.

$$\hat{F} = (2\mu + \lambda) A \frac{\partial \hat{u}}{\partial x} + \lambda A \hat{\psi} \quad (3.27)$$

$$\hat{Q} = \mu I \left(\frac{\partial \hat{\psi}}{\partial x} - 24 \frac{\hat{\phi}}{h} \right) \quad (3.28)$$

$$\hat{S} = \frac{48}{5} (2\mu + \lambda) I \frac{\partial \hat{\phi}}{\partial x} \quad (3.29)$$

The explicit form of the stiffness matrix of Three-Mode rod can be found in the paper by Krawczuk et al. [10].

3.1.5. Comparison of the Rod Theories

In this section, elementary, Love, Mindlin-Herrmann and Three-Mode rod theories are compared to each other by means of the dispersion and spectrum relationships and the terms of the dynamic stiffness matrices. Dispersion represents the relation between the wave speed and the frequency. A wave is called as non-dispersive, if the speed of the wave is constant with respect to the frequency. Conversely, if the speed of the wave is changing as the frequency changes, the wave is called as dispersive wave. The wave speed is derived as:

$$c = \frac{\omega}{k}; c_g = \frac{d\omega}{dk} \quad (3.30)$$

Eq. 3.30 represents the derivation of the phase speed (c) and the group velocity (c_g). The dynamic analysis is based on superposition of harmonics at different frequencies, which travel at different phase speeds. Group velocity is the velocity of the superimposed wave groups.

In elementary rod theory, only one mode of vibration is generated. The wavenumber is purely real in undamped case and the wave is non-dispersive. The phase and group velocities are derived by the following equations:

$$c = \frac{\omega}{k_R} = \sqrt{\frac{EA}{\rho A}}; c_g = \frac{d\omega}{dk_R} = \sqrt{\frac{EA}{\rho A}} \quad (3.31)$$

Love rod theory considers the Poisson's ratio effect, but no additional mode of vibration is generated. The wavenumber can be purely imaginary after a certain frequency limit. Thus, transverse motion will absorb all of the input energy. Eq. 3.32

gives the phase velocity and the group velocity.

$$c = \frac{\omega}{k_R} = \sqrt{\frac{EA - \omega^2 v^2 \rho J}{\rho A}}; c_g = \frac{d\omega}{dk_R} = \sqrt{\frac{EA}{\rho A}} \left[1 - \frac{\omega^2 v^2 \rho J}{EA} \right]^{3/2} \quad (3.32)$$

Shear deformations due to motions in the transverse direction, and the Poisson's ratio effects are considered in the Mindlin-Herrmann rod theory. An additional mode with a cut-off frequency is generated. The cut-off frequency is obtained by setting the wavenumber in the characteristic equation equal to zero. The second mode does not propagate until the cut-off frequency, and starts to dominate the behavior beyond this limit. The cut-off frequency is calculated as

$$\omega_c = \sqrt{\frac{(2\mu + \lambda) A}{\rho I K_2}} \quad (3.33)$$

Group velocities for Mindlin-Herrmann rod is calculated by the formulae given below [18],

$$c_g = \frac{d\omega}{dk_R} = c^2 \left[c - \omega \frac{dc}{d\omega} \right]^{-1} \quad (3.34)$$

In Three-Mode theory two additional modes related to the Poisson's ratio effect and non-uniform distribution of the longitudinal displacements are generated. The cut-off frequencies related to these additional modes are given by Eq. 3.35 and the group velocity is calculated using Eq. 3.34.

$$\omega_{c1} = \sqrt{\frac{5\mu A}{\rho I}}; \omega_{c2} = \sqrt{\frac{(2\mu + \lambda) A}{\rho I}} \quad (3.35)$$

Figure 3.3 below shows the change in the absolute value of wavenumbers with frequency for the elementary, Love, Mindlin-Herrmann and Three-Mode rod theories.

In the low frequency range, the wavenumbers of elementary and Love rod theories are compatible. Additionally, the first mode of both Mindlin-Herrmann and Three-Mode rod theories behave in a similar manner. However, beyond an exact frequency range, behavior of the wavenumbers differentiate from each other. The second mode of the Mindlin-Herrmann rod theory is fully imaginary up to a certain limit of frequency, and beyond this limit it starts to propagate. Also, second and third modes of the Three-Mode theory have cut-off frequencies.

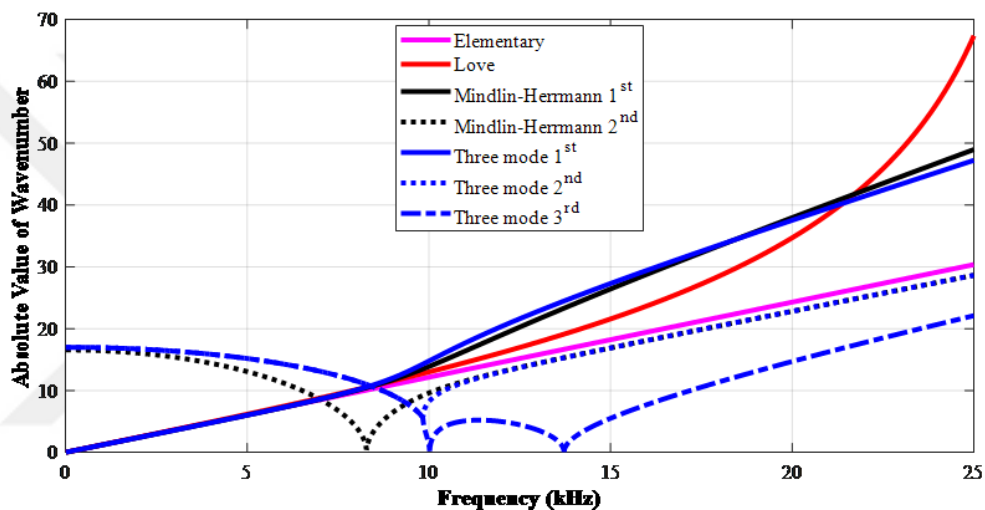


Figure 3.3. Spectrum relation for Elementary, Love, Mindlin-Herrmann and Three-mode rod theories.

The dispersion relationships for the four rod theories are presented in Figure 3.4. The vertical axis shows the absolute value of the ratio between group and phase velocities. When Elementary rod theory is considered, the wave propagates in a non-dispersive manner; the ratio is constant throughout the whole frequency range. Love rod theory shows that, as the frequency increases, group velocity becomes smaller than the phase velocity. Group velocities related to the first mode of the Mindlin-Herrmann and Three-Mode rod theories decrease until a certain frequency limit, then it increases to an asymptotical value. Additional modes generated by the both Mindlin Herrmann and Three-Mode rod theories propagate beyond the cut-off frequency. They increase up to an asymptotical value.

The terms of the stiffness matrices obtained based on the SEM, FEM and theo-

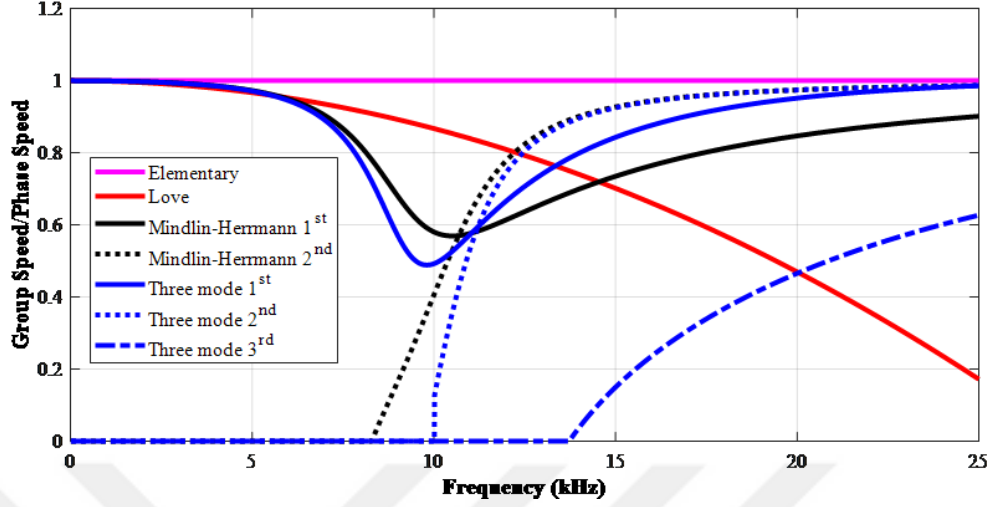


Figure 3.4. Dispersion relationship for elementary, Love, Mindlin-Herrmann and Three-mode rod theories.

retical solutions are compared to each other to investigate the difference in the stiffness terms. The stiffness matrices related to the conventional rod is constructed according to the formulation given below [6].

$$\mathbf{K} = \frac{EA}{L} \begin{bmatrix} 1 & -1 \\ -1 & 1 \end{bmatrix} - \frac{\rho AL\omega^2}{6} \begin{bmatrix} 2 & 1 \\ 1 & 2 \end{bmatrix} \quad (3.36)$$

The theoretical stiffness matrix is obtained using the general solution to ordinary differential equation and is given by Eq. 3.37 below:

$$\mathbf{K} = \frac{EA}{L} \frac{k_R}{\sin k_R L} \begin{bmatrix} \cos k_R L & -1 \\ -1 & \cos k_R L \end{bmatrix} \quad (3.37)$$

In Eq. 3.37, k_R represents the roots of the characteristic equation.

Figure 3.5, shows the absolute value of k_{11} term, which is the value at the first row and first column of the stiffness matrix, for the Elementary, Love and Mindlin-Herrmann rod theories, and the conventional and theoretical solutions.

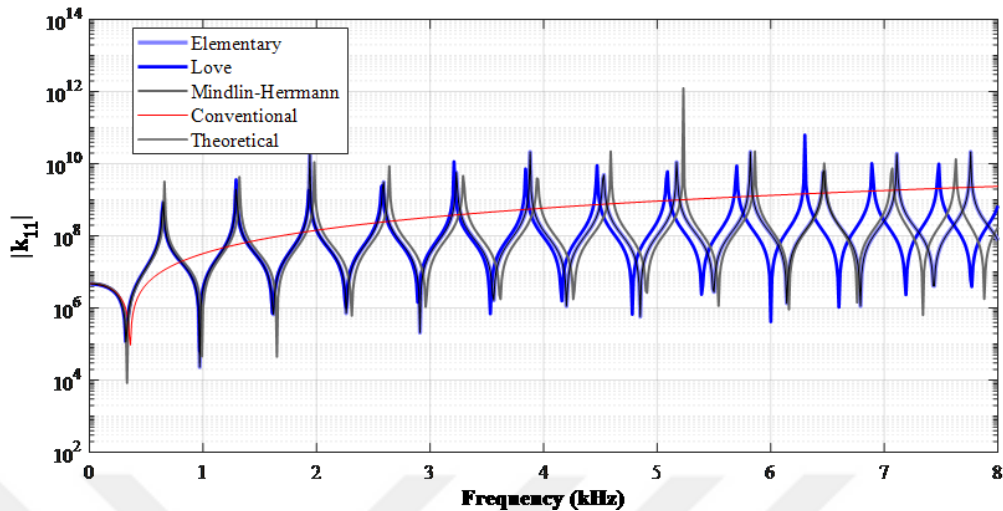


Figure 3.5. k_{11} values according to conventional, theoretical, Elementary, Love and Mindlin-Herrmann rod theories.

In the low frequency range, the stiffness terms, k_{11} , for all methods are identical. However, as the frequency increases, conventional rod differs from the others, while the other methods remain identical.

3.2. Spectral Element for Beam Elements

Spectral element matrices for beam elements based on the Bernoulli-Euler and Timoshenko beam theories are derived in this section. Related time domain GDEM can be found in Section 2.2 Beam Theories.

Bernoulli-Euler beam theory becomes erroneous at high frequencies, as it leads to unrealistic wave speeds. Moreover, if the element's depth is high, neglecting the effects of the rotational inertia and shearing deformations causes erroneous results. Thus, higher order beam theories should be adopted for such elements, and/or for high frequencies. Doyle [12] derived the exact displacements and tractions in a beam element with 100 mm high, subjected to 20 kHz narrowband pulse. The results are presented in Figure 3.6. In this figure, each line corresponds to a different time. The displacement in the longitudinal direction is compatible with the assumptions made in the Bernoulli-Euler beam theory. However, the distribution of the vertical displacements cannot be

captured based on this theory. As can be seen from the figure, parabolic distribution of the shear stress should be considered in the analysis.

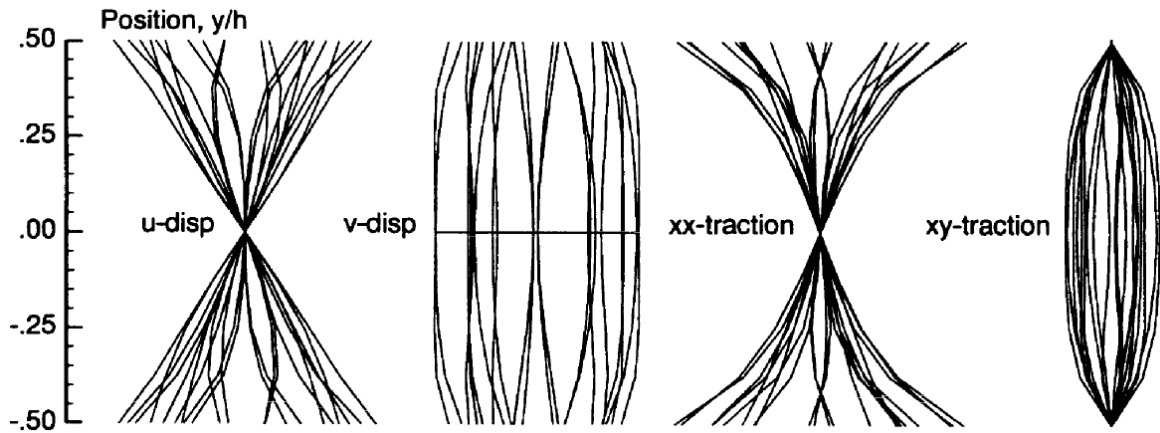


Figure 3.6. Exact displacements and traction distributions on a cross section [12].

Timoshenko beam theory does not produce additional degrees of freedoms, but considers deformations due to shear. As a result, the slope of the sections becomes an independent variable, and the wave mode related to that variable can be obtained. Consequently, the behavior of a beam element under an applied dynamic load can be obtained more precisely by using higher order beam theories.

3.2.1. Bernoulli-Euler Beam Theory

The time domain GDEM for the Bernoulli-Euler beam theory is given by Eq. 2.44. Frequency domain GDEM is obtained as

$$EI \frac{d^4 \hat{v}}{dx^4} - \omega^2 \rho A \hat{v} = \hat{q} \quad (3.38)$$

The displacement in the transverse direction at any arbitrary point is derived as given in equation 3.39 and the slope is derived simply by differentiating the vertical displacement with respect to spatial coordinate.

$$\hat{v}(x) = A e^{-ik_B x} + B e^{-k_B x} + C e^{-ik_B(L-x)} + D e^{-k_B(L-x)} \quad (3.39)$$

$$\hat{\phi}(x) = -ik_B A e^{-ik_B x} - k_B B e^{-k_B x} + ik_B C e^{-ik_B(L-x)} + k_B D e^{-k_B(L-x)} \quad (3.40)$$

The first two terms of the equations 3.39 and 3.40 are the incident waves, and the last two terms are the reflected waves. In addition, the first and the third terms are the wave propagation solution while the remaining terms are related to spatially damped vibrations [12]. k_B is the wavenumber and obtained as

$$k_B = \left(\frac{\omega^2 \rho A}{EI} \right)^{1/4} \quad (3.41)$$

The frequency dependent shape functions ($\hat{g}_{Bi}(x)$) are derived by substituting the boundary conditions to the equations 3.39, and 3.40, and are given by the following equation,

$$v(x) = \begin{Bmatrix} \hat{g}_{B1}(x) \\ \hat{g}_{B2}(x) \\ \hat{g}_{B3}(x) \\ \hat{g}_{B4}(x) \end{Bmatrix}^T \begin{Bmatrix} \hat{v}_1 \\ \hat{\phi}_1 \\ \hat{v}_2 \\ \hat{\phi}_2 \end{Bmatrix} \quad (3.42)$$

where,

$$\begin{Bmatrix} \hat{g}_{B1}(x) \\ \hat{g}_{B2}(x) \\ \hat{g}_{B3}(x) \\ \hat{g}_{B4}(x) \end{Bmatrix}^T = \begin{bmatrix} e^{-ik_B x} \\ e^{-k_B x} \\ e^{-ik_B(L-x)} \\ e^{-k_B(L-x)} \end{bmatrix}^T \begin{bmatrix} 1 & 1 & e^{-ik_B L} & e^{-k_B L} \\ -ik_B & -k_B & ik_B e^{-ik_B L} & k_B e^{-k_B L} \\ e^{-ik_B L} & e^{-k_B L} & 1 & 1 \\ -ik_B e^{-ik_B L} & -k_B e^{-k_B L} & ik_B & k_B \end{bmatrix}^{-1}$$

The dynamic shape functions are formed in pairs, and each component of the pairs are symmetric to each other. The spectral element matrix for a beam according to the Bernoulli-Euler beam theory can be constructed using the force-displacement relation-

ship as given in the following equation,

$$\begin{Bmatrix} \hat{V}_1 \\ \hat{M}_1 \\ \hat{V}_2 \\ \hat{M}_2 \end{Bmatrix} = EI \begin{bmatrix} \hat{g}_{B1}'''(0) & \hat{g}_{B2}'''(0) & \hat{g}_{B3}'''(0) & \hat{g}_{B4}'''(0) \\ -\hat{g}_{B1}''(0) & -\hat{g}_{B2}''(0) & -\hat{g}_{B3}''(0) & -\hat{g}_{B4}''(0) \\ -\hat{g}_{B1}'''(L) & -\hat{g}_{B2}'''(L) & -\hat{g}_{B3}'''(L) & -\hat{g}_{B4}'''(L) \\ \hat{g}_{B1}''(L) & \hat{g}_{B2}''(L) & \hat{g}_{B3}''(L) & \hat{g}_{B4}''(L) \end{bmatrix} \begin{Bmatrix} \hat{v}_1 \\ \hat{\phi}_1 \\ \hat{v}_2 \\ \hat{\phi}_2 \end{Bmatrix} \quad (3.43)$$

$\hat{M}_1, \hat{M}_2, \hat{V}_1$ and \hat{V}_2 are the spectral bending moments and shear forces at each end nodes of the element, which are equal to $-\hat{M}(0), \hat{M}(L), -\hat{V}(0)$ and $\hat{V}(L)$, respectively. The stiffness matrix is square, symmetric and complex valued.

3.2.2. Timoshenko Beam Theory

The time domain GDEMs related to Timoshenko beam theory are given in the equations 2.52 and 2.53. Spectral representation of the GDEM in matrix form is given as:

$$\begin{bmatrix} GAK_1k_B^2 - \rho A\omega^2 & -ik_BGAK_1 \\ ik_BGAK_1 & EIk_B^2 + GAK_1 - \rho IK_2\omega^2 \end{bmatrix} \begin{Bmatrix} \hat{v} \\ \hat{\phi} \end{Bmatrix} = \begin{Bmatrix} 0 \\ 0 \end{Bmatrix} \quad (3.44)$$

The roots of the characteristic equation of the matrix above gives the wavenumbers k_{B1} and k_{B2} , which are related to the first and the second mode of vibration.

Since shear deformations are considered in the Timoshenko beam theory, plane sections no longer remain plane, and the slope cannot be obtained by differentiating the vertical displacement with respect to spatial coordinate. Thus, a second independent variable is introduced.

$$\hat{v}(x) = AR_1e^{-ik_{B1}x} + BR_2e^{-ik_{B2}x} - CR_1e^{-ik_{B1}(L-x)} - DR_2e^{-ik_{B2}(L-x)} \quad (3.45)$$

$$\hat{\phi}(x) = Ae^{-ik_{B1}x} + Be^{-ik_{B2}x} + Ce^{-ik_{B1}(L-x)} + De^{-ik_{B2}(L-x)} \quad (3.46)$$

The amplitude ratios, R_1 and R_2 , are derived by using following formula,

$$R_i = \frac{ik_i GAK_1}{GAK_1 k_i^2 - \rho A \omega^2} \quad (3.47)$$

Dynamic shape functions can be derived in an analogous way to the Mindlin-Herrmann rod theory. The force-displacement relationship for a Timoshenko beam is given as,

$$\hat{V} = -EI \frac{d^2 \hat{\phi}}{dx^2} - \rho IK_2 \omega^2 \hat{\phi} \quad (3.48)$$

$$\hat{M} = EI \frac{d \hat{\phi}}{dx} \quad (3.49)$$

Dynamic stiffness matrix for Timoshenko beam can be constructed using the dynamic shape functions, $(\hat{g}_{B\phi i}(x))$, and the force-displacement relationships defined above. The form of the stiffness matrix is given below,

$$\begin{Bmatrix} \hat{V}_1 \\ \hat{M}_1 \\ \hat{V}_2 \\ \hat{M}_2 \end{Bmatrix} = \begin{bmatrix} EI \begin{bmatrix} \hat{g}_{B\phi 1}''(0) & \hat{g}_{B\phi 2}''(0) & \hat{g}_{B\phi 3}''(0) & \hat{g}_{B\phi 4}''(0) \\ -\hat{g}_{B\phi 1}'(0) & -\hat{g}_{B\phi 2}'(0) & -\hat{g}_{B\phi 3}'(0) & -\hat{g}_{B\phi 4}'(0) \\ -\hat{g}_{B\phi 1}''(L) & -\hat{g}_{B\phi 2}''(L) & -\hat{g}_{B\phi 3}''(L) & -\hat{g}_{B\phi 4}''(L) \\ \hat{g}_{B\phi 1}'(L) & \hat{g}_{B\phi 2}'(L) & \hat{g}_{B\phi 3}'(L) & \hat{g}_{B\phi 4}'(L) \end{bmatrix} \\ +\rho IK_2 \omega^2 \begin{bmatrix} \hat{g}_{B\phi 1}(0) & \hat{g}_{B\phi 2}(0) & \hat{g}_{B\phi 3}(0) & \hat{g}_{B\phi 4}(0) \\ 0 & 0 & 0 & 0 \\ -\hat{g}_{B\phi 1}(L) & -\hat{g}_{B\phi 2}(L) & -\hat{g}_{B\phi 3}(L) & -\hat{g}_{B\phi 4}(L) \\ 0 & 0 & 0 & 0 \end{bmatrix} \end{bmatrix} \begin{Bmatrix} \hat{v}_1 \\ \hat{\phi}_1 \\ \hat{v}_2 \\ \hat{\phi}_2 \end{Bmatrix} \quad (3.50)$$

3.2.3. Comparison of the Beam Theories

In this section, Bernoulli-Euler and Timoshenko beam theories are compared by means of spectrum and dispersion relationships. Then, the terms of spectral element matrices of these two theories are compared to the stiffness matrices obtained theoretically and to those of the classical finite element analysis.

The phase and the group velocities related to the Bernoulli-Euler beam theory are derived as given by Eq. 3.51. The group velocity for the Timoshenko beam theory can be calculated using Eq. 3.34.

$$c = \frac{\omega}{k} = \sqrt{\omega} \left[\frac{EI}{\rho A} \right]^{1/4}; c_g = \frac{d\omega}{dk} = 2\sqrt{\omega} \left[\frac{EI}{\rho A} \right]^{1/4} \quad (3.51)$$

Timoshenko beam theory does not introduce additional modes when compared to Bernoulli-Euler beam theory. However, since the shear deformations and the rotational inertia are considered, the behavior of each mode is changed. With the introduction of the shear deformations, slope becomes an independent variable. One of the significant differences between these two beam theories is the presence of second propagating mode with a cut-off frequency [2]. The cut-off frequency, where the wavenumber is equal to zero, can be found to be:

$$\omega_c = \sqrt{\frac{GAK_1}{\rho IK_2}} \quad (3.52)$$

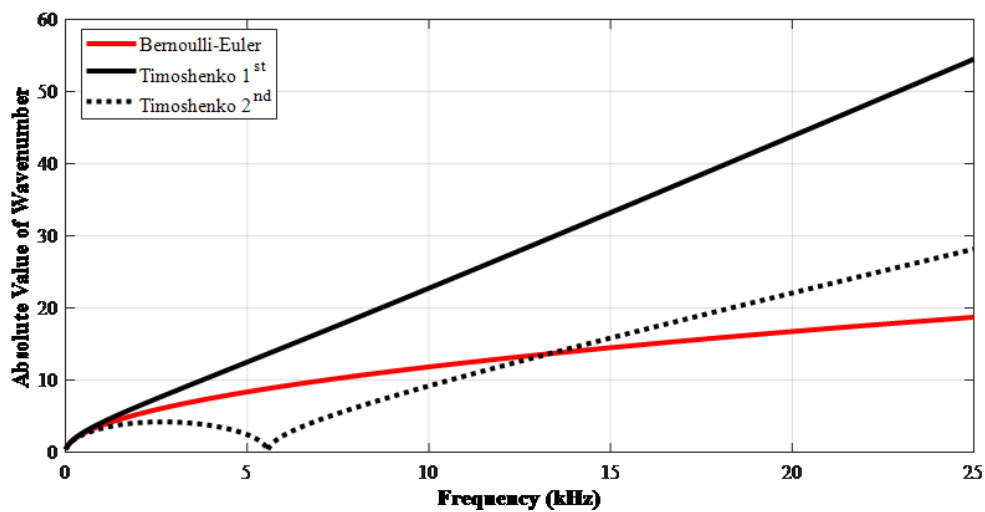


Figure 3.7. Spectrum relationship for Bernoulli-Euler and Timoshenko beam theories.

Figure 3.7 shows the spectrum relations for the Bernoulli-Euler and Timoshenko beam theories. As can be seen from the figure, the behavior of the wave modes is

similar for the low frequency range. Beyond the cut-off frequency, the second mode of the Timoshenko beam begins to propagate, and the behavior related to these two beam theories becomes different from each other.

Figure 3.8 shows the dispersion relationship of the Bernoulli-Euler and Timoshenko beams. The vertical axis is the ratio between the group velocity and longitudinal wave speed. As can be seen from the figure, in high frequency range Bernoulli-Euler beam theory produces very high speeds. The second mode of the Timoshenko beam starts to propagate at the cut-off frequency, and becomes asymptotic to a higher speed [11].

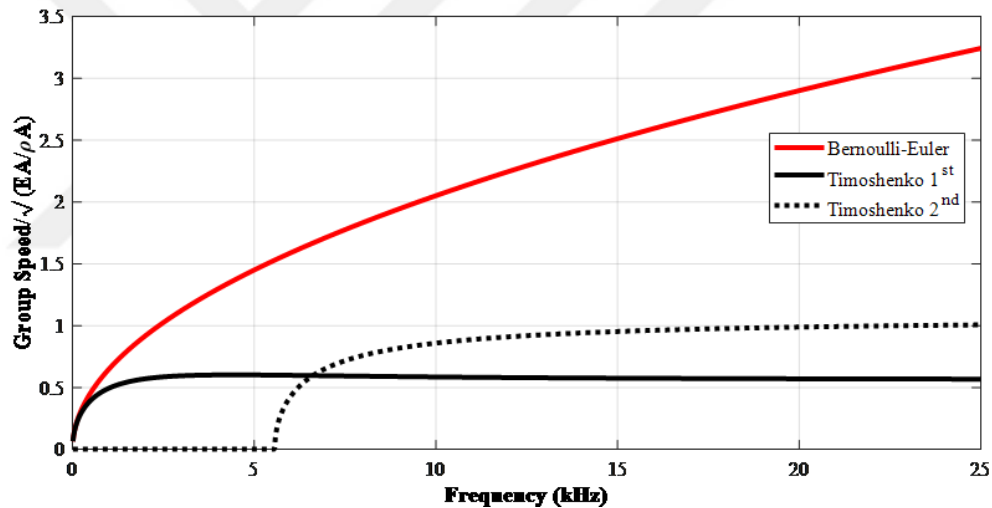


Figure 3.8. Dispersion relationship for Bernoulli-Euler and Timoshenko beam theories.

Figure 3.9 shows the stiffness term k_{11} according to the conventional, theoretical, Bernoulli-Euler and Timoshenko beam theories. The stiffness of the conventional beam is obtained as follows [6],

$$\mathbf{K} = \frac{EI}{L^3} \begin{bmatrix} 12 & 6L & -12 & 6L \\ 6L & 4L^2 & -6L & 2L^2 \\ -12 & -6L & 12 & -6L \\ 6L & 2L^2 & -6L & 4L^2 \end{bmatrix} - \frac{\rho AL\omega^2}{420} \begin{bmatrix} 156 & 22L & 54 & -13L \\ 22L & 4L^2 & 13L & -3L^2 \\ 54 & 13L & 156 & -22L \\ -13L & -3L^2 & -22L & 4L^2 \end{bmatrix} \quad (3.53)$$

The theoretical stiffness matrix is obtained using the general solution to the ordinary differential equation, and is given by Eq. 3.54 [19].

$$\mathbf{K} = \frac{EI}{L^3} \begin{bmatrix} k_{11} & k_{12} & k_{13} & k_{14} \\ k_{21} & k_{22} & k_{23} & k_{24} \\ k_{31} & k_{32} & k_{33} & k_{34} \\ k_{41} & k_{42} & k_{43} & k_{44} \end{bmatrix} \quad (3.54)$$

where,

$$\bar{L} = k_B L$$

$$\Delta_B = \frac{1}{1 - (\cos \bar{L} \cosh \bar{L})}$$

$$k_{11} = \Delta_B \bar{L}^3 (\cos \bar{L} \sinh \bar{L} + \sin \bar{L} \cosh \bar{L}) = k_{33}$$

$$k_{22} = \Delta_B \bar{L}^3 k_B^{-2} (-\cos \bar{L} \sinh \bar{L} + \sin \bar{L} \cosh \bar{L}) = k_{44}$$

$$k_{12} = \Delta_B \bar{L}^3 k_B^{-1} (\sin \bar{L} \sinh \bar{L}) = k_{21} = -k_{34} = -k_{43}$$

$$k_{13} = -\Delta_B \bar{L}^3 (\sin \bar{L} + \sinh \bar{L}) = k_{31}$$

$$k_{14} = \Delta_B \bar{L}^3 k_B^{-1} (-\cos \bar{L} + \cosh \bar{L}) = k_{41} = -k_{23} = -k_{32}$$

$$k_{24} = \Delta_B \bar{L}^3 k_B^{-2} (-\sin \bar{L} + \sinh \bar{L}) = k_{42}$$

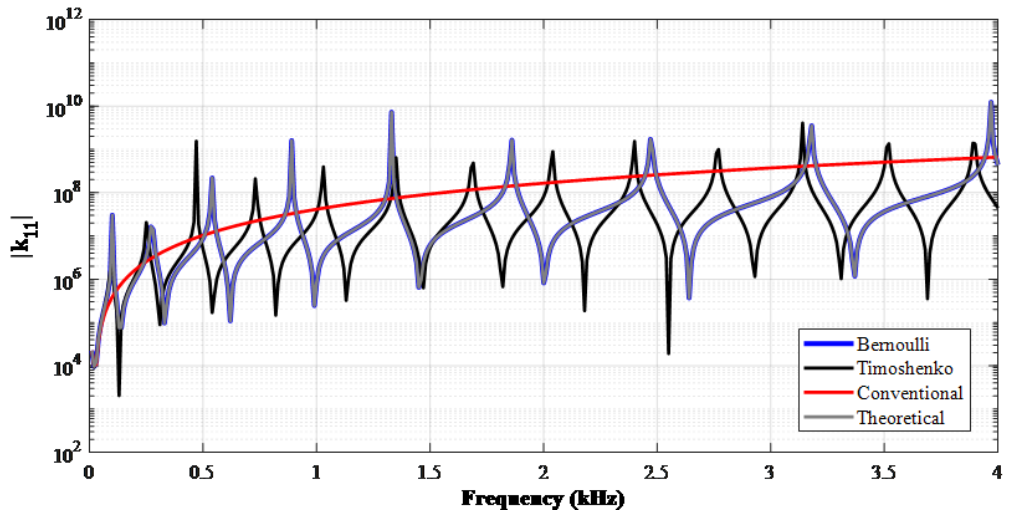


Figure 3.9. k_{11} values according to conventional, theoretical, Bernoulli-Euler and Timoshenko beam theories.

The dynamic stiffness matrix is symmetric, and in general complex valued. All of the beam models have the same characteristics in the low frequency range. However, they differ from each other as the frequency increases. If the member is not a small sized member, they will differ from each other at lower frequencies, too. The stiffness terms related to conventional beam theory show only one zero-crossing, while the others show many zero-crossings. The stiffness term of the conventional beam continues to infinity when the frequency increases.

3.3. Assemblage of Spectral Element Matrices

The arbitrarily oriented elements that form the plane frame are assembled using a procedure analogous to FEM. The joints, where two or more elements intersect with each other, are assumed to be rigid and massless. The interactions between longitudinal and flexural deflections are neglected since the small deflection theory is adopted in the formulation. Therefore, stiffness matrix of each element is obtained by the superposition of the spectral element matrices of a rod and a beam element in the local coordinate system. Spectral element matrices of each element transformed into global coordinates, and assembled to form the plane frame. The spectral element matrix of an element in local coordinate system is obtained as follows:

$$\left\{ \begin{array}{c} \hat{F}_1 \\ \hat{V}_1 \\ \hat{M}_1 \\ \hat{F}_2 \\ \hat{V}_2 \\ \hat{M}_2 \end{array} \right\} = \left[\begin{array}{c} EA \\ +EI \end{array} \left[\begin{array}{cccccc} \hat{k}_{R11} & 0 & 0 & \hat{k}_{R12} & 0 & 0 \\ 0 & 0 & 0 & 0 & 0 & 0 \\ 0 & 0 & 0 & 0 & 0 & 0 \\ \hat{k}_{R21} & 0 & 0 & \hat{k}_{R22} & 0 & 0 \\ 0 & 0 & 0 & 0 & 0 & 0 \\ 0 & 0 & 0 & 0 & 0 & 0 \\ 0 & \hat{k}_{B11} & \hat{k}_{B12} & 0 & \hat{k}_{B13} & \hat{k}_{B14} \\ 0 & \hat{k}_{B21} & \hat{k}_{B22} & 0 & \hat{k}_{B23} & \hat{k}_{B24} \\ 0 & 0 & 0 & 0 & 0 & 0 \\ 0 & \hat{k}_{B31} & \hat{k}_{B32} & 0 & \hat{k}_{B33} & \hat{k}_{B34} \\ 0 & \hat{k}_{B41} & \hat{k}_{B42} & 0 & \hat{k}_{B43} & \hat{k}_{B44} \end{array} \right] \right\} \left\{ \begin{array}{c} \hat{u}_1 \\ \hat{v}_1 \\ \hat{\phi}_1 \\ \hat{u}_2 \\ \hat{v}_2 \\ \hat{\phi}_2 \end{array} \right\} \quad (3.55)$$

The resultant forces and moments are represented by \hat{F} , \hat{V} and \hat{M} . The subscripts 1 and 2 corresponds to the i^{th} and j^{th} end of the member, respectively. EA is the axial stiffness and EI is the flexural stiffness of the member. The stiffness matrix terms of a rod and a beam are represented by \hat{k}_{Rij} and \hat{k}_{Bij} , respectively.

Since the elements of a plane frame are oriented arbitrarily, each spectral element matrix is constructed in the local coordinate system of the concerned member. Before the assemblage process, spectral element matrices of each individual element in local coordinate system must be transformed into global coordinate system in order to express the nodal DOFs in global coordinates. The global transformation is done by using the following transformation matrix

$$\mathbf{T} = \begin{bmatrix} \cos \theta & \sin \theta & 0 & 0 & 0 & 0 \\ -\sin \theta & \cos \theta & 0 & 0 & 0 & 0 \\ 0 & 0 & 1 & 0 & 0 & 0 \\ 0 & 0 & 0 & \cos \theta & \sin \theta & 0 \\ 0 & 0 & 0 & -\sin \theta & \cos \theta & 0 \\ 0 & 0 & 0 & 0 & 0 & 1 \end{bmatrix} \quad (3.56)$$

Spectral element matrix in global coordinates is then obtained as,

$$\hat{\mathbf{K}}_g = \mathbf{T}^T \hat{\mathbf{K}} \mathbf{T} \quad (3.57)$$

Spectral element matrix of the structure is constructed by assembling global dynamic stiffness matrices of each individual element at each frequency. Spectral element matrix of the system should be rearranged and renumbered in order to account for the boundary conditions and prescribed forces. Then, the spectral element matrices corresponding to each element of the structure are assembled. If the displacements at a node are known to be equal to zero, then the rows and columns related to these zero DOFs can be eliminated from the spectral element matrix and the reduced spectral element matrix can be formed using the non-zero DOFs. In some cases, the displace-

ments at a node are known and not equal to zero. Thus, the known terms cannot be eliminated from the stiffness matrix. In spite of eliminating the known terms, they are grouped as known and unknown displacements / forces as seen below.

$$\begin{Bmatrix} \hat{\mathbf{F}}_k \\ \hat{\mathbf{F}}_u \end{Bmatrix} = \begin{bmatrix} \hat{\mathbf{K}}_{guu} & \hat{\mathbf{K}}_{guk} \\ \hat{\mathbf{K}}_{gku} & \hat{\mathbf{K}}_{gkk} \end{bmatrix} \begin{Bmatrix} \hat{\mathbf{u}}_u \\ \hat{\mathbf{u}}_k \end{Bmatrix} \quad (3.58)$$

In equation 3.58, subscript k refers to known quantities and u refers to unknown quantities. Unknown displacements and forces can be found by solving the system of equation given above. In case of base excitation, *penalty method* is adopted to impose the displacement produced by the excitation to the related DOFs. This method is implemented by adding a spring with a large stiffness to the related DOFs and defining a load that produces the required displacement at that DOFs [20].

Displacement response at an arbitrary point of a member at any frequency can be found by the multiplication of the frequency dependent shape functions and the nodal displacements of the concerned element at the related frequency.

The damping can be introduced in the form of hysteretic damping. It can be done by replacing the elasticity modulus of the system with a complex-valued one as follows,

$$E_d = E(1 + 2i\zeta) \quad (3.59)$$

Hysteretic damping is also referred as the rate-independent damping, or structural damping, and it can easily be applied in the frequency domain analysis. It represents both the elastic and damping forces at the same time [21].

3.4. Numerical Example

As an example, the dynamic response of a five-story, two-bay plane frame is calculated by using both FEM and SEM. The aim is to demonstrate the accuracy of SEM in the medium to high frequency range. Since, it is known that the accuracy of FEM analysis increases with the decreasing mesh size, two different FEM models are used in the analysis. In the first FEM model, structural elements without any kind of discontinuity are modeled as a single element. In the second FEM model, each structural member is divided into 100 segments. Moreover, two SEM models are constructed in order to see the effect of adopting higher order theories on the calculated dynamic response. In the first SEM model, structural elements are formulated based on elementary theories. In the second SEM model higher order theories, namely Love rod and Timoshenko beam theories, are adopted. Mindlin-Herrmann and Three-Mode rod theories are not employed in the analyses, since they introduce extra DOFs, and the frequency range considered does not cover the cut-off frequency. A MATLAB-based code [22] is prepared for the SEM analysis. SAP2000 v.19 [23] is utilized for FEM analysis. The dynamic response is calculated under the effect of the self-weight of the structure and the applied base excitation. The structure is excited in the global x direction through its base. The time and the frequency domain properties of the applied base excitation is given in Figure 3.10 and Figure 3.11, respectively.

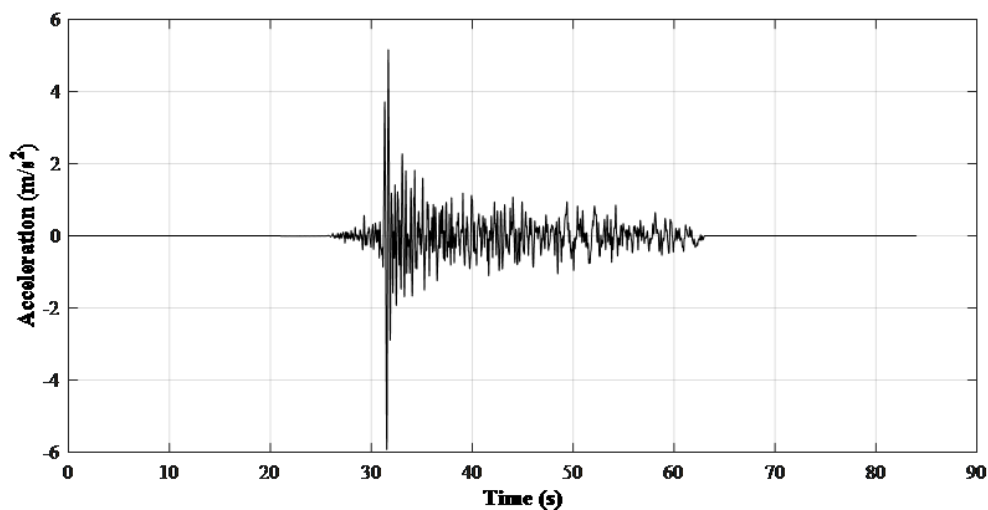


Figure 3.10. Time domain representation of applied base acceleration.

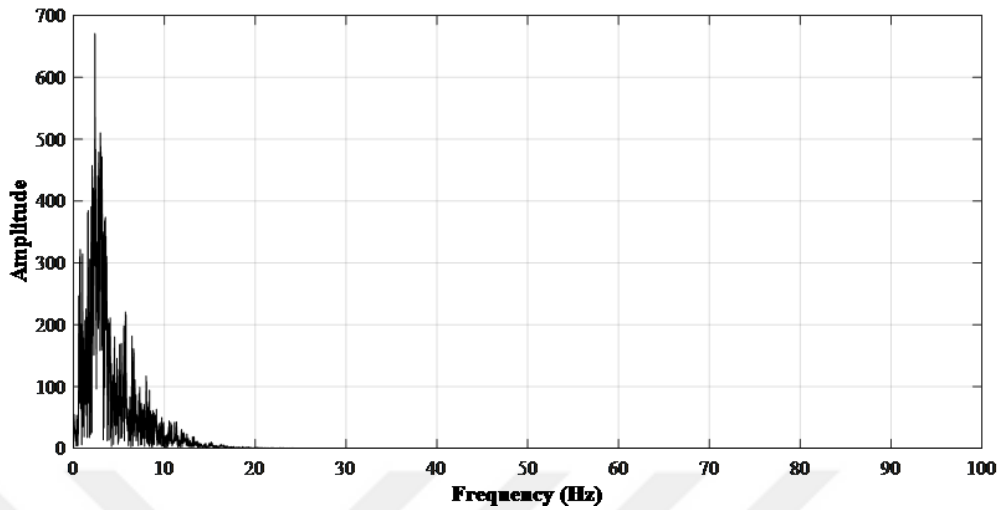


Figure 3.11. Frequency domain representation of applied base acceleration.

Figure 3.12 shows the geometric properties and the assigned DOF numbers. The story height and the bay width of the plane frame are 3m and 5m, respectively. The dimensions of the columns are identical at 0.60*0.60 m. The beam dimensions are selected as 0.30*0.60 m. The material is selected as C25 concrete class whose Young's modulus, mass density and Poisson's ratio of the material are given as, 30 GPa , 2.4 g/cm^3 and 0.2, respectively.

The structural damping with 5% damping ratio (ζ) is introduced to the system. It is applied by replacing the elasticity modulus of the system with a complex value as given in the Eq. 3.59.

The Fourier Amplitude Spectra (FAS) of the dynamic response at DOF= 52, which corresponds to the top displacement in the direction of the excitation, is presented in Figure 3.13. In this figure, FAS of the calculated response within the frequency range of 0-50 Hz is shown by using the first FEM, the second FEM, the first SEM and the second SEM models. In the low frequency range, the responses calculated from the four analyses are almost identical. However, as the frequency increases, the calculated responses start diverging.

For a better understanding, the dynamic response calculated from the four anal-

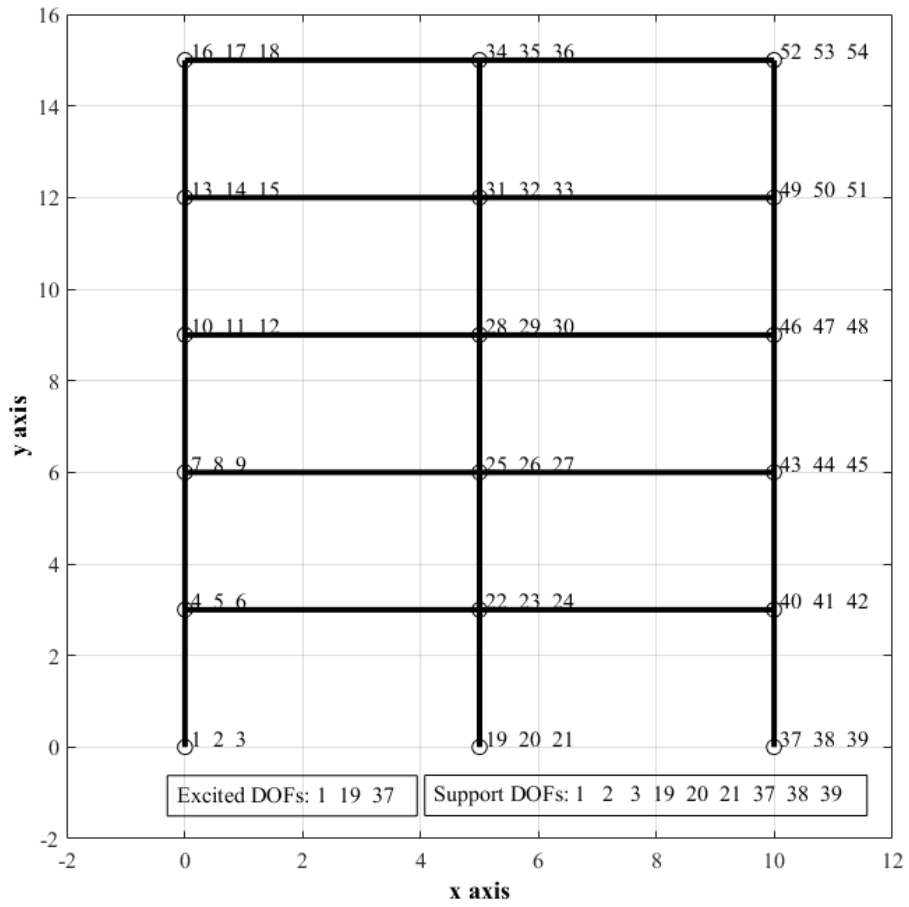


Figure 3.12. Geometry and DOFs numbers of the example structure.

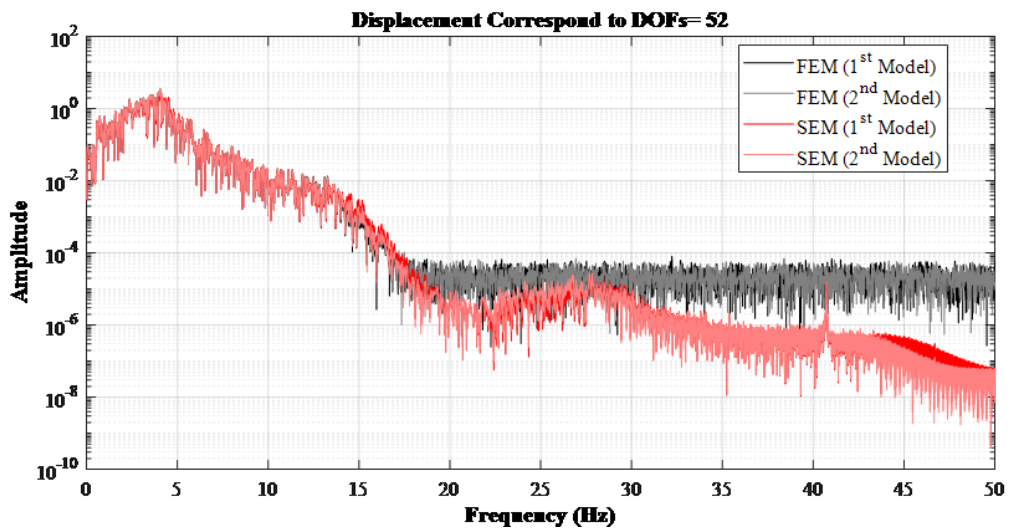


Figure 3.13. FAS of the response at DOF= 52 between 0-50 Hz.

yses between the frequency ranges of 0-10 Hz., 10-15 Hz. and 15-20 Hz. are illustrated in Figure 3.14, Figure 3.15 and Figure 3.16, respectively.

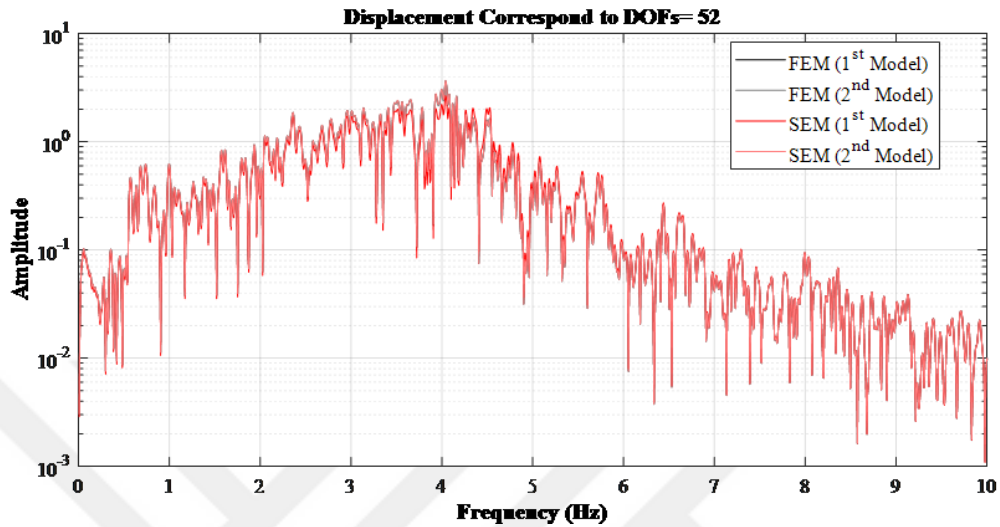


Figure 3.14. FAS of the response at DOFs 50 between 0-10 Hz.

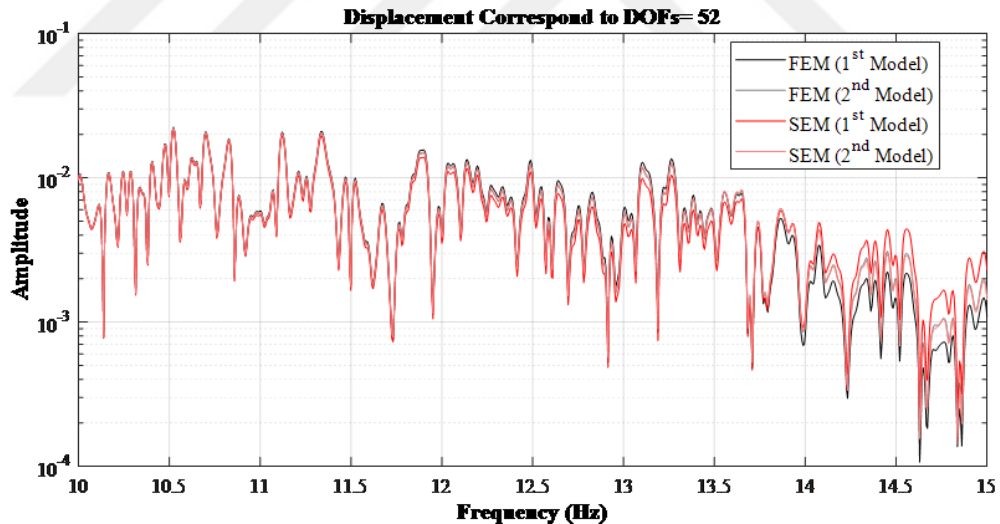


Figure 3.15. FAS of the response at DOF= 52 between 10-15 Hz.

In the low frequency range, which is presented in Figure 3.14, the dynamic response calculated at DOF= 52 from the four of the analysis are approximately identical. As can be seen from Figure 3.15, in the vicinity of 12 Hz. the response calculated from the first FEM analysis starts diverging from the others. As the frequency increases, the response obtained from the second SEM model is also diverges from the response obtained from the second FEM and the first SEM. In the vicinity of 16 Hz. the dynamic response at DOF= 52 calculated from the first SEM deviate from the second

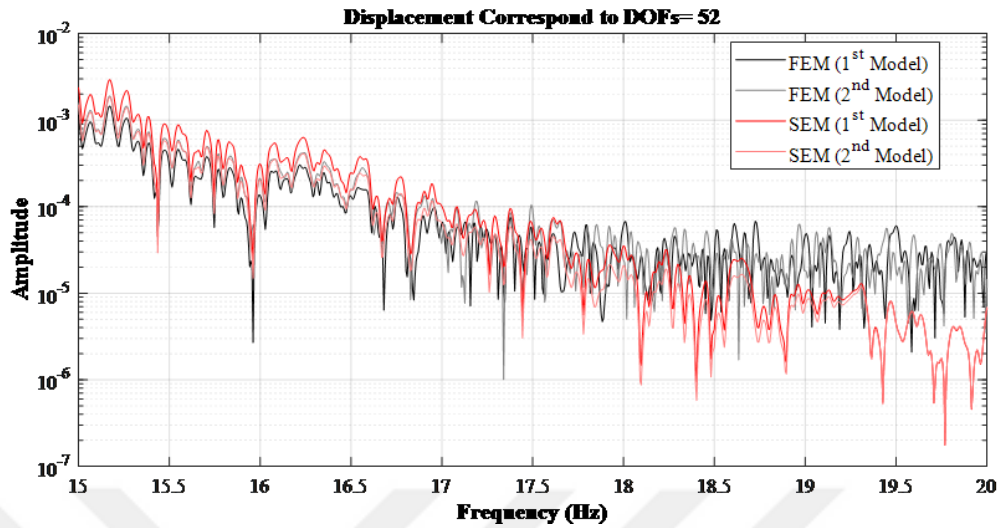


Figure 3.16. FAS of the response at DOF= 52 between 15-20 Hz.

FEM. Beyond 18 Hz., the responses calculated from the SEM and FEM models differ significantly.

The time-domain response can be calculated by taking the inverse Fourier transform of the response calculated in the frequency domain. Figure 3.17 and Figure 3.18 illustrates the comparison of the calculated time domain responses obtained from the four analyses. The response is band-pass filtered between 0.1-5 Hz. and 15-20 Hz. in order to reflect the differences in the low and high frequency ranges. The response in the low frequency range is identical for four of the analysis. However, as the frequency increases they differ considerably.

Resultant forces can also be calculated both in the frequency and time domains using SEM. Figure 3.19, Figure 3.20, Figure 3.21 and Figure 3.22 show the variation in the base shear with respect to time between 8-17 s., 17-26 s., 26-35 s. and 35-44 s., respectively. The base shear calculated from the four models differ from each other throughout the time interval.

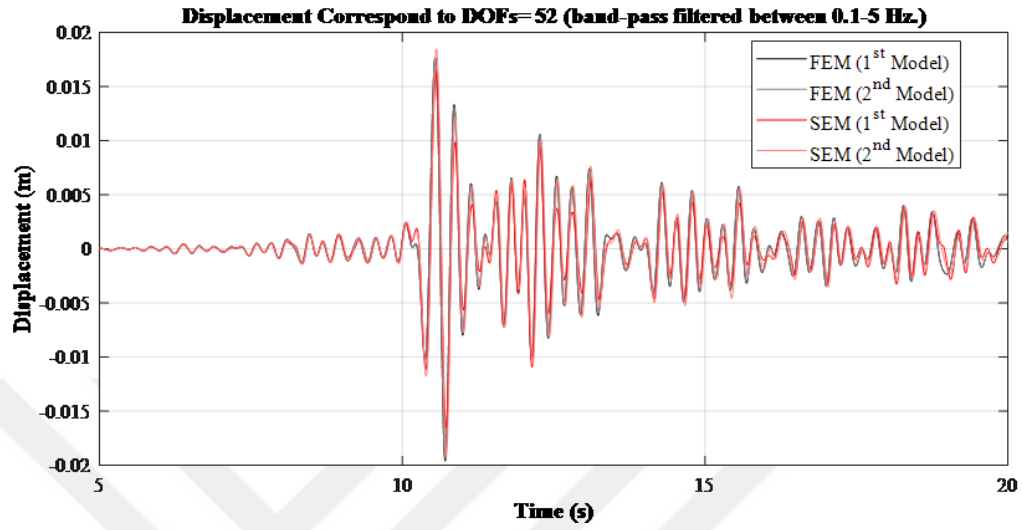


Figure 3.17. Band pass filtered between 0.1-5 Hz. time domain response at DOF= 52 between 5-20 sec.

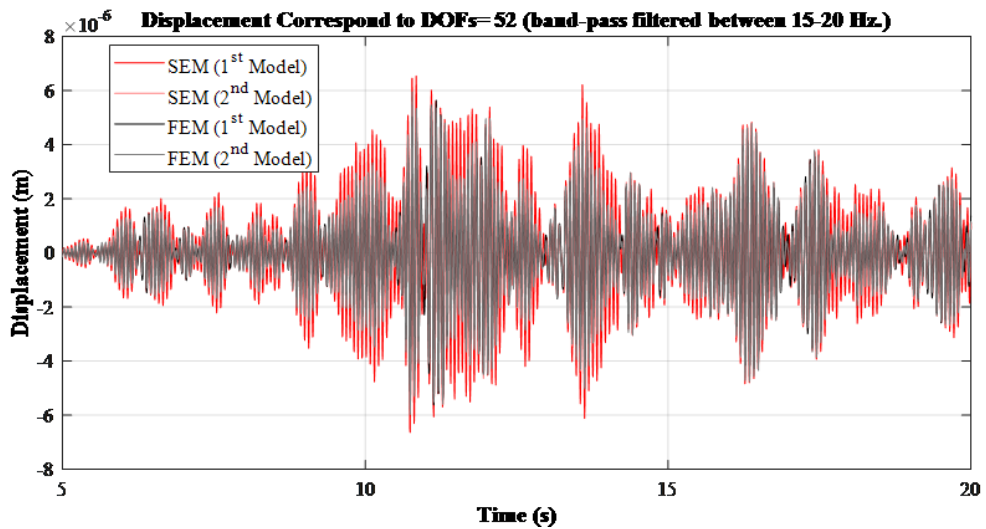


Figure 3.18. Band pass filtered between 15-20 Hz. time domain response at DOF= 52 between 5-20 sec.

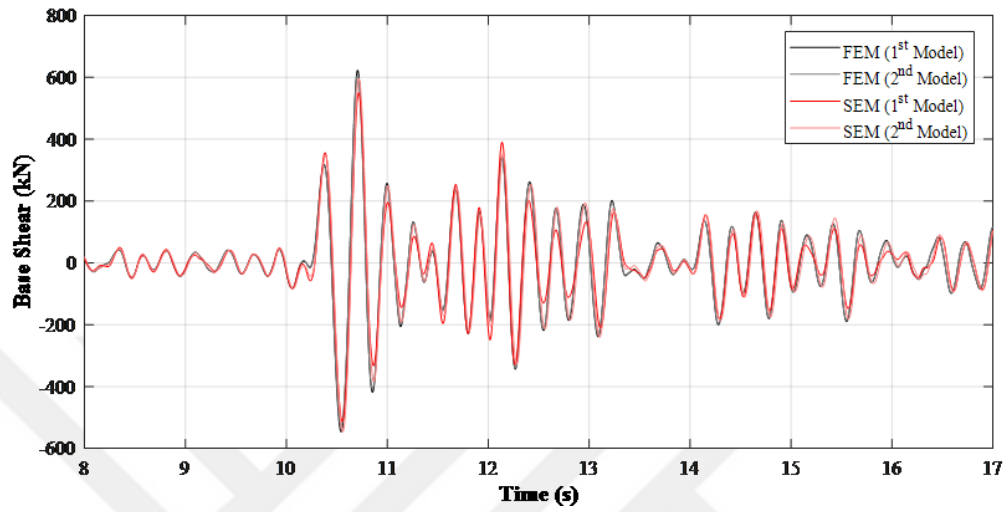


Figure 3.19. Variation in base shear with respect to time (between 8-17 sec.).

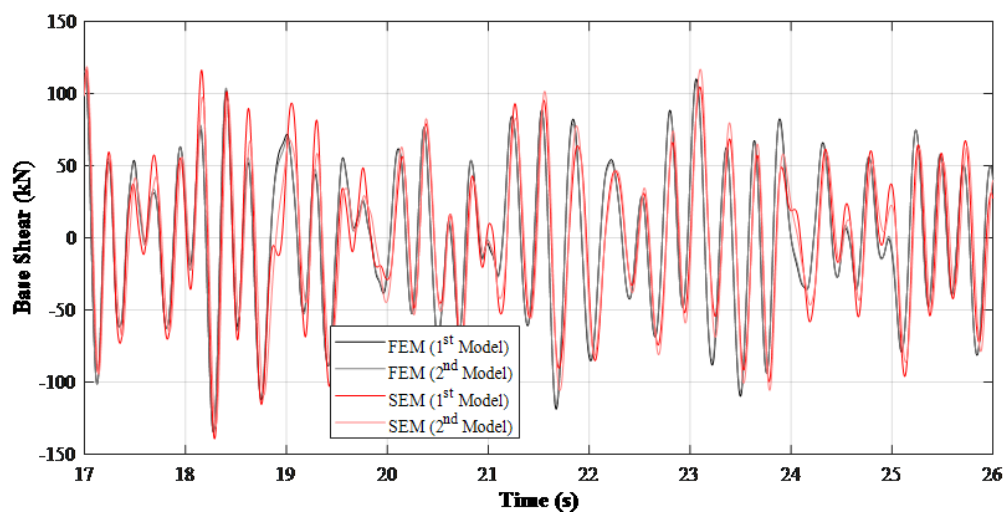


Figure 3.20. Variation in base shear with respect to time (between 17-26 sec.).

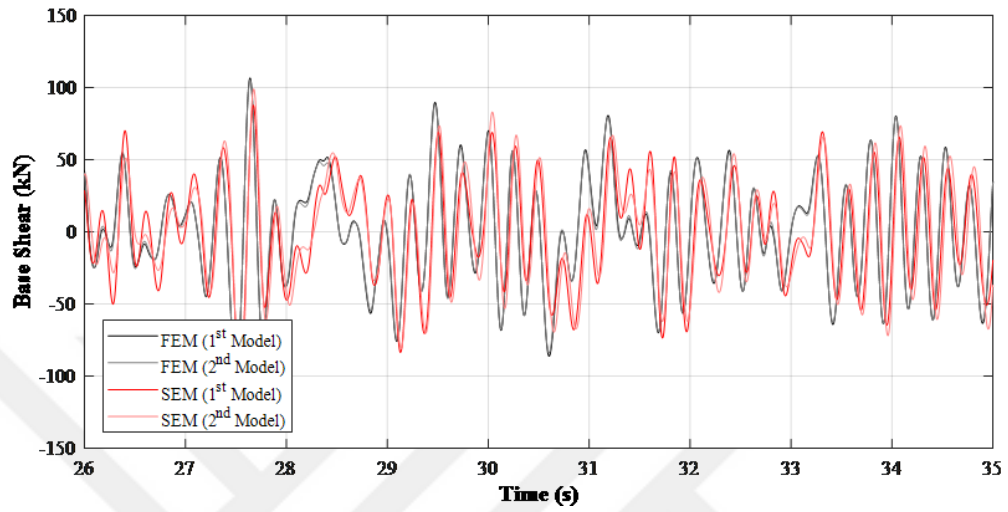


Figure 3.21. Variation in base shear with respect to time (between 26-35 sec.).

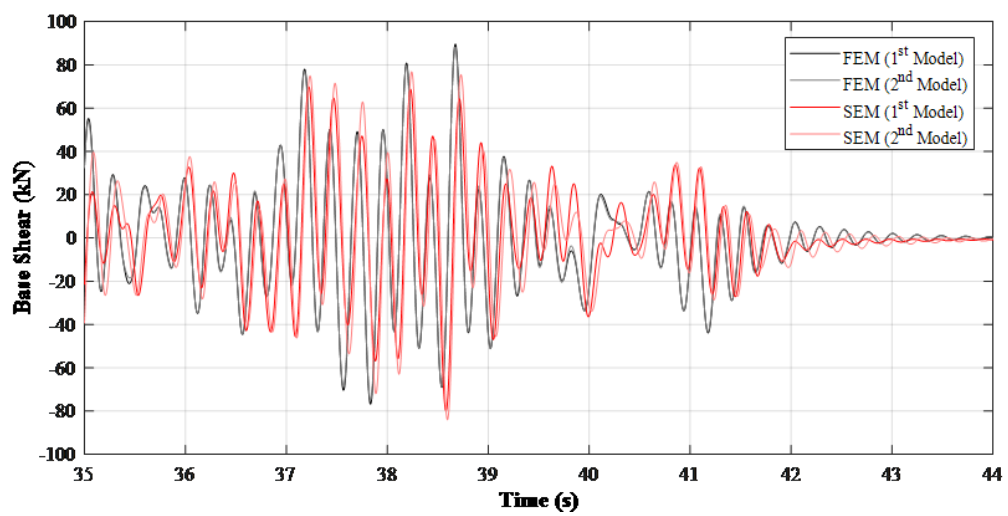


Figure 3.22. Variation in base shear with respect to time (between 35-44 sec.).

4. TRAVELLING WAVE METHOD

The propagation properties of waves through the elements (i.e., waveguides) of a structure can be utilized to study its dynamic behavior. In the medium to high frequency ranges, this method yields accurate results. In contrast to SEM, the propagation path of the disturbance can also be tracked. Wave propagation solutions are based on the propagation, reflection, transmission and generation properties at the discontinuities. A discontinuity, such as a joint, can be treated as a filter. It changes the amplitudes of the incident waves and can generate additional waves. Thus, the reflection, transmission, and the wave generation characteristics of joints are the vital elements of the wave propagation analysis. Assemblage of these properties provides a concise method to analyze dynamic behavior of structures. The amplitudes of the reflected and transmitted waves are related to the incident waves by means of the transmission and reflection coefficients. Any type of incident wave can generate a new type of different waves at the discontinuities. For instance, a flexural wave can generate a longitudinal wave, or conversely, a longitudinal wave can generate a flexural wave.

The propagation of waves in structures have been extensively studied more than half a century. Graff [24] and Cramer, Heckl and Petersson [25] described vibration of elastic structures in terms of the reflections and transmissions of the incident wave at discontinuities. Doyle [14] derived solutions for wave propagation in one-dimensional waveguides. The transmission and reflection coefficients at different types of joints are studied by many researchers. Mace [26] and Milne [27] presented reflection and transmission properties at a joint based on the Bernoulli-Euler beam theory. Mei and Mace [28] considered wave propagation in Timoshenko beams, and transmission and reflection properties at an L type junction. The effect of structural joints on the wave propagation is studied by Doyle and Kamle [29, 30], based on experiments. Mei [31] studied wave propagation in space frames.

Nagem and Williams [32] developed a matrix methodology for planar structures. In their method, system matrices are constructed using the transfer matrices of the

elements and joint coupling matrices. Howard and Pao [33] introduced reverberation ray matrix method. The method uses dual coordinate system to form system matrix in global coordinates and Fourier transforms. Mace, Duhamel, Brennan and Hinke [34] utilized wave finite element method. A vast amount of literature on this method can be found in the paper published by Waki, Mace and Brennan [35]. Von Flotow [36], and Miller and Von Flotow [37] developed a method called as Travelling Wave Method (TWM). According to Mei and Mace [28], the TWM has proved to be powerful for analyzing vibrations in complex structural networks. Beale and Accorsi [38], generalized the TWM to apply it in two and three-dimensional frames.

In TWM, the wave guide equations are derived in terms of the left and right propagating waves. Left and right directions of a member are arbitrary. The waves traveling in the direction of increasing spatial coordinate with respect to the member's corresponding local coordinate system are referred as the right propagating, and the waves traveling in the opposite direction are referred as the left propagating.

The waveguide equation, which relates the wave mode amplitudes to the generalized displacements and forces, is expressed as follows:

$$\begin{Bmatrix} \mathbf{U} \\ \mathbf{F} \end{Bmatrix} = \begin{bmatrix} \mathbf{Y}_{uR} & \mathbf{Y}_{uL} \\ \mathbf{Y}_{fR} & \mathbf{Y}_{fL} \end{bmatrix} \begin{Bmatrix} \mathbf{u}_R \\ \mathbf{u}_L \end{Bmatrix} \quad (4.1)$$

where, \mathbf{U} and \mathbf{F} represent the generalized displacement and force vectors, respectively, and \mathbf{u}_R and \mathbf{u}_L are the vectors of right and left propagating waves. The generalized positive displacements have the same direction at both ends of the member. However, positive forces have opposite directions. Basic steps of the general procedure for TWM is illustrated in Figure 4.1.

In the following sections, waveguide equations for longitudinal and flexural wave propagation are obtained based on various element theories.

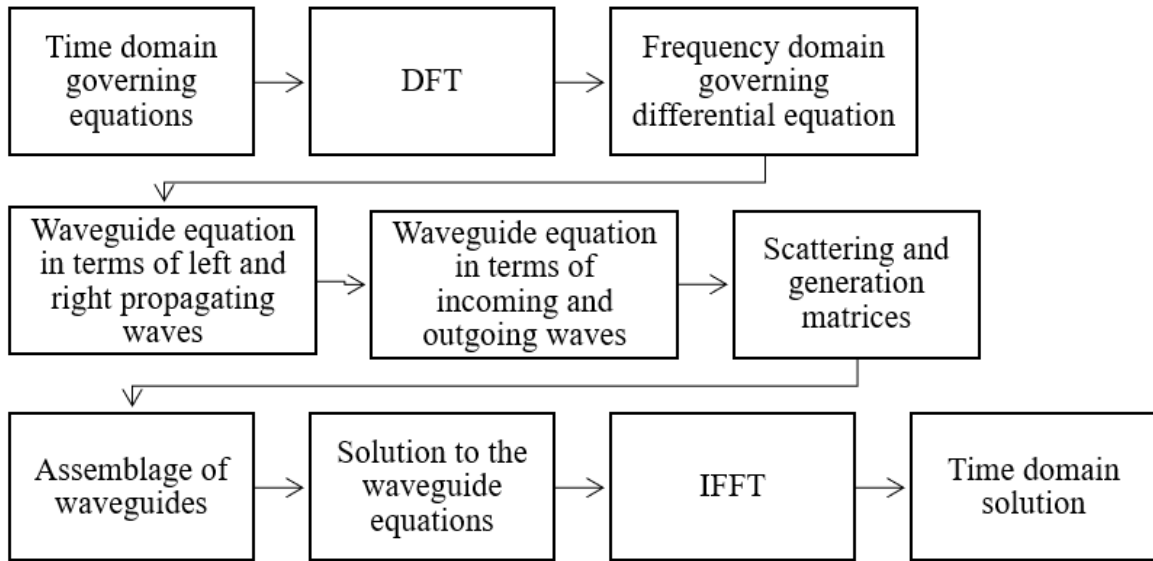


Figure 4.1. General procedure for TWM.

4.1. Longitudinal Wave Propagation

In this section, wave propagation equations for the four element theories mentioned earlier are obtained to derive reflection, transmission and generation relations.

4.1.1. Elementary Rod Theory

Wave solution to the governing differential equation in terms of spectral representation is given by Eq. 3.6. The same equation can be rewritten in terms of left and right propagating wave modes, as shown below:

$$\tilde{u}(x) = u_R e^{-ik_R x} + u_L e^{ik_R x} \quad (4.2)$$

Using force-displacement relationship given by Eq. 2.4, internal forces developed at an arbitrary point is derived as follows,

$$\tilde{F}(x) = EA(-ik_R u_R e^{-ik_R x} + ik_R u_L e^{ik_R x}) \quad (4.3)$$

Waveguide equations for the longitudinal wave modes, based on elementary rod theory, become

$$\begin{Bmatrix} \tilde{u}(x) \\ \tilde{F}(x) \end{Bmatrix} = \begin{bmatrix} 1 & 1 \\ -ik_R EA & ik_R EA \end{bmatrix} \begin{Bmatrix} u_R \\ u_L \end{Bmatrix} \quad (4.4)$$

4.1.2. Love Rod Theory

Spectral representation of the solution to the governing differential equation of motion based on Love rod theory is given by Eq. 3.11. In terms of right and left propagating waves, the equation becomes,

$$\tilde{u}(x) = u_R e^{-ik_R x} + u_L e^{ik_R x} \quad (4.5)$$

Using the force displacement relationship, internal force is described as,

$$\tilde{F}(x) = (-ik_R EA - \nu^2 \omega^2 \rho J) u_R e^{-ik_R x} + (ik_R EA - \nu^2 \omega^2 \rho J) u_L e^{ik_R x} \quad (4.6)$$

Waveguide equations for the longitudinal wave modes, based on elementary rod theory, become

$$\begin{Bmatrix} \tilde{u}(x) \\ \tilde{F}(x) \end{Bmatrix} = \begin{bmatrix} 1 & 1 \\ -ik_R EA - \nu^2 \omega^2 \rho J & ik_R EA - \nu^2 \omega^2 \rho J \end{bmatrix} \begin{Bmatrix} u_R \\ u_L \end{Bmatrix} \quad (4.7)$$

4.1.3. Mindlin-Herrmann Rod Theory

Wave solution to governing differential equations in terms of spectral representation is given by the equations 3.16 and 3.17. The same equation, in terms of the left

and right propagating wave modes, is rewritten by the following equations:

$$\tilde{u}(x) = R_1 u_{R1} e^{-ik_{R1}x} + R_2 u_{R2} e^{-ik_{R2}x} - R_1 u_{L1} e^{ik_{R1}x} - R_2 u_{L2} e^{ik_{R2}x} \quad (4.8)$$

$$\tilde{\psi}(x) = u_{R1} e^{-ik_{R1}x} + u_{R2} e^{-ik_{R2}x} + u_{L1} e^{ik_{R1}x} + u_{L2} e^{ik_{R2}x} \quad (4.9)$$

Using the force-displacement relationship given by equations 3.19 and 3.20, internal forces developed in the section are calculated as,

$$\begin{aligned} \tilde{F}(x) &= (-ik_{R1}R_1T_1 + T_2) u_{R1} e^{-ik_{R1}x} + (-ik_{R2}R_2T_1 + T_2) u_{R2} e^{-ik_{R2}x} \\ &+ (-ik_{R1}R_1T_1 + T_2) u_{L1} e^{ik_{R1}x} + (-ik_{R2}R_2T_1 + T_2) u_{L2} e^{ik_{R2}x} \end{aligned} \quad (4.10)$$

$$\tilde{Q}(x) = T_3 (-ik_{R1}u_{R1} e^{-ik_{R1}x} - ik_{R2}u_{R2} e^{-ik_{R2}x} + ik_{R1}u_{L1} e^{ik_{R1}x} + ik_{R2}u_{L2} e^{ik_{R2}x}) \quad (4.11)$$

where, T_1 , T_2 and T_3 are given in Eq. 3.15. T_7 and T_8 of Eq. 4.13 are calculated as:

$$T_7 = ik_{R1}R_1; T_8 = ik_{R2}R \quad (4.12)$$

Waveguide equations for the longitudinal wave modes, based on Mindlin-Herrmann rod theory, become:

$$\begin{Bmatrix} \tilde{u}(x) \\ \tilde{\psi}(x) \\ \tilde{F}(x) \\ \tilde{Q}(x) \end{Bmatrix} = \begin{bmatrix} R_1 & R_2 & -R_1 & -R_2 \\ 1 & 1 & 1 & 1 \\ -T_7T_1 + T_2 & -T_8T_1 + T_2 & -T_7T_1 + T_2 & -T_8T_1 + T_2 \\ -ik_{R1}T_3 & -ik_{R2}T_3 & ik_{R1}T_3 & ik_{R2}T_3 \end{bmatrix} \begin{Bmatrix} u_{R1} \\ u_{R2} \\ u_{L1} \\ u_{L2} \end{Bmatrix} \quad (4.13)$$

4.1.4. Three-Mode Rod Theory

Spectral representation of the solution to the governing differential equation of motion based on Three-Mode rod theory is given by the equations from 3.22 to 3.24.

In terms of the right and left propagating waves, the equations become:

$$\begin{aligned}\tilde{u}(x) = & R_4 u_{R1} e^{-ik_{R1}x} + R_5 u_{R2} e^{-ik_{R2}x} + R_6 u_{R3} e^{-ik_{R3}x} + R_4 u_{R1} e^{ik_{R1}x} \\ & + R_5 u_{R2} e^{ik_{R2}x} + R_6 u_{R3} e^{ik_{R3}x}\end{aligned}\quad (4.14)$$

$$\begin{aligned}\tilde{\psi}(x) = & R_1 u_{R1} e^{-ik_{R1}x} + R_2 u_{R2} e^{-ik_{R2}x} + R_3 u_{R3} e^{-ik_{R3}x} - R_1 u_{R1} e^{ik_{R1}x} \\ & - R_2 u_{R2} e^{ik_{R2}x} - R_3 u_{R3} e^{ik_{R3}x}\end{aligned}\quad (4.15)$$

$$\tilde{\phi}(x) = u_{R1} e^{-ik_{R1}x} + u_{R2} e^{-ik_{R2}x} + u_{R3} e^{-ik_{R3}x} + u_{R1} e^{ik_{R1}x} + u_{R2} e^{ik_{R2}x} + u_{R3} e^{ik_{R3}x}\quad (4.16)$$

Using the relation between forces and displacements, given by equations 3.27 to 3.29, waveguide equations can be obtained in an analogous way to the Mindlin-Herrmann rod theory.

4.2. Flexural Wave Propagation

Flexural behavior of beams can be expressed in terms of propagating and evanescent wave components. Near field waves are generally ignored since their amplitudes decrease rapidly with respect to distance [26]. However, they could generate transmitted and reflected waves of both propagating and evanescent types.

In this section, waveguide equations for flexural vibrations of a beam element is presented both for the Bernoulli-Euler and Timoshenko beam theories. In the high frequency range, adopting Bernoulli-Euler beam theory cause erroneous results. Thus, adopting Timoshenko beam theory in wave propagation analysis could be more appropriate.

4.2.1. Bernoulli-Euler Beam Theory

Wave solution to governing differential equations in terms of spectral representation is given by the equations 3.39 and 3.40. They can be rewritten in the form of the left and right propagating wave modes, as shown by the following equations:

$$\tilde{v}(x) = v_{R1}e^{-ik_Bx} + v_{R2}e^{-k_Bx} + v_{L1}e^{ik_Bx} + v_{L2}e^{k_Bx} \quad (4.17)$$

$$\tilde{\phi}(x) = -ik_Bv_{R1}e^{-ik_Bx} - k_Bv_{R2}e^{-k_Bx} + ik_Bv_{L1}e^{ik_Bx} + k_Bv_{L2}e^{k_Bx} \quad (4.18)$$

Using the force displacement relationship, internal forces developed in the section are calculated as,

$$\tilde{V}(x) = EI(-ik_B^3v_{R1}e^{-ik_Bx} + k_B^3v_{R2}e^{-k_Bx} + ik_B^3v_{L1}e^{ik_Bx} - k_B^3v_{L2}e^{k_Bx}) \quad (4.19)$$

$$\tilde{M}(x) = EI(-k_B^2v_{R1}e^{-ik_Bx} + k_B^2v_{R2}e^{-k_Bx} - k_B^2v_{L1}e^{ik_Bx} + k_B^2v_{L2}e^{k_Bx}) \quad (4.20)$$

Waveguide equations for the flexural wave modes for the Bernoulli-Euler beam theory are represented by the following equations:

$$\begin{Bmatrix} \tilde{v}(x) \\ \tilde{\phi}(x) \\ \tilde{V}(x) \\ \tilde{M}(x) \end{Bmatrix} = \begin{bmatrix} 1 & 1 & 1 & 1 \\ -ik_B & -k_B & ik_B & k_B \\ -EIik_B^3 & EI k_B^3 & EIik_B^3 & -EI k_B^3 \\ -EI k_B^2 & EI k_B^2 & -EI k_B^2 & EI k_B^2 \end{bmatrix} \begin{Bmatrix} v_{R1} \\ v_{R2} \\ v_{L1} \\ v_{L2} \end{Bmatrix} \quad (4.21)$$

4.2.2. Timoshenko Beam Theory

Spectral representation of the solution to the governing differential equations for the Timoshenko beam theory is given by the equations 3.45 and 3.46. In terms of right

and left propagating waves, the equations become:

$$\tilde{v}(x) = R_1 v_{R1} e^{-ik_{B1}x} + R_2 v_{R2} e^{-ik_{B2}x} - R_1 v_{L1} e^{ik_{B1}x} - R_2 v_{L2} e^{ik_{B2}x} \quad (4.22)$$

$$\tilde{\phi}(x) = v_{R1} e^{-ik_{B1}x} + v_{R2} e^{-ik_{B2}x} + v_{L1} e^{ik_{B1}x} + v_{L2} e^{ik_{B2}x} \quad (4.23)$$

Waveguide equations for the flexural wave modes for the Timoshenko beam theory are represented by the following equations:

$$\begin{pmatrix} \tilde{v}(x) \\ \tilde{\phi}(x) \\ \tilde{V}(x) \\ \tilde{M}(x) \end{pmatrix} = \begin{bmatrix} R_1 & R_2 & -R_1 & -R_2 \\ 1 & 1 & 1 & 1 \\ EI k_{B1}^2 - T_9 & EI k_{B2}^2 - T_9 & EI k_{B1}^2 - T_9 & EI k_{B2}^2 - T_9 \\ -EI i k_{B1} & -EI i k_{B2} & EI i k_{B1} & EI i k_{B2} \end{bmatrix} \begin{pmatrix} v_{R1} \\ v_{R2} \\ v_{L1} \\ v_{L2} \end{pmatrix} \quad (4.24)$$

where,

$$T_9 = \rho I K_2 \omega^2 \quad (4.25)$$

4.3. Evaluation of Scattering and Generation Matrices

In order to evaluate dynamic response, the propagation properties of the waves through the waveguides, and the reflection and transmission properties at a joint should be defined. Scattering matrices cover the reflection and transmission properties at the discontinuity. After defining waveguide equation of the wave mode in the local coordinate system, they should be converted into global coordinate system using the rotation matrix as it is done in SEM.

The reflection and transmission coefficients at a joint are calculated based on the equilibrium, compatibility and the prescribed boundary conditions. For n number of elements that are connected to the same joint, $(n - 1)$ compatibility conditions can be written for each degrees of freedom (DOFs). Thus, compatibility conditions

give $(n - 1) * m$ equations for m number of DOFs prescribed at each member end. Equilibrium conditions give m equations. Figure 4.2 illustrates the resultants at the member ends. In the figure, L and R represent the left and right ends of the beam, which are selected arbitrarily, θ is the angle between the local coordinates system of the member and the global coordinate systems, and subscripts 1, 2 and 3 stand for the element indices.

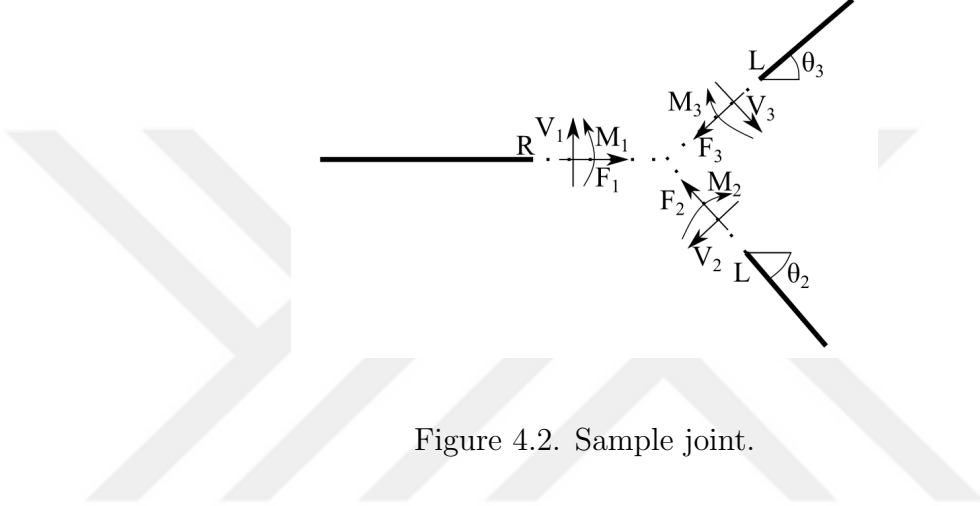


Figure 4.2. Sample joint.

Transmission and reflection coefficients at a joint, which form the junction scattering matrix, are calculated based on the amplitudes of the incoming and outgoing waves. Left propagating waves become incoming waves for a member that is connected to the joint at its left end. The outgoing waves are the waves travelling in the opposite direction. Considering the positive sign convention, resultant forces at the left end are assumed to be negative. The waveguide equations in global coordinates, based on the incoming (u_i) and outgoing (u_o) waves can be rewritten as:

$$\begin{Bmatrix} \mathbf{U} \\ \mathbf{F} \end{Bmatrix} = \begin{bmatrix} \mathbf{d}_i & \mathbf{d}_o \\ \mathbf{f}_i & \mathbf{f}_o \end{bmatrix} \begin{Bmatrix} \mathbf{u}_i \\ \mathbf{u}_o \end{Bmatrix} = \begin{bmatrix} \mathbf{T}\mathbf{Y}_{uL} & \mathbf{T}\mathbf{Y}_{uR} \\ -\mathbf{T}\mathbf{Y}_{fL} & -\mathbf{T}\mathbf{Y}_{fR} \end{bmatrix} \begin{Bmatrix} \mathbf{u}_L \\ \mathbf{u}_R \end{Bmatrix} \quad (4.26)$$

For the members connected to the joint at its right end, the wave guide equations in global coordinates, based on the incoming and outgoing waves are:

$$\begin{Bmatrix} \mathbf{U} \\ \mathbf{F} \end{Bmatrix} = \begin{bmatrix} \mathbf{d}_i & \mathbf{d}_o \\ \mathbf{f}_i & \mathbf{f}_o \end{bmatrix} \begin{Bmatrix} \mathbf{u}_i \\ \mathbf{u}_o \end{Bmatrix} = \begin{bmatrix} \mathbf{T}\mathbf{Y}_{uR} & \mathbf{T}\mathbf{Y}_{uL} \\ \mathbf{T}\mathbf{Y}_{fR} & \mathbf{T}\mathbf{Y}_{fL} \end{bmatrix} \begin{Bmatrix} \mathbf{u}_R \\ \mathbf{u}_L \end{Bmatrix} \quad (4.27)$$

In equations 4.26 and 4.27, \mathbf{T} is the rotation matrix, which converts the displacements and forces from local to global coordinates. \mathbf{U} and \mathbf{F} are the displacement and force vectors, respectively.

Scattering matrix is obtained by substituting displacements and forces generated by the incoming and outgoing wave modes into the equilibrium and compatibility equations, and boundary conditions. System of equations for the joint given in Figure 4.2 is obtained as follows,

$$\begin{Bmatrix} \alpha \mathbf{f}_{\mathbf{o}_1} + \beta \mathbf{d}_{\mathbf{o}_1} & \alpha \mathbf{f}_{\mathbf{o}_2} & \alpha \mathbf{f}_{\mathbf{o}_3} \\ \mathbf{d}_{\mathbf{o}_1} & -\mathbf{d}_{\mathbf{o}_2} & \mathbf{0} \\ \mathbf{d}_{\mathbf{o}_1} & \mathbf{0} & -\mathbf{d}_{\mathbf{o}_3} \end{Bmatrix} \{\mathbf{u}_{\mathbf{o}}\} = \begin{Bmatrix} -\alpha \mathbf{f}_{\mathbf{i}_1} - \beta \mathbf{d}_{\mathbf{i}_1} & -\alpha \mathbf{f}_{\mathbf{i}_2} & -\alpha \mathbf{f}_{\mathbf{i}_3} \\ -\mathbf{d}_{\mathbf{i}_1} & \mathbf{d}_{\mathbf{i}_2} & \mathbf{0} \\ -\mathbf{d}_{\mathbf{i}_1} & \mathbf{0} & \mathbf{d}_{\mathbf{i}_3} \end{Bmatrix} \{\mathbf{u}_{\mathbf{i}}\} + \{\beta \delta + \mathbf{Q}\} \quad (4.28)$$

where, δ and \mathbf{Q} are the prescribed displacement and force vectors at the joint, respectively. Equilibrium and boundary conditions are substituted into the system of equations via α and β matrices, which are square matrices with size equal to number of DOFs. The values are assigned to α and β matrices in accordance with the support and displacement boundary conditions. The detailed information on these matrices can be found in Beale and Accorsi [38]. Then, the scattering matrix, \mathbf{S} , is obtained as:

$$\mathbf{S} = \begin{bmatrix} \alpha \mathbf{f}_{\mathbf{o}_1} + \beta \mathbf{d}_{\mathbf{o}_1} & \alpha \mathbf{f}_{\mathbf{o}_2} & \alpha \mathbf{f}_{\mathbf{o}_3} \\ \mathbf{d}_{\mathbf{o}_1} & -\mathbf{d}_{\mathbf{o}_2} & \mathbf{0} \\ \mathbf{d}_{\mathbf{o}_1} & \mathbf{0} & -\mathbf{d}_{\mathbf{o}_3} \end{bmatrix}^{-1} \begin{bmatrix} -\alpha \mathbf{f}_{\mathbf{i}_1} - \beta \mathbf{d}_{\mathbf{i}_1} & -\alpha \mathbf{f}_{\mathbf{i}_2} & -\alpha \mathbf{f}_{\mathbf{i}_3} \\ -\mathbf{d}_{\mathbf{i}_1} & \mathbf{d}_{\mathbf{i}_2} & \mathbf{0} \\ -\mathbf{d}_{\mathbf{i}_1} & \mathbf{0} & \mathbf{d}_{\mathbf{i}_3} \end{bmatrix} \quad (4.29)$$

The amplitudes of the waves generated by the applied external excitation is calculated using the generation matrix, \mathbf{G} , which is given as:

$$\mathbf{G} = \begin{bmatrix} \alpha \mathbf{f}_{\mathbf{o}_1} + \beta \mathbf{d}_{\mathbf{o}_1} & \alpha \mathbf{f}_{\mathbf{o}_2} & \alpha \mathbf{f}_{\mathbf{o}_3} \\ \mathbf{d}_{\mathbf{o}_1} & -\mathbf{d}_{\mathbf{o}_2} & \mathbf{0} \\ \mathbf{d}_{\mathbf{o}_1} & \mathbf{0} & -\mathbf{d}_{\mathbf{o}_3} \end{bmatrix}^{-1} \quad (4.30)$$

4.4. Assemblage of Waveguides

In order to obtain dynamic response of the whole structure to a given excitation, scattering and generation matrices obtained at each joint are assembled to form the structural system. Then, the scattering and generation matrices of a structure that comprises N number of elements are derived as:

$$\mathbf{S} = \begin{bmatrix} \mathbf{S}_1 & & & \\ & \mathbf{S}_2 & & \\ & & \ddots & \\ & & & \mathbf{S}_N \end{bmatrix} \quad (4.31)$$

$$\mathbf{G} = \begin{bmatrix} \mathbf{G}_1 & & & \\ & \mathbf{G}_2 & & \\ & & \ddots & \\ & & & \mathbf{G}_N \end{bmatrix} \quad (4.32)$$

The amplitudes of the generated waves at adjacent joints are calculated through system transmission matrices, which are diagonal matrices. The exponential part of the waveguide equations, which correspond to the waves travel in the direction of increasing spatial coordinate with respect to member's corresponding local coordinate system, is substituted into the diagonal of the system transmission matrix (\mathbf{ST}). To assign the amplitude of the wave at a joint caused by the wave generated at an adjacent joint, a permutation matrix (\mathbf{P}) is defined. For instance, the outgoing wave u_{o1_1} at joint 1 in Figure 4.3 becomes incoming wave u_{i2_1} at joint 2. The amplitude of the incoming waves can be related to the outgoing waves by means of the system transmission and permutation matrices.

(\mathbf{ST}) and (\mathbf{P}) matrices based on elementary rod and Bernoulli-Euler beam the-

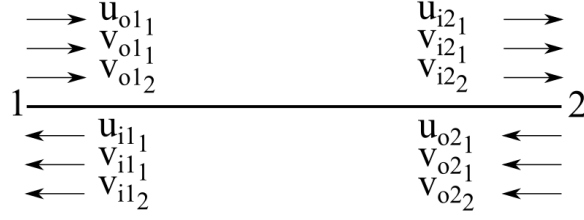


Figure 4.3. Travelling waves through an element.

ories can be defined as:

$$\begin{Bmatrix} u_{i1_1} \\ v_{i1_1} \\ v_{i1_2} \\ u_{i2_1} \\ v_{i2_1} \\ v_{i2_2} \end{Bmatrix} = [\mathbf{ST}] [\mathbf{P}] \begin{Bmatrix} u_{o1_1} \\ v_{o1_1} \\ v_{o1_2} \\ u_{o2_1} \\ v_{o2_1} \\ v_{o2_2} \end{Bmatrix} \quad (4.33)$$

where,

$$[\mathbf{ST}] = \begin{bmatrix} e^{-ik_R x} & & & & & & \\ & e^{-ik_B x} & & & & & \\ & & e^{-k_B x} & & & & \\ & & & e^{-ik_R x} & & & \\ & & & & e^{-ik_B x} & & \\ & & & & & e^{-k_B x} & \end{bmatrix}; \quad [\mathbf{P}] = \begin{bmatrix} 0 & 0 & 0 & 1 & 0 & 0 \\ 0 & 0 & 0 & 0 & 1 & 0 \\ 0 & 0 & 0 & 0 & 0 & 1 \\ 1 & 0 & 0 & 0 & 0 & 0 \\ 0 & 1 & 0 & 0 & 0 & 0 \\ 0 & 0 & 1 & 0 & 0 & 0 \end{bmatrix}$$

For a structure that comprises N number of elements, the incoming and outgoing waves are related to each other as:

$$\begin{Bmatrix} \mathbf{U}_{i1} \\ \mathbf{U}_{i2} \\ \vdots \\ \mathbf{U}_{iN} \end{Bmatrix} = \begin{bmatrix} \mathbf{ST}_1 \mathbf{P}_1 & & & \\ & \mathbf{ST}_2 \mathbf{P}_2 & & \\ & & \ddots & \\ & & & \mathbf{ST}_N \mathbf{P}_N \end{bmatrix} \begin{Bmatrix} \mathbf{U}_{o1} \\ \mathbf{U}_{o2} \\ \vdots \\ \mathbf{U}_{oN} \end{Bmatrix} \quad (4.34)$$

Amplitude of the outgoing waves is calculated as:

$$\{\mathbf{U}_o\} = [\mathbf{I} - \mathbf{S} * \mathbf{S}\mathbf{T} * \mathbf{P}]^{-1} [\mathbf{G}] \{\beta\delta + \mathbf{Q}\} \quad (4.35)$$

where, (\mathbf{I}) is the identity matrix.

The displacements and forces acting at the joint and/or at an arbitrary location through the member length is calculated by substituting the incoming and outgoing wave amplitudes into the wave solution of the governing differential equation.

4.5. Numerical Example

As an example, the dynamic response of a five-story, two-bay plane frame, which is given in Section 3.4, is calculated by using both FEM and TWM. It is aimed to demonstrate the accuracy of TWM in the medium to high frequency range. Since, it is known that the accuracy of FEM analysis increases with the decreasing mesh size, two different FEM models are used in the analysis. In the first FEM model, structural elements without any kind of discontinuity are modeled as a single element. In the second FEM model, each structural member is divided into 100 segments. Moreover, two TWM models are constructed in order to see the effect of adopting higher order theories on the calculated dynamic response. In the first TWM model, structural elements are formulated based on elementary theories. In the second TWM model, higher order theories, namely Love rod and Timoshenko beam theories, are adopted. Mindlin-Herrmann and Three-Mode rod theories are not employed in the analyses, because they introduce extra DOFs and the frequency range of interest does not cover the cut-off frequency. A MATLAB-based code [22] is prepared for the TWM analysis. SAP2000 v.19 [23] is utilized for the FEM analysis. The dynamic response is calculated under the effect of the self-weight of the structure and the applied base excitation.

The same base excitation, which is defined in the Section 3.4 is applied in the longitudinal direction.

The Fourier Amplitude Spectra (FAS) of the dynamic response at DOF= 52, which corresponds to the top displacement in the direction of excitation, is presented in Figure 4.4. The figure shows FAS of the response calculated by using the first and the second FEM models, and the first and the second TWM models in the frequency range of 0-50 Hz. In the low frequency range, the responses calculated from the four analyses are almost identical. However, as the frequency increases, the calculated responses start diverging.

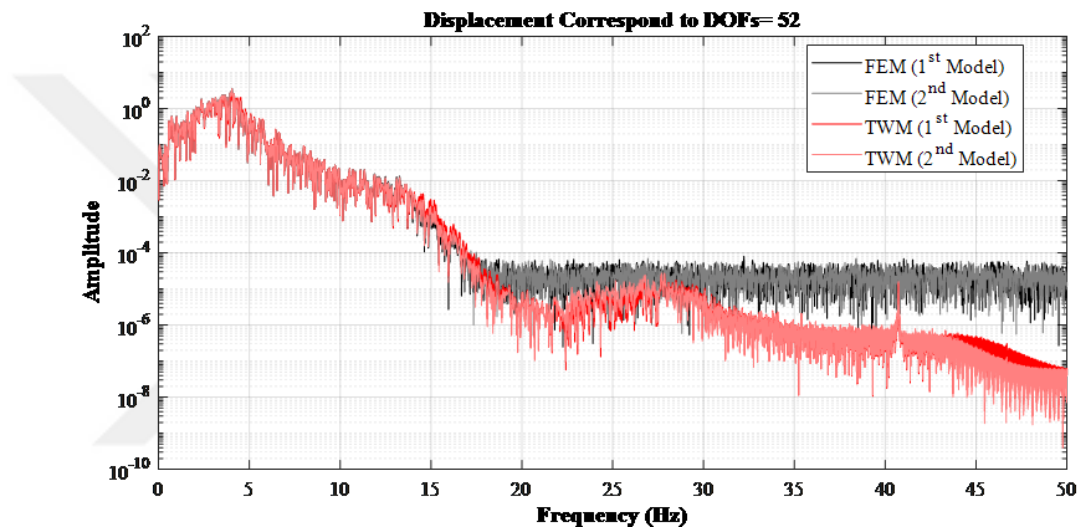


Figure 4.4. FAS of the response at DOF= 52 between 0-50 Hz.

For a better understanding, the dynamic response calculated from the four analyses between the frequency ranges of 0-10 Hz., 10-15 Hz. and 15-20 Hz. are illustrated in Figure 4.5, Figure 4.6 and Figure 4.7, respectively. In the low frequency range, which is presented in Figure 4.4, the dynamic response calculated at DOF= 52 from the four analyses are approximately identical. As can be seen from Figure 4.6, in the vicinity of 12 Hz. the response calculated from the first FEM analysis starts diverging from the others. As the frequency increases the response obtained from the second TWM model is also diverges from the response obtained from the second FEM and the first TWM. In the vicinity of 16 Hz. the dynamic response at DOF= 52 calculated from the first TWM deviate from the second FEM. Beyond 18 Hz., the responses calculated from the TWM and FEM models differ significantly.

The time-domain response can be calculated by taking the inverse Fourier trans-

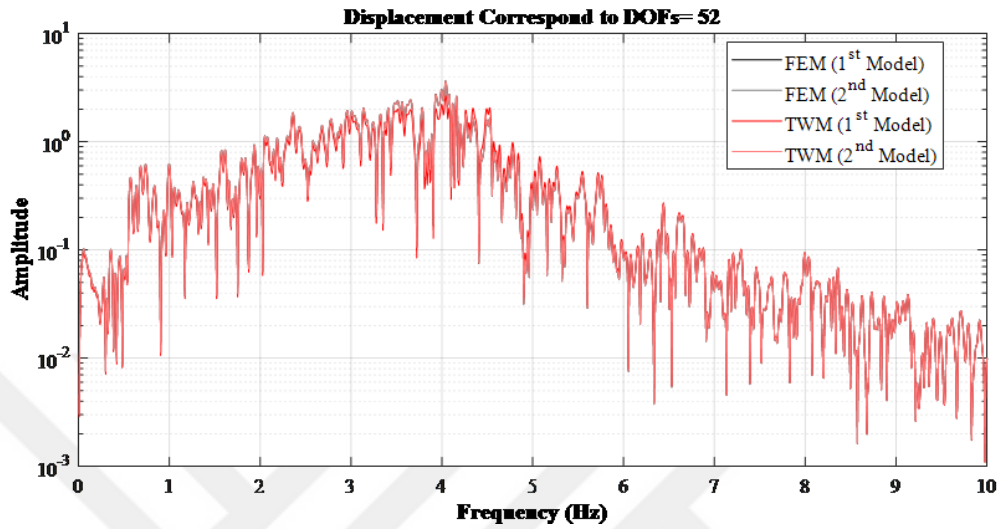


Figure 4.5. FAS of the response at DOF= 52 between 0-10 Hz.

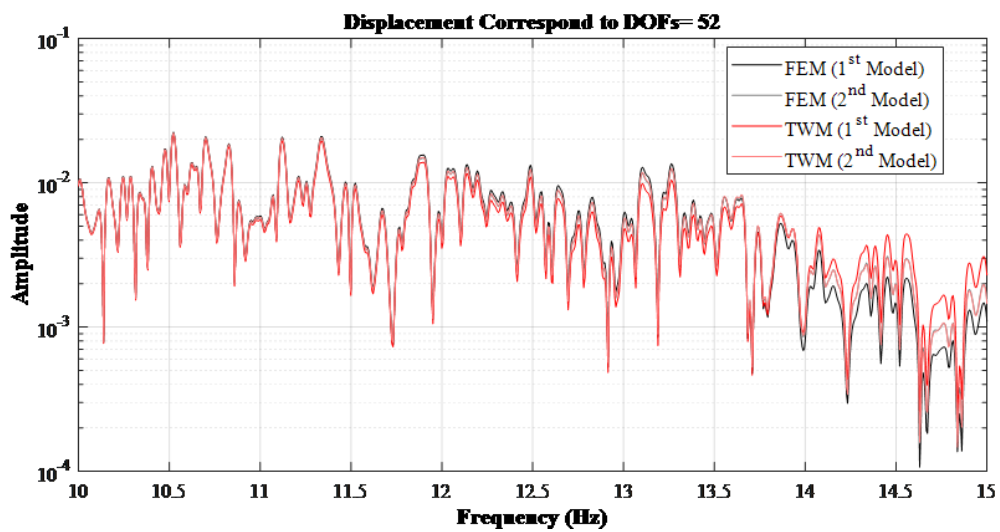


Figure 4.6. FAS of the response at DOF= 52 between 10-15 Hz.

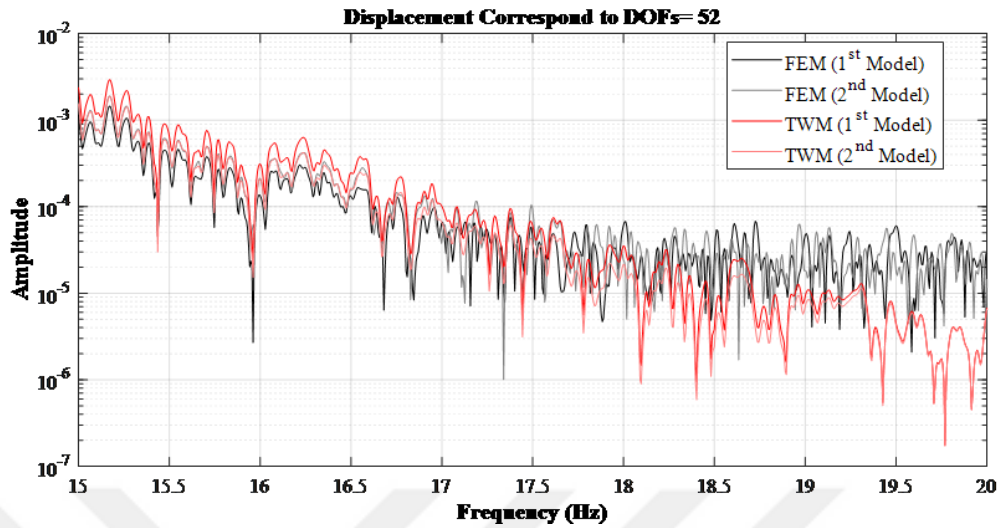


Figure 4.7. FAS of the response at DOF= 52 between 15-20 Hz.

form of the response calculated in the frequency domain. Figure 4.8 and Figure 4.9 illustrate the comparison of the calculated time domain response obtained from the four analyses. In Figure 4.8 and Figure 4.9, the response is band-pass filtered between 0.1-5 Hz. and 15-20 Hz, respectively. It is aimed to reflect the differences in the low and high frequency ranges. The response in the low frequency range is identical for four of the analysis. However, as the frequency increases they differ considerably.

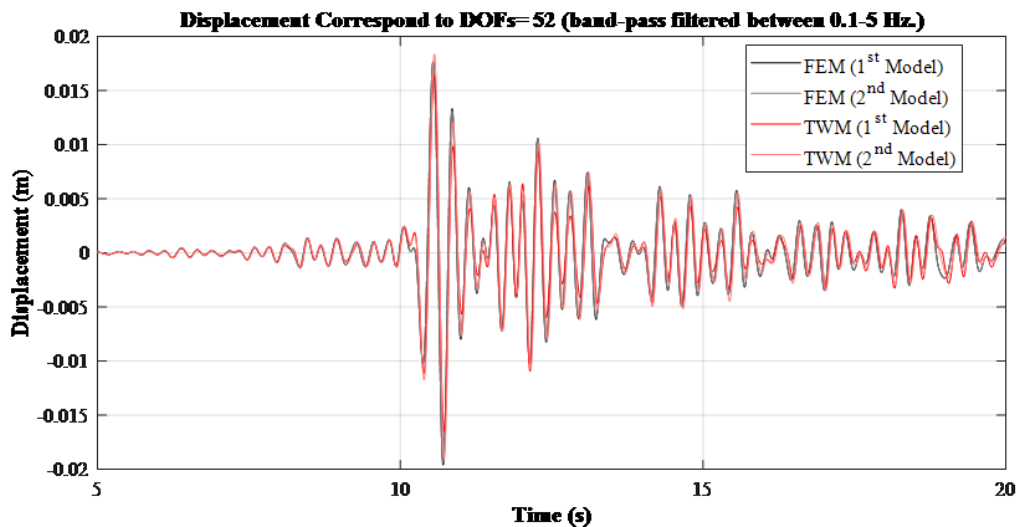


Figure 4.8. Band pass filtered between 0.1-5 Hz. time domain response at DOF= 52 between 5-20 sec.

Resultant forces can also be calculated both in the frequency and time domains

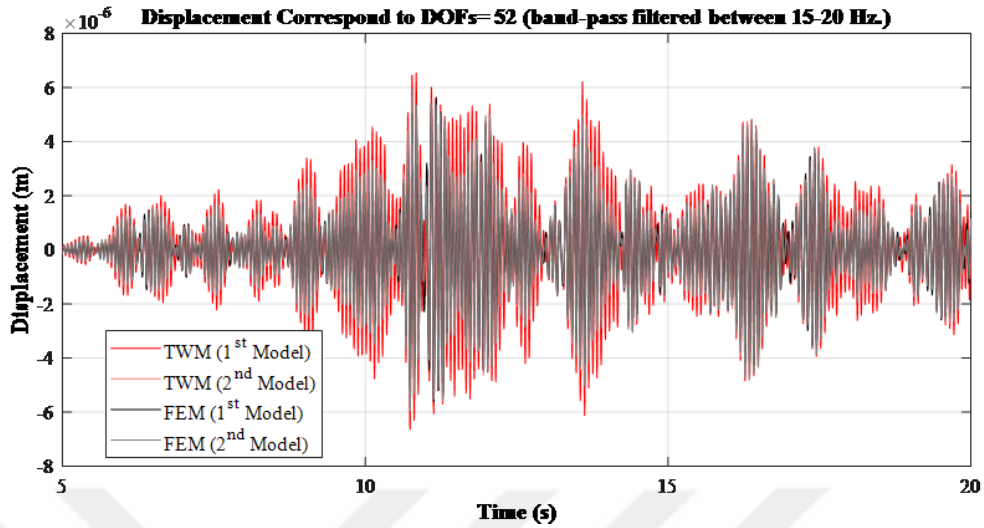


Figure 4.9. Band pass filtered between 15-20 Hz. time domain response at DOF= 52 between 5-20 sec.

using TWM. Figure 4.10, Figure 4.11 and Figure 4.12 show the variation in the base shear with respect to time between 8-17 s., 17-26 s. and 26-35 s., respectively. The base shear calculated from the four models differ from each other throughout the time interval.

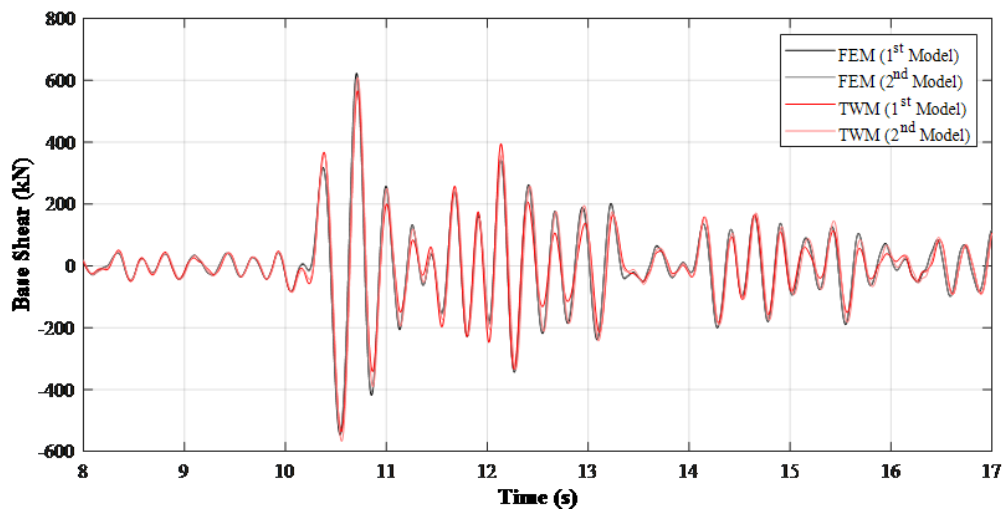


Figure 4.10. Variation in base shear with respect to time (between 8-17 sec.).

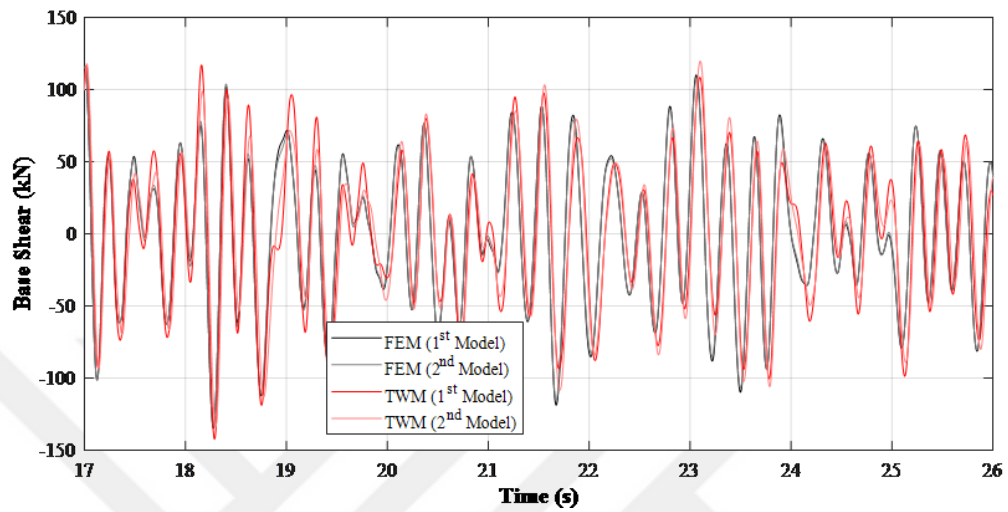


Figure 4.11. Variation in base shear with respect to time (between 17-26 sec.).

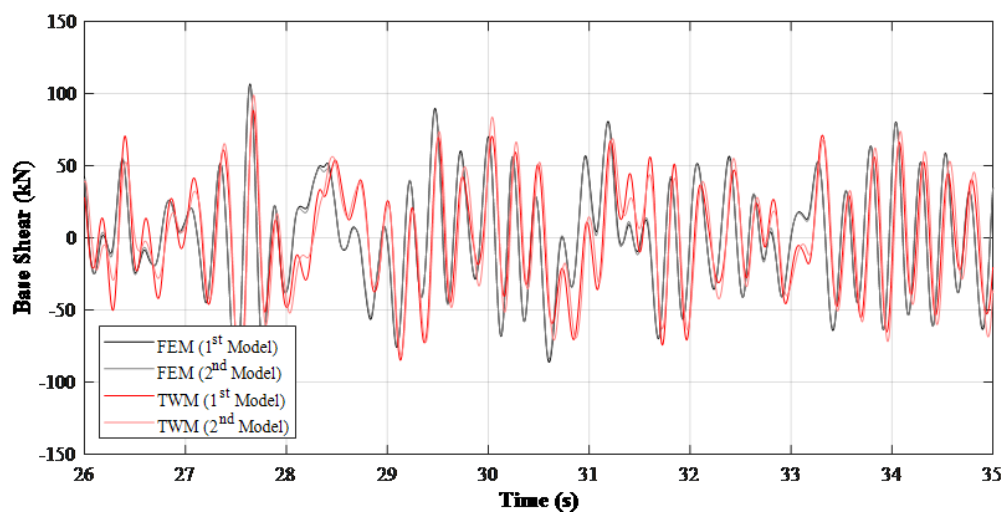


Figure 4.12. Variation in base shear with respect to time (between 26-35 sec.).

5. ENERGY FLUX

Seismic design and assessment of the structures are most commonly carried out using Finite Element Method (FEM). However, FEM becomes insufficient in the mid to high frequency range. Thus, energy-based methods can be utilized as an alternative methodology to perform dynamic analysis of structures. Housner [39] was the first who introduced energy-based approach in seismic analysis of structures. The energy input to a structure is a stable parameter since it mainly depends on the mass and the natural period of the structure, and scarcely effected by the strength and the type of restoring force characteristics [40].

Statistical Energy Analysis (SEA) have emerged as a robust methodology to carry out dynamic analysis of structures, especially in the high frequency range. In SEA, a complex structure is modeled as a statistical set of subsystems or mode groups [41]. It only provides information about the average dynamic response of the system. The spatial distribution of the dynamic response is lost. According to Carcaterra and Sestieri [42], statistical energy analysis produces poor output against significant qualitative and quantitative input data. Moreover, it is only valid for broadband excitations. As an alternative methodology, Wave Intensity Analysis (WIA) is proposed by Langley (1992). Energy Finite Element Analysis (EFEA) was introduced by Nefske and Sung (1987). According to their methodology, mechanical energy flow through an element can be assumed as a heat conduction problem. Wohlever and Bernhard [43] and Carcaterra and Sestieri [42] have proved that, the heat conduction analogy is not valid for the general case of energy flow in structures. Lase, Ichchou and Jezequel [44], proposed two methods, namely general energy and simplified energy methods, to obtain the behavior of energy in beams and bars. General energy method corresponds to the total energy density and the active energy flow. Simplified energy method complies with the Lagrangian energy density and reactive energy flow. Ichchou, Le Bot and Jezequel [45] proposed energy models for one-dimensional multi propagative systems. Mace and Shorter [46] suggested a new methodology, which splits the model into global and local subsystems. Both are treated by classical finite element methods. Park and

Hong [47] derived vibrational energy flow in Timoshenko beams in terms of space and time averaged energy of far field waves. According to Carcaterra and Sestieri [42], the kinetic energy seems to be more convenient, because this is the quantity that is more relevant in dynamic problems and more related to acoustic radiation.

Energy flux is a dynamic measure of energy for base excitations, which is defined as the kinetic energy due to seismic shaking multiplied by the propagation velocity of seismic waves. It gives the amount of seismic energy transmitted per unit time through a cross-section of a medium [3]. In this manner, characteristics of energy flow and dissipation throughout the structure with respect to frequency can be obtained. Thus, this method provides a new tool to evaluate dynamic response of structures. Energy flux propagates as the waves travel through the waveguides. As in the wave propagation formulation, at the discontinuities, some portion of the incident energy transmitted into the adjacent members and some part is reflected. The reflection and transmission coefficients for the energy flux are independent of the direction of the propagation. The sum of the reflected and transmitted energy flux is equal to the incident energy flux due to the principle of conservation of energy.

5.1. Transmission and Reflection Coefficients

Transmission and reflection coefficients for energy flux are equal to the ratio of transmitted and reflected energy flux, respectively, to the incident energy flux. These coefficients are derived based on the transmission and the reflection coefficients of the waves, and characteristic impedances of waveguides. Thus, the scattering matrix at a joint is derived as the first step in the calculation of transmission and reflection coefficients of the energy flux. The scattering matrix is constructed based on the methodology presented by Beale and Accorsi [38]. The scattering matrix for n number

of elements that are connected to same joint are derived as:

$$\mathbf{S} = \begin{bmatrix} \mathbf{r}_{11} & \mathbf{t}_{21} & \cdots & \mathbf{t}_{n1} \\ \mathbf{t}_{12} & \mathbf{r}_{22} & \cdots & \mathbf{t}_{n2} \\ \vdots & \vdots & \ddots & \vdots \\ \mathbf{t}_{1n} & \mathbf{t}_{2n} & \cdots & \mathbf{r}_{nn} \end{bmatrix} \quad (5.1)$$

Where, \mathbf{t} and \mathbf{r} represent the transmission and reflection matrices, respectively. The subscript shows the direction of the wave. The size of the reflection and transmission matrices depends on the number of wave modes that travel through the member. For a better understanding, the scattering matrix at the joint where the wave experience material and/or cross-section change, is obtained based on elementary rod theory. The properties of the rods and the wave modes are presented in Figure 5.1.

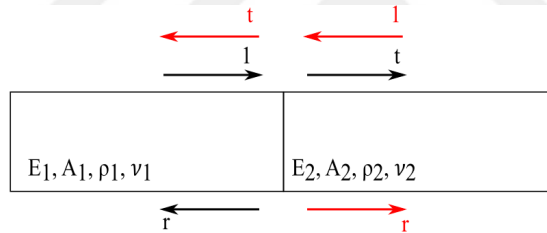


Figure 5.1. Energy flux between collinear rods.

In Figure 5.1, E , A , ρ and ν stand for the Young's modulus, area of the section, mass density of unit volume and Poisson's ratio, respectively. Subscripts 1 and 2 are the element numbers and l , t and r are the incident, transmitted and reflected waves. Scattering matrix is obtained as:

$$\mathbf{S} = \begin{bmatrix} \mathbf{r}_{11} & \mathbf{t}_{21} \\ \mathbf{t}_{12} & \mathbf{r}_{22} \end{bmatrix} = \begin{bmatrix} \frac{E_1 A_1 k_{R1} - E_2 A_2 k_{R2}}{E_1 A_1 k_{R1} + E_2 A_2 k_{R2}} & \frac{2E_2 A_2 k_{R2}}{E_1 A_1 k_{R1} + E_2 A_2 k_{R2}} \\ \frac{2E_1 A_1 k_{R1}}{E_1 A_1 k_{R1} + E_2 A_2 k_{R2}} & \frac{-(E_1 A_1 k_{R1} - E_2 A_2 k_{R2})}{E_1 A_1 k_{R1} + E_2 A_2 k_{R2}} \end{bmatrix} \quad (5.2)$$

In Eq. 5.2, \mathbf{r}_{11} and \mathbf{r}_{22} stands for the reflected wave coefficients for the first and second elements, respectively. \mathbf{t}_{12} is the coefficient of the wave transmitted from the first to the second element. Conversely, \mathbf{t}_{21} is the coefficient of the wave transmitted from the second to the first element. k_{R1} and k_{R2} correspond to the wavenumber related to the first and second elements respectively. Group velocity of the waves based on

Elementary rod theory is given in Eq. 3.31.

The reflection and transmission coefficients for energy flux is derived as:

$$\mathbf{S}_{\mathbf{EF}} = \begin{bmatrix} \mathbf{r}_{\mathbf{EF11}} & \mathbf{t}_{\mathbf{EF21}} \\ \mathbf{t}_{\mathbf{EF12}} & \mathbf{r}_{\mathbf{EF22}} \end{bmatrix} \quad (5.3)$$

$$= \begin{bmatrix} \left(\frac{E_1 A_1 k_{R1} - E_2 A_2 k_{R2}}{E_1 A_1 k_{R1} + E_2 A_2 k_{R2}} \right)^2 & \frac{\rho_1 A_1 c_{gR1}}{\rho_2 A_2 c_{gR2}} \left(\frac{2E_2 A_2 k_{R2}}{E_1 A_1 k_{R1} + E_2 A_2 k_{R2}} \right)^2 \\ \frac{\rho_2 A_2 c_{gR2}}{\rho_1 A_1 c_{gR1}} \left(\frac{2E_1 A_1 k_{R1}}{E_1 A_1 k_{R1} + E_2 A_2 k_{R2}} \right)^2 & \left(\frac{-(E_1 A_1 k_{R1} - E_2 A_2 k_{R2})}{E_1 A_1 k_{R1} + E_2 A_2 k_{R2}} \right)^2 \end{bmatrix}$$

In Eq. 5.3, $\mathbf{r}_{\mathbf{EF11}}$ and $\mathbf{r}_{\mathbf{EF22}}$ stands for the reflected energy flux coefficients for the first and second elements, respectively. $\mathbf{t}_{\mathbf{EF12}}$ is the coefficient of the energy flux transmitted from the first to the second element. Conversely, $\mathbf{t}_{\mathbf{EF21}}$ is the coefficient of the energy flux transmitted from the second to the first element. c_{gR1} and c_{gR2} correspond to the group velocities related to the first and second elements, respectively.

The reflection and transmission coefficients based on the Bernoulli-Euler beam theory for both wave propagation and energy flux are calculated for the beams are shown in Figure 5.2.

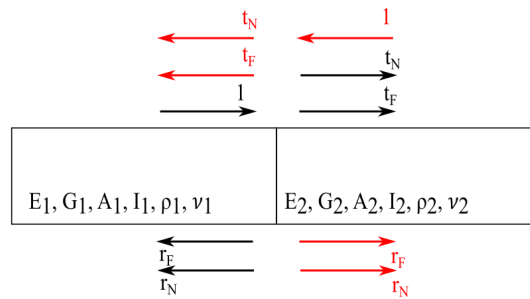


Figure 5.2. Energy flux between collinear beams.

In Figure 5.2, E, G, A, I, ρ and ν stand for the Young's modulus, shear modulus, area of the section, second moment of inertia, mass density per unit volume and Poisson's ratio, respectively. Subscripts 1 and 2 are the element numbers and 1, t_F , t_N , r_F and r_N are the incident, transmitted far field, transmitted near field, reflected far field and reflected near field waves.

Flexural behavior of a beam can be expressed in terms of propagating and evanescent waves. Evanescent waves are generally ignored, since the amplitudes decrease rapidly. However, they can generate significant transmitted and reflected waves of both propagating and evanescent types [26]. The scattering matrix is obtained as follows:

$$\mathbf{S} = \begin{bmatrix} \mathbf{r}_{11} & \mathbf{t}_{21} \\ \mathbf{t}_{12} & \mathbf{r}_{22} \end{bmatrix} = \begin{bmatrix} \begin{bmatrix} r_{1111} & r_{1112} \\ r_{1121} & r_{1122} \end{bmatrix} & \begin{bmatrix} t_{2111} & t_{2112} \\ t_{2121} & t_{2122} \end{bmatrix} \\ \begin{bmatrix} t_{1211} & t_{1212} \\ t_{1221} & t_{1222} \end{bmatrix} & \begin{bmatrix} r_{2211} & r_{2212} \\ r_{2221} & r_{2222} \end{bmatrix} \end{bmatrix} \quad (5.4)$$

In Eq. 5.4, the size of the transmission and reflection matrices are two, since two wave modes, namely far-field and near-field wave modes, characterize the behavior of the beam. The off-diagonal terms in reflection and transmission matrices represent the ratio of the transformed waves from evanescent to propagating and propagating to evanescent. The explicit form of the reflection and transmission matrices are presented in Eqs. 5.5 to 5.8.

$$\mathbf{r}_{11} = \begin{bmatrix} -\frac{-2\beta_1 + i\chi_1 - 2i\beta_1\chi_1 + i\beta_1^2\chi_1 + 2\beta_1\chi_1^2}{2\beta_1 + \chi_1 + 2\beta_1\chi_1 + \beta_1^2\chi_1 + 2\beta_1\chi_1^2} & -\frac{(-1-i+(1+i)\beta_1^2)\chi_1}{2\beta_1 + \chi_1 + 2\beta_1\chi_1 + \beta_1^2\chi_1 + 2\beta_1\chi_1^2} \\ -\frac{(-1+i+(1-i)\beta_1^2)\chi_1}{2\beta_1 + \chi_1 + 2\beta_1\chi_1 + \beta_1^2\chi_1 + 2\beta_1\chi_1^2} & \frac{2\beta_1 + i\chi_1 - 2i\beta_1\chi_1 + i\beta_1^2\chi_1 - 2\beta_1\chi_1^2}{2\beta_1 + \chi_1 + 2\beta_1\chi_1 + \beta_1^2\chi_1 + 2\beta_1\chi_1^2} \end{bmatrix} \quad (5.5)$$

$$\mathbf{t}_{12} = \begin{bmatrix} \frac{2(1+\beta_1)(1+\chi_1)}{2\beta_1 + \chi_1 + 2\beta_1\chi_1 + \beta_1^2\chi_1 + 2\beta_1\chi_1^2} & -\frac{2i(-1+\beta_1)(i+\chi_1)}{2\beta_1 + \chi_1 + 2\beta_1\chi_1 + \beta_1^2\chi_1 + 2\beta_1\chi_1^2} \\ \frac{2(-1+\beta_1)(1+i\chi_1)}{2\beta_1 + \chi_1 + 2\beta_1\chi_1 + \beta_1^2\chi_1 + 2\beta_1\chi_1^2} & \frac{2(1+\beta_1)(1+\chi_1)}{2\beta_1 + \chi_1 + 2\beta_1\chi_1 + \beta_1^2\chi_1 + 2\beta_1\chi_1^2} \end{bmatrix} \quad (5.6)$$

$$\mathbf{t}_{21} = \begin{bmatrix} \frac{2(1+\beta_2)(1+\chi_2)}{2\beta_2 + \chi_2 + 2\beta_2\chi_2 + \beta_2^2\chi_2 + 2\beta_2\chi_2^2} & -\frac{2i(-1+\beta_2)(i+\chi_2)}{2\beta_2 + \chi_2 + 2\beta_2\chi_2 + \beta_2^2\chi_2 + 2\beta_2\chi_2^2} \\ \frac{2(-1+\beta_2)(1+i\chi_2)}{2\beta_2 + \chi_2 + 2\beta_2\chi_2 + \beta_2^2\chi_2 + 2\beta_2\chi_2^2} & \frac{2(1+\beta_2)(1+\chi_2)}{2\beta_2 + \chi_2 + 2\beta_2\chi_2 + \beta_2^2\chi_2 + 2\beta_2\chi_2^2} \end{bmatrix} \quad (5.7)$$

$$\mathbf{r}_{22} = \begin{bmatrix} -\frac{-2\beta_2 + i\chi_2 - 2i\beta_2\chi_2 + i\beta_2^2\chi_2 + 2\beta_2\chi_2^2}{2\beta_2 + \chi_2 + 2\beta_2\chi_2 + \beta_2^2\chi_2 + 2\beta_2\chi_2^2} & -\frac{(-1-i+(1+i)\beta_2^2)\chi_2}{2\beta_2 + \chi_2 + 2\beta_2\chi_2 + \beta_2^2\chi_2 + 2\beta_2\chi_2^2} \\ -\frac{(-1+i+(1-i)\beta_2^2)\chi_2}{2\beta_2 + \chi_2 + 2\beta_2\chi_2 + \beta_2^2\chi_2 + 2\beta_2\chi_2^2} & \frac{2\beta_2 + i\chi_2 - 2i\beta_2\chi_2 + i\beta_2^2\chi_2 - 2\beta_2\chi_2^2}{2\beta_2 + \chi_2 + 2\beta_2\chi_2 + \beta_2^2\chi_2 + 2\beta_2\chi_2^2} \end{bmatrix} \quad (5.8)$$

The terms β_1 , β_2 , χ_1 and χ_2 are calculated as:

$$\beta_1 = \frac{E_2 I_2 k_{B2}^2}{E_1 I_1 k_{B1}^2}; \beta_2 = \frac{E_1 I_1 k_{B1}^2}{E_2 I_2 k_{B2}^2}; \chi_1 = \frac{k_{B2}}{k_{B1}}; \chi_2 = \frac{k_{B1}}{k_{B2}} \quad (5.9)$$

k_{B1} and k_{B2} are the wavenumbers of the propagating wave mode of the first and the

second beams, respectively. Wave numbers corresponding to second mode of the beams are equal to ik_{B1} and ik_{B2} . For the undamped case, wavenumber related to the second mode becomes purely imaginary. The group velocity considering only the first mode (c_{gFB}) of the beam is derived as given in Eq. 3.51. The group velocity for the second mode (c_{gFN}) is equal to ic_{gFB} . For the undamped case, it becomes purely imaginary, which means the second mode wave does not propagate.

The reflection and transmission coefficients for energy flux is derived as:

$$\mathbf{S}_{\text{EF}} = \begin{bmatrix} \mathbf{r}_{\text{EF11}} & \mathbf{t}_{\text{EF21}} \\ \mathbf{t}_{\text{EF12}} & \mathbf{r}_{\text{EF22}} \end{bmatrix} = \begin{bmatrix} \begin{bmatrix} r_{EF11_{11}} & r_{EF11_{12}} \\ r_{EF11_{21}} & r_{EF11_{22}} \end{bmatrix} & \begin{bmatrix} t_{EF21_{11}} & t_{EF21_{12}} \\ t_{EF21_{21}} & t_{EF21_{22}} \end{bmatrix} \\ \begin{bmatrix} t_{EF12_{11}} & t_{EF12_{12}} \\ t_{EF12_{21}} & t_{EF12_{22}} \end{bmatrix} & \begin{bmatrix} r_{EF22_{11}} & r_{EF22_{12}} \\ r_{EF22_{21}} & r_{EF22_{22}} \end{bmatrix} \end{bmatrix} \quad (5.10)$$

where,

$$\mathbf{r}_{\text{EF11}} = \begin{bmatrix} r_{EF11_{11}} & r_{EF11_{12}} \\ r_{EF11_{21}} & r_{EF11_{22}} \end{bmatrix} = \begin{bmatrix} |r_{11_{11}}|^2 & \frac{c_{gFB1}}{c_{gNB1}} |r_{11_{12}}|^2 \\ \frac{c_{gNB1}}{c_{gFB1}} |r_{11_{21}}|^2 & |r_{11_{22}}|^2 \end{bmatrix} \quad (5.11)$$

$$\mathbf{t}_{\text{EF12}} = \begin{bmatrix} t_{EF12_{11}} & t_{EF12_{12}} \\ t_{EF12_{21}} & t_{EF12_{22}} \end{bmatrix} = \begin{bmatrix} \frac{\rho_2 A_2 c_{gFB2}}{\rho_1 A_1 c_{gFB1}} |t_{12_{11}}|^2 & \frac{\rho_2 A_2 c_{gFB2}}{\rho_1 A_1 c_{gNB1}} |t_{12_{12}}|^2 \\ \frac{\rho_2 A_2 c_{gNB2}}{\rho_1 A_1 c_{gFB1}} |t_{12_{21}}|^2 & \frac{\rho_2 A_2 c_{gNB2}}{\rho_1 A_1 c_{gNB1}} |t_{12_{22}}|^2 \end{bmatrix} \quad (5.12)$$

$$\mathbf{t}_{\text{EF21}} = \begin{bmatrix} t_{EF21_{11}} & t_{EF21_{12}} \\ t_{EF21_{21}} & t_{EF21_{22}} \end{bmatrix} = \begin{bmatrix} \frac{\rho_1 A_1 c_{gFB1}}{\rho_2 A_2 c_{gFB2}} |t_{21_{11}}|^2 & \frac{\rho_1 A_1 c_{gFB1}}{\rho_2 A_2 c_{gNB2}} |t_{21_{12}}|^2 \\ \frac{\rho_1 A_1 c_{gNB1}}{\rho_2 A_2 c_{gFB2}} |t_{21_{21}}|^2 & \frac{\rho_1 A_1 c_{gNB1}}{\rho_2 A_2 c_{gNB2}} |t_{21_{22}}|^2 \end{bmatrix} \quad (5.13)$$

$$\mathbf{r}_{\text{EF22}} = \begin{bmatrix} r_{EF22_{11}} & r_{EF22_{12}} \\ r_{EF22_{21}} & r_{EF22_{22}} \end{bmatrix} = \begin{bmatrix} |r_{22_{11}}|^2 & \frac{c_{gFB2}}{c_{gNB2}} |r_{22_{12}}|^2 \\ \frac{c_{gNB2}}{c_{gFB2}} |r_{22_{21}}|^2 & |r_{22_{22}}|^2 \end{bmatrix} \quad (5.14)$$

In case of undamped collinear beams, the real part of the off-diagonal terms of the reflection and transmission matrices are equal to zero. When the elements are non-collinear, size of the reflection and transmission matrices become three, which correspond to longitudinal and flexural wave modes. Thus, the reflection and transmission

matrices for energy flux are obtained as:

$$\mathbf{r}_{\mathbf{EF}ij} = \begin{bmatrix} r_{EFij11} & r_{EFij12} & r_{EFij13} \\ r_{EFij21} & r_{EFij22} & r_{EFij23} \\ r_{EFij31} & r_{EFij32} & r_{EFij33} \end{bmatrix} \quad \mathbf{t}_{\mathbf{EF}ij} = \begin{bmatrix} t_{EFij11} & t_{EFij12} & t_{EFij13} \\ t_{EFij21} & t_{EFij22} & t_{EFij23} \\ t_{EFij31} & t_{EFij32} & t_{EFij33} \end{bmatrix} \quad (5.15)$$

where, subscripts i and j corresponds to the direction of the waves, the diagonal terms stands for the reflected or transmitted waves without mode conversion. Subscripts 11, 22 and 33 stand for the longitudinal to longitudinal, far-field flexural to far-field flexural and near-field flexural to near-field flexural waves. The off-diagonal terms indicate the energy flux transmitted and reflected with mode conversion.

In case of undamped structures formed by non-collinear elements, the real part of the off-diagonal terms corresponding to evanescent waves is equal to zero. Thus, the energy flux carried by the evanescent waves becomes equal to zero. However, if some amount of damping is introduced to the structure, the real part of the off-diagonal terms corresponding to evanescent waves becomes different than zero and negative valued. The diagonal terms are purely real for damped or undamped structures formed by the collinear or non-collinear elements.

The energy flux reflection and transmission coefficients for an 'L' type joint shown in Figure 5.3 are plotted in Figure 5.4 through Figure 5.9. In Figure 5.3, 1, t , t_n , t_f , r , r_n and r_f stand for the incident, longitudinal transmitted wave, transmitted far field flexural wave, transmitted flexural near field wave, reflected longitudinal wave, reflected far field flexural wave and reflected nearfield flexural wave. It is assumed that the properties of the sections are identical. The effects of the 90-degree angle at the joint on energy flux reflection and transmission coefficients are investigated.

Figure 5.4 through Figure 5.9 show the absolute value of the real part of the energy flux reflection and transmission coefficients, and their sum (to show that the sum is equal to one). The reflection and transmission coefficients corresponding to the undamped structure are given in Figure 5.4 through 5.6. When damping is introduced

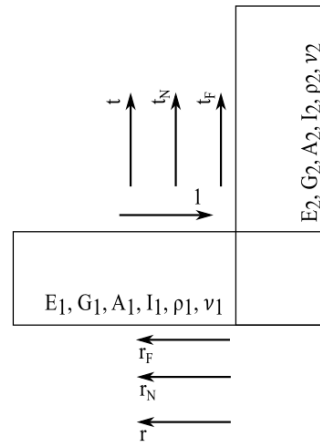


Figure 5.3. Reflected and transmitted waves at an L joint.

to the system by replacing the Young's modulus by a complex value, the off-diagonal terms related to the evanescent waves become different than zero. Figure 5.7 to Figure 5.9 correspond to the damped structure. Sum of the absolute values of the real parts are equal to unity due to the conservation of energy.

Figure 5.4 represents the transmitted and reflected energy flux related to the incident longitudinal wave. The incident energy flux in the longitudinal direction mostly reflected as longitudinal energy flux and its contribution decreases as the frequency increases. The energy flux transmitted into the second element as the far-field energy flux is the other major mechanism, which becomes dominant as the frequency increases. Moreover, some part of the energy flux is reflected as far-field flexural energy flux. Negligibly small amount of energy flux is transmitted to the second element as longitudinal energy flux. The sum of the reflected and transmitted energy fluxes are equal to unity.

In accordance with Figure 5.5, the far-field flexural energy flux incident from the first element is mostly reflected as far-field energy flux, transmitted into the adjacent member as far-field and longitudinal energy fluxes. The portion of the reflected and transmitted energy fluxes depend on the frequency. Small amount of energy flux is reflected as longitudinal wave. Their sum is equal to unity and the evanescent waves do not carry any amount of energy flux.

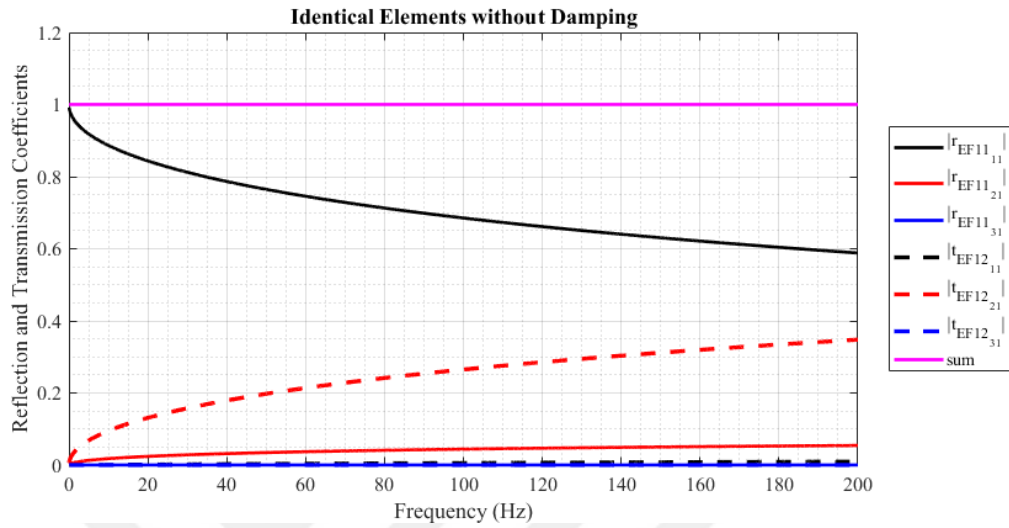


Figure 5.4. Absolute value of the real part of the reflection and transmission coefficients of longitudinal energy flux at an L joint (undamped case).

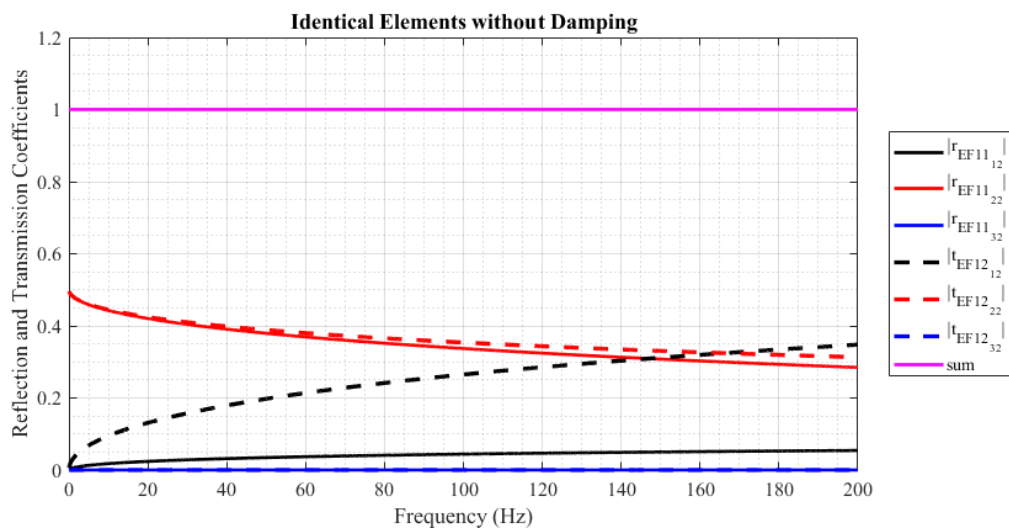


Figure 5.5. Absolute value of the real part of the reflection and transmission coefficients of far-field energy flux at an L joint (undamped case).

Figure 5.6 shows that the energy flux related to the evanescent waves reflected and transmitted without mode conversion.

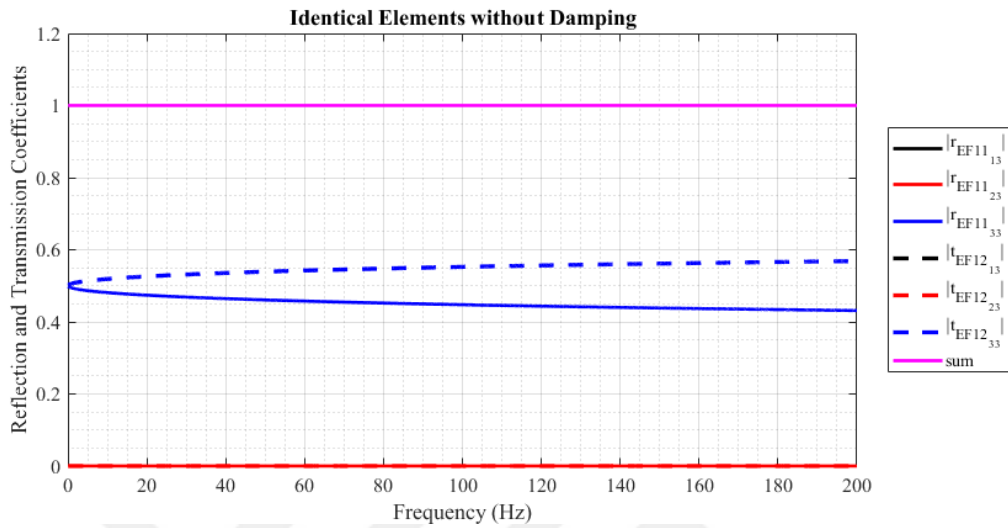


Figure 5.6. Absolute value of the real part of the reflection and transmission coefficients of near-field energy flux at an L joint (undamped case).

When damping is introduced to the system, the transportation mechanism of the energy flux mainly remains the same. Evanescent waves carry negligibly small amount of energy flux. In case of identical elements either with damping or not, $\mathbf{t}_{\mathbf{EF}12}$ and $\mathbf{t}_{\mathbf{EF}21}$, and $\mathbf{r}_{\mathbf{EF}11}$ and $\mathbf{r}_{\mathbf{EF}22}$ are symmetric matrices, which are equal.

Figure 5.10, represents the transmitted and reflected waves at a T joint corresponding to an incident wave from the first element. The members are assumed to be identical.

Figures 5.11 to 5.16 show the absolute values of the real parts of the energy flux coefficients of transmitted and reflected waves at a T joint. Figure 5.11 to 5.13 illustrate the reflection and transmission coefficients for the undamped case whereas Figure 5.14 to 5.16 stand for the damped case. When damping is introduced to the system, negligibly small amount of energy flux is carried by the evanescent waves.

Figure 5.11 shows that, the major part of the energy flux, incident from the first element as longitudinal wave, is transmitted into the third element as longitudinal

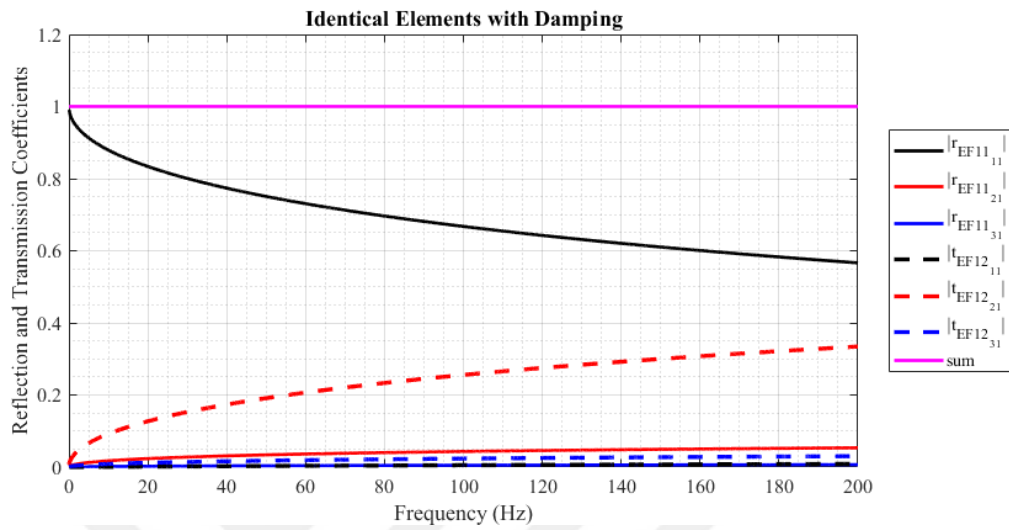


Figure 5.7. Absolute value of the real part of the reflection and transmission coefficients of longitudinal energy flux at an L joint (damped case).

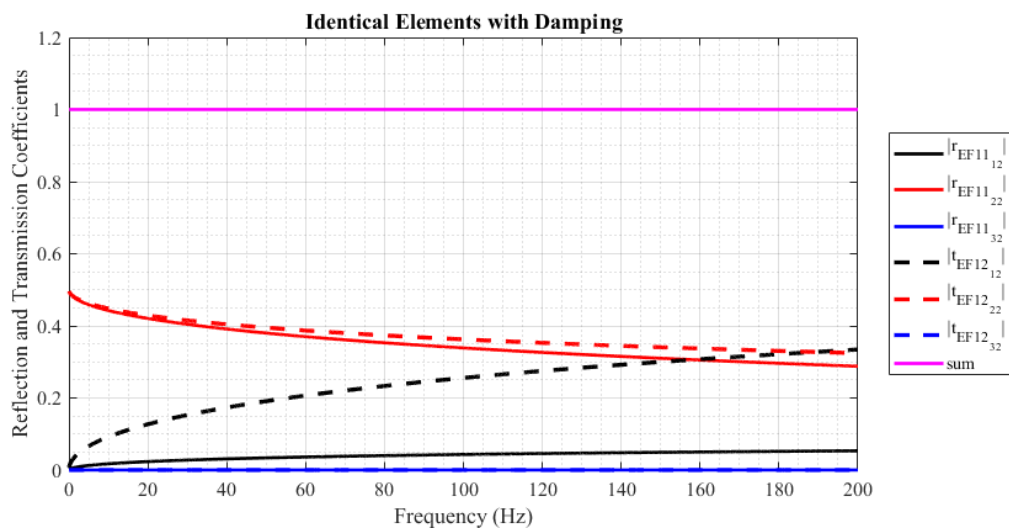


Figure 5.8. Absolute value of the real part of the reflection and transmission coefficients of far-field energy flux at an L joint (damped case).

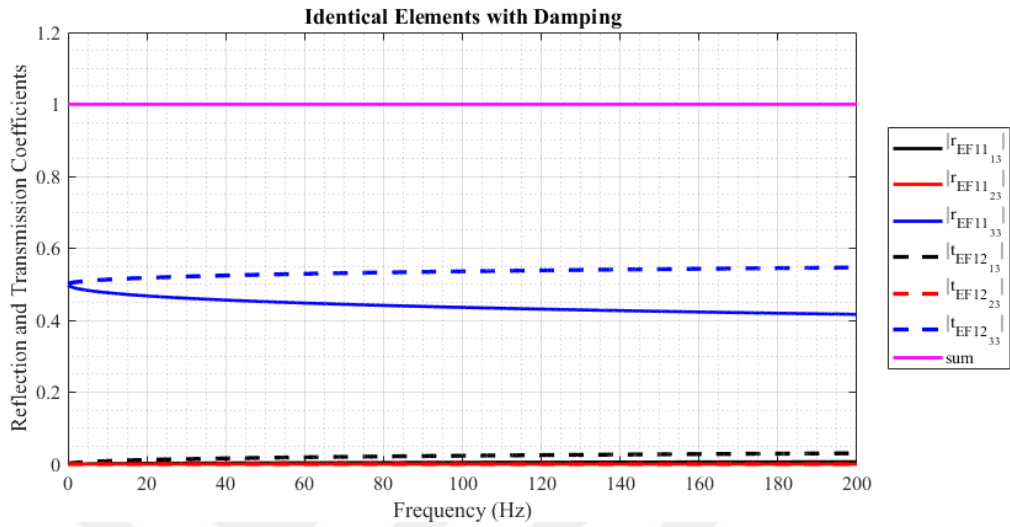


Figure 5.9. Absolute value of the real part of the reflection and transmission coefficients of near-field energy flux at an L joint (damped case).

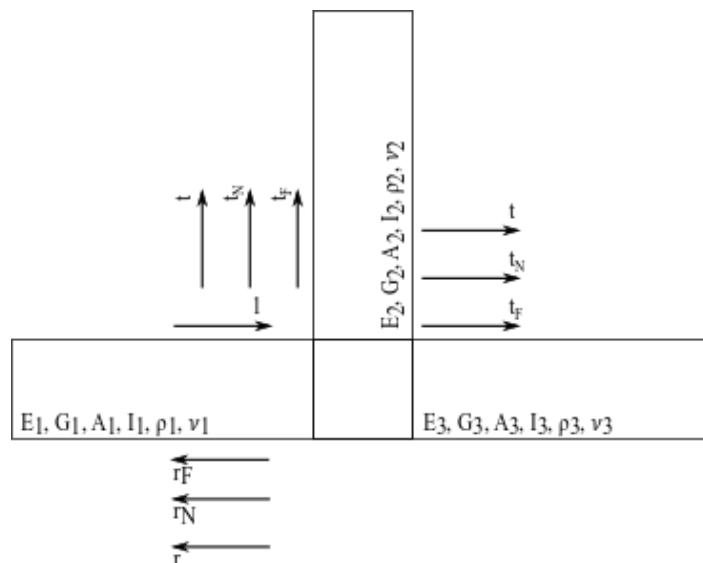


Figure 5.10. Transmitted and reflected waves at a T joint corresponding to the incident wave from the first element.

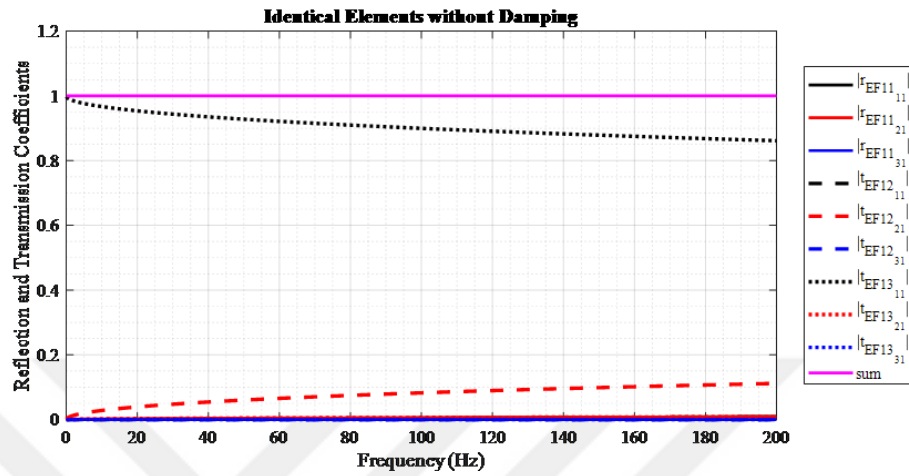


Figure 5.11. Absolute value of the real part of the reflection and transmission coefficients of longitudinal energy flux at a T joint (undamped case).

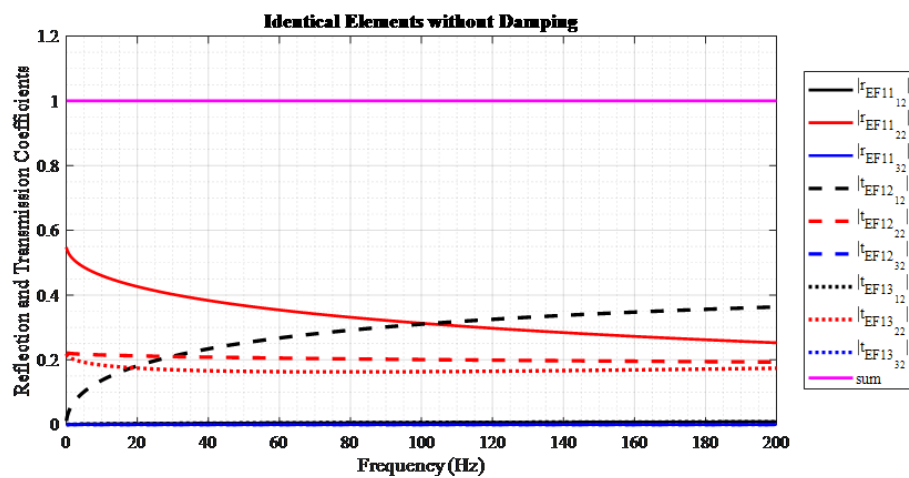


Figure 5.12. Absolute value of the real part of the reflection and transmission coefficients of far-field energy flux at a T joint (undamped case).

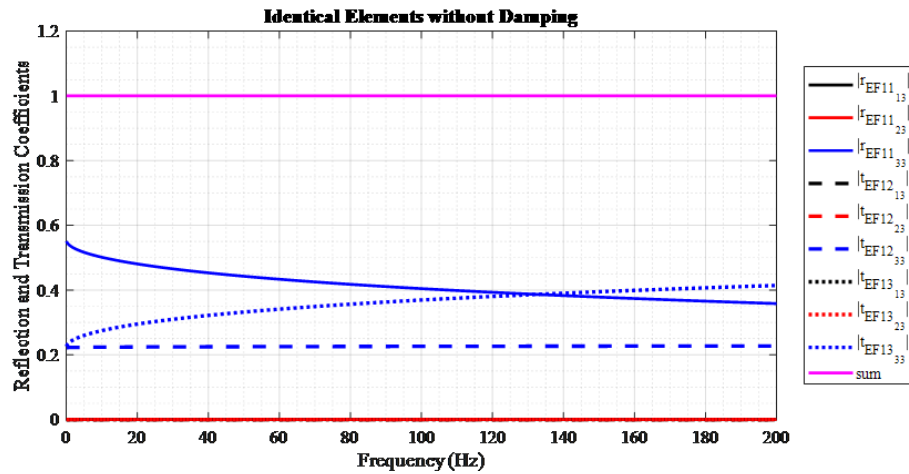


Figure 5.13. Absolute value of the real part of the reflection and transmission coefficients of near-field energy flux at a T joint (undamped case).

wave. Some amount is transmitted into the second element as far-field flexural energy flux. Negligibly small amount is transmitted into the third element as far-field flexural energy flux, reflected as far-field flexural and longitudinal energy flux.

Figure 5.12 illustrates the transfer mechanism of the far-field energy flux, incident from the first element. Major part of the energy flux is reflected and transmitted as flexural energy flux. The amount of the energy flux, transmitted as longitudinal energy flux increases with the frequency.

The evanescent waves are transmitted and reflected as evanescent waves, as can be seen from Figure 5.13.

Figure 5.14, Figure 5.15 and Figure 5.16 show that, when damping is introduced, negligibly small amount of the incident energy flux is transmitted and reflected by evanescent waves.

The energy flux reflection and transmission coefficients at a cross-joint is presented as the last example. It is assumed that the members are identical, and the wave is initiated from the first element.

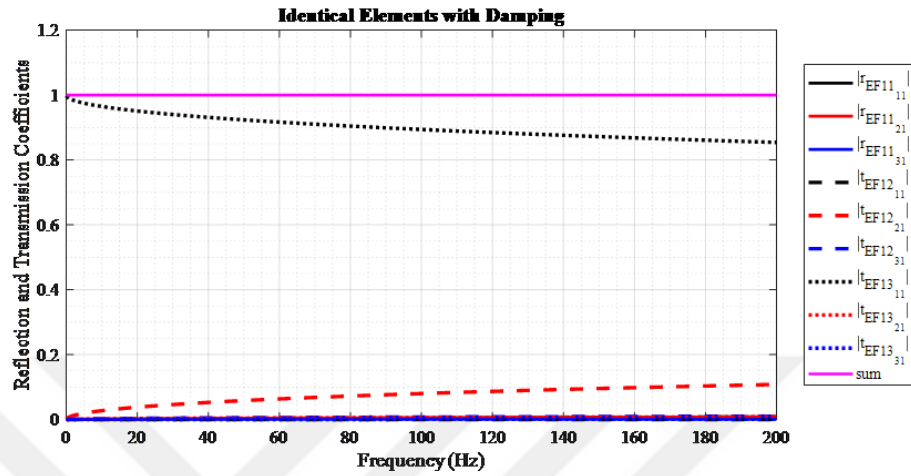


Figure 5.14. Absolute value of the real part of the reflection and transmission coefficients of longitudinal energy flux at a T joint (damped case).

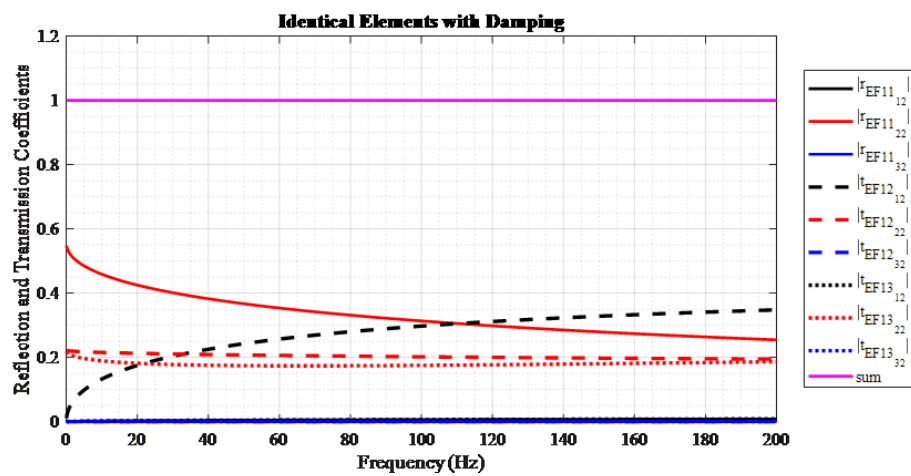


Figure 5.15. Absolute value of the real part of the reflection and transmission coefficients of far-field energy flux at a T joint (damped case).

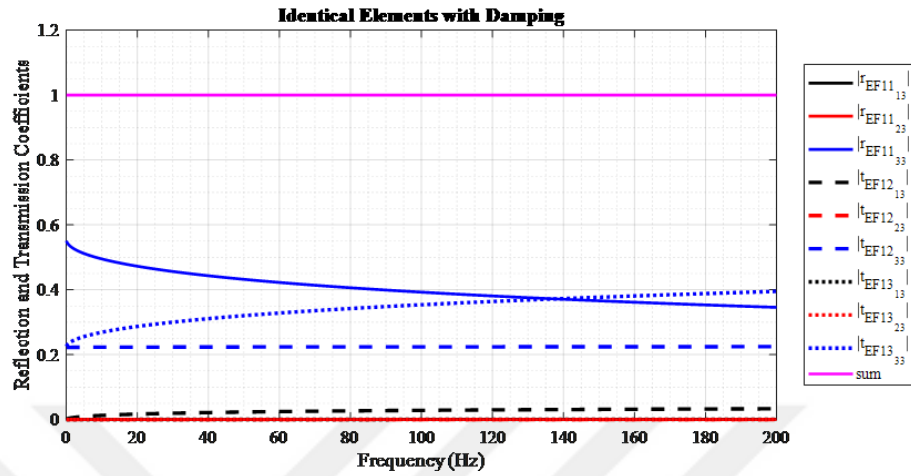


Figure 5.16. Absolute value of the real part of the reflection and transmission coefficients of near-field energy flux at a T joint (damped case).

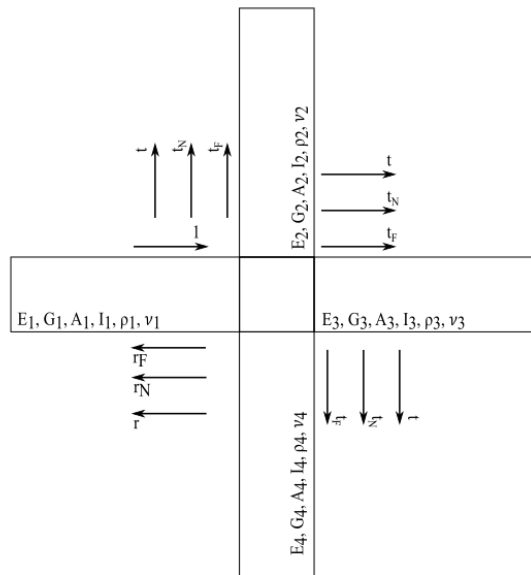


Figure 5.17. Transmitted and reflected waves at a cross joint corresponding to the incident wave from the first element.

The reflection and transmission coefficients at a cross-joint for the undamped case are presented in Figure 5.18 through Figure 5.20. Figure 5.21 to Figure 5.23, shows the energy flux reflection and transmission coefficients for the damped case.

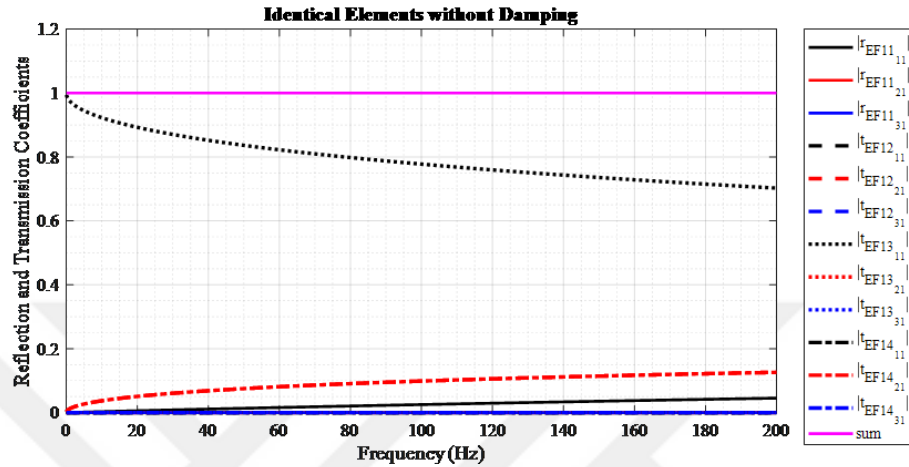


Figure 5.18. Absolute value of the real part of the reflection and transmission coefficients of longitudinal energy flux at a cross joint (undamped case).

According to Figure 5.18, the incident longitudinal energy flux from the first element is transmitted into the third element as longitudinal energy flux, and into the second and fourth elements as far-field flexural energy flux. Some amount of energy flux is reflected as longitudinal energy flux.

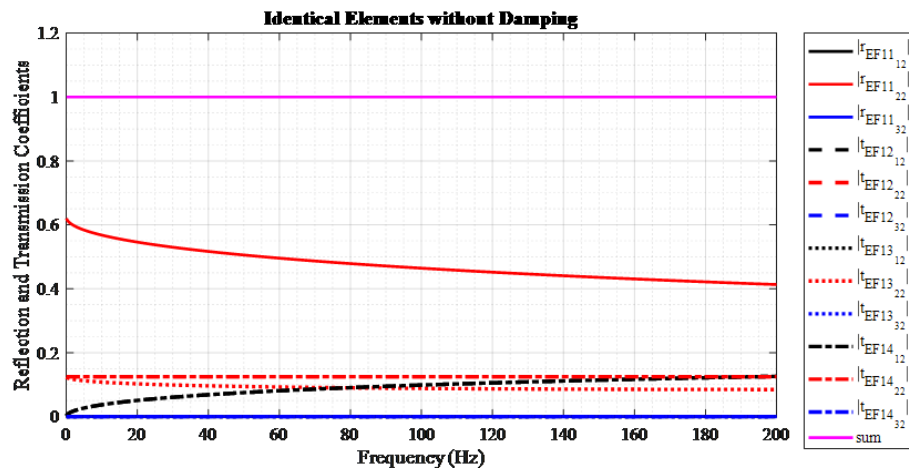


Figure 5.19. Absolute value of the real part of the reflection and transmission coefficients of far-field energy flux at a cross joint (undamped case).

Figure 5.19 reveals that, the incident far field flexural energy flux is reflected as

far-field flexural energy flux. Some amount is transmitted into the adjacent members as longitudinal and far-field flexural energy fluxes. In case of undamped structures, the evanescent waves are transmitted and reflected without mode conversion at a cross joint.

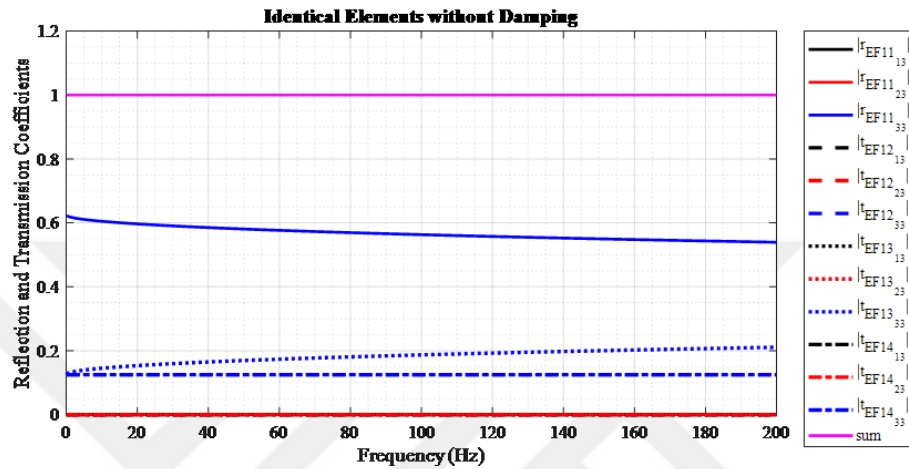


Figure 5.20. Absolute value of the real part of the reflection and transmission coefficients of near-field energy flux at a cross joint (undamped case).

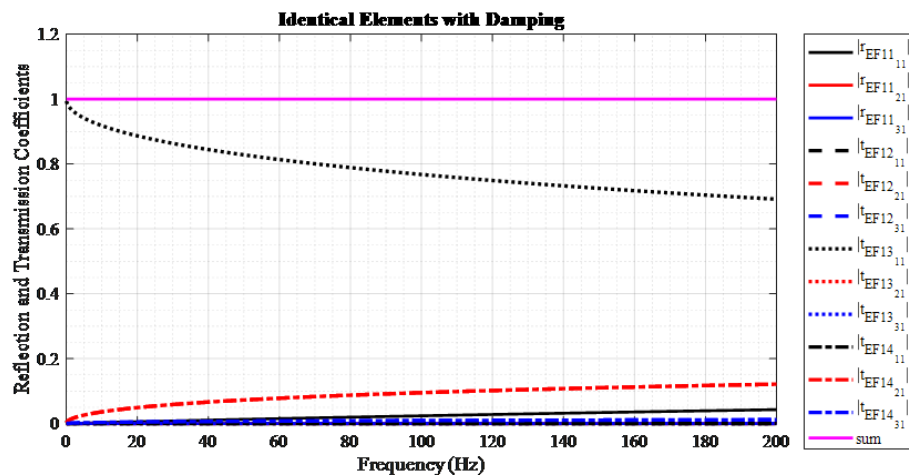


Figure 5.21. Absolute value of the real part of the reflection and transmission coefficients of longitudinal energy flux at a cross joint (damped case).

When damping is introduced, evanescent waves become travelling waves, which carry energy flux throughout the structure. The amount of the energy flux carried by the evanescent waves is negligibly smaller than the energy flux carried by the longitudinal and far-field flexural waves.

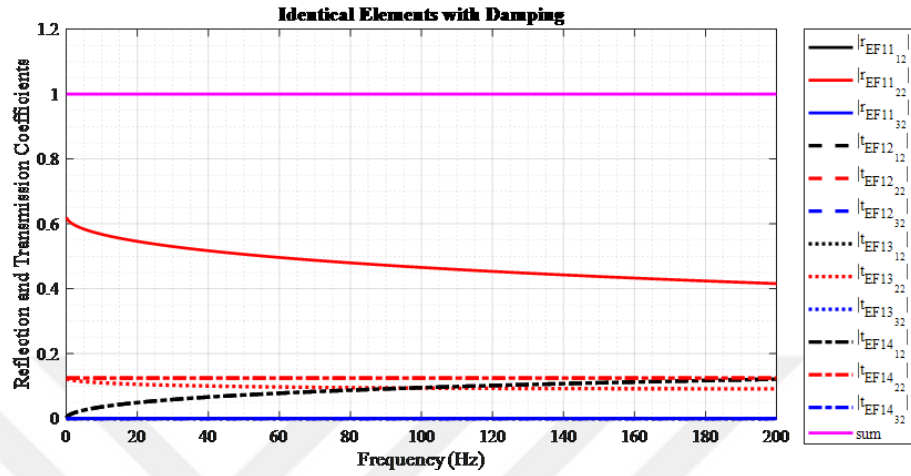


Figure 5.22. Absolute value of the real part of the reflection and transmission coefficients of far-field energy flux at a cross joint (damped case).

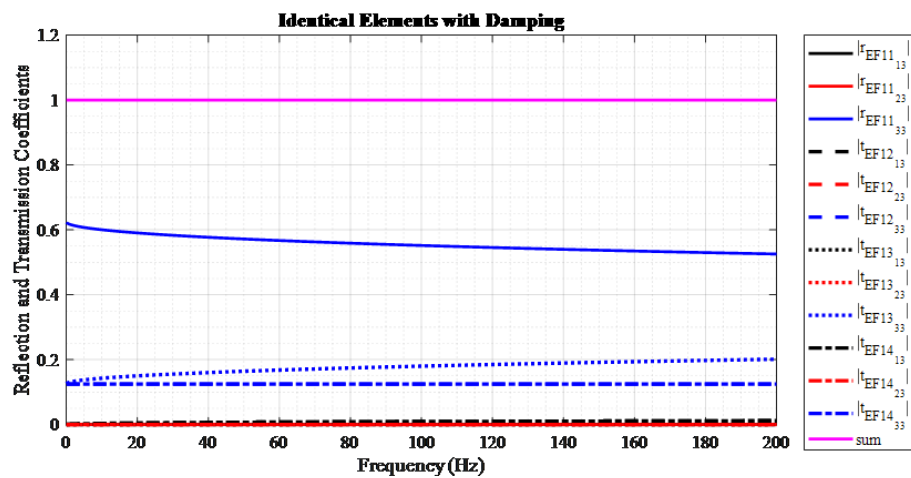


Figure 5.23. Absolute value of the real part of the reflection and transmission coefficients of near-field energy flux at a cross joint (damped case).

5.2. Input Energy Flux

The energy flux that enters the system is calculated using the generation matrix presented by Beale and Accorsi [38]. The amplitudes of the displacement wave modes that cause system to vibrate are the product of the generation matrix and the forces/displacements that excite the system. Then, the amplitudes of velocity wave modes are calculated by multiplying the displacement wave modes by $i\omega$. Since the energy flux is the product of the kinetic energy and the velocity of seismic waves, the input energy flux is calculated as;

$$EF_{in} = \mathbb{R} \left\{ \frac{1}{2} \left\{ \begin{array}{l} \rho A c_{gR} |\dot{u}|^2 \\ \rho A c_{gFB} |\dot{v}_F|^2 \\ \rho A c_{gNB} |\dot{v}_N|^2 \end{array} \right\} \right\} \quad (5.16)$$

In Eq. 5.16, superscript dot corresponds to the first derivative of the displacement with respect to time.

5.3. Assemblage Procedure

In order to obtain dynamic response of a structure in terms of energy flux, the reflection and transmission matrices calculated at each joint must be assembled to form the structure. Then, the scattering matrix of a structure that comprises N number of elements are derived as:

$$\mathbf{S}_{EF} = \mathbb{R} \left[\begin{array}{cccc} \mathbf{S}_{EF1} & & & \\ & \mathbf{S}_{EF2} & & \\ & & \mathbf{O} & \\ & & & \mathbf{S}_{EFN} \end{array} \right] \quad (5.17)$$

The amplitudes of the generated energy flux at adjacent joints are calculated through system transmission matrices, which are diagonal matrices. The square of the

exponential part of the waveguide equations, which corresponds to the waves traveling in the direction of increasing spatial coordinate with respect to member's corresponding local coordinate system, is substituted into diagonal of the system transmission matrix ($\mathbf{ST}_{\mathbf{EF}}$). To assign the amplitude of the energy flux at a joint caused by the energy flux generated at an adjacent joint, a permutation matrix ($\mathbf{P}_{\mathbf{EF}}$) is defined. For instance, the outgoing energy flux u_{EFo1_1} at joint 1 in Figure 5.24 becomes incoming energy flux u_{EFi2_1} at joint 2. The amplitude of the incoming energy flux can be related to the outgoing energy flux by means of the system transmission and permutation matrices.

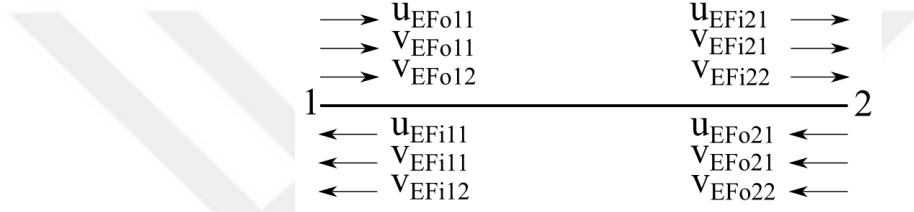


Figure 5.24. Energy flux through an element.

$\mathbf{ST}_{\mathbf{EF}}$ and $\mathbf{P}_{\mathbf{EF}}$ matrices based on elementary rod and Bernoulli-Euler beam theories are defined as:

$$\begin{pmatrix} u_{EFi1_1} \\ v_{EFi1_1} \\ v_{EFi1_2} \\ u_{EFi2_1} \\ v_{EFi2_1} \\ v_{EFi2_2} \end{pmatrix} = [\mathbf{ST}_{\mathbf{EF}}] [\mathbf{P}_{\mathbf{EF}}] \begin{pmatrix} u_{EFo1_1} \\ v_{EFo1_1} \\ v_{EFo1_2} \\ u_{EFo2_1} \\ v_{EFo2_1} \\ v_{EFo2_2} \end{pmatrix} \quad (5.18)$$

where,

$$[\mathbf{ST}_{\mathbf{EF}}] = \begin{bmatrix} e^{-2ik_R x} & & & & & \\ & e^{-2ik_B x} & & & & \\ & & e^{-2k_B x} & & & \\ & & & e^{-2ik_R x} & & \\ & & & & e^{-2ik_B x} & \\ & & & & & e^{-2k_B x} \end{bmatrix}$$

$$[\mathbf{P}_{\mathbf{EF}}] = \begin{bmatrix} 0 & 0 & 0 & 1 & 0 & 0 \\ 0 & 0 & 0 & 0 & 1 & 0 \\ 0 & 0 & 0 & 0 & 0 & 1 \\ 1 & 0 & 0 & 0 & 0 & 0 \\ 0 & 1 & 0 & 0 & 0 & 0 \\ 0 & 0 & 1 & 0 & 0 & 0 \end{bmatrix}$$

For a structure that comprises N number of elements, the incoming and outgoing energy fluxes are related to each other as:

$$\begin{Bmatrix} \mathbf{U}_{\mathbf{EF}i1} \\ \mathbf{U}_{\mathbf{EF}i2} \\ \vdots \\ \mathbf{U}_{\mathbf{EF}iN} \end{Bmatrix} = \begin{bmatrix} \mathbf{ST}_{\mathbf{EF}1}\mathbf{P}_{\mathbf{EF}1} & & & \\ & \mathbf{ST}_{\mathbf{EF}2}\mathbf{P}_{\mathbf{EF}2} & & \\ & & \ddots & \\ & & & \mathbf{ST}_{\mathbf{EF}N}\mathbf{P}_{\mathbf{EF}N} \end{bmatrix} \begin{Bmatrix} \mathbf{U}_{\mathbf{EF}o1} \\ \mathbf{U}_{\mathbf{EF}o2} \\ \vdots \\ \mathbf{U}_{\mathbf{EF}oN} \end{Bmatrix} \quad (5.19)$$

Amplitude of the outgoing energy flux is calculated as:

$$\{\mathbf{U}_{\mathbf{EF}o}\} = \{[\mathbf{I} - \mathbf{S}_{\mathbf{EF}} * \mathbf{ST}_{\mathbf{EF}} * \mathbf{P}_{\mathbf{EF}}]^{-1} \mathbf{EF}_{\mathbf{in}}\} \quad (5.20)$$

where, \mathbf{I} is the identity matrix. Then, the net energy flux is calculated as:

$$\{\mathbf{U}_{\mathbf{EFnet}}\} = \mathbb{R} \{ \{\mathbf{U}_{\mathbf{EF}o}\} - \{\mathbf{U}_{\mathbf{EF}i}\} \} \quad (5.21)$$

6. SOIL STRUCTURE INTERACTION

The dynamic response of a structure is influenced by the interactions between the superstructure, the foundation, and the soil medium surrounding the foundation. The motion of the foundation deviates from the free field motion due to the deformations occur while the incident waves travelling through the soil medium into the structure. Besides the response of the soil, generation of the base shear and moments cause displacements and rotations at the foundation-soil interface, as well as additional waves in the soil, as the waves travel through the superstructure. In literature, this process is referred as ‘Soil-Structure Interaction (SSI)’ and comprises two successive mechanisms. Modification of the free field motion is referred to ‘Kinematic Interaction’. Superstructure induced vibrations are influenced by the flexibility of the soil-foundation system and referred to as ‘Inertial Interaction’. ‘Foundation Impedance Functions (FIF)’ define the stiffness and damping properties of the soil-foundation system. FIF depend on the frequency and mode of the vibration, the properties of the foundation system (geometry, embedment, etc.) and the properties of the soil (shear wave velocity, Poisson’s ratio, etc.). For structures susceptible to SSI (e.g. heavy structures founded on soft soil), it is important that seismic forces and displacements are calculated by considering the effects of SSI [4].”

In this chapter, we demonstrate the applicability of the existing foundation impedance functions in SEM, TWM and Energy Flux analysis. Detailed information on the past studies can be found in the papers by Kausel [48], Gazetas [49] and Stewart, Fenves and Seed [50]. Various numerical example on SSI can be found in the papers by Gazetas [51] and Mylonakis, Nikolaou and Gazetas [52]. These two papers also provide foundation impedance functions for various types of foundations with different soil properties. The foundation impedance functions for different type of foundations can be found in the handbook by Sieffert and Cevaer [53].

FIM for a surface foundation subjected to vertically propagating S waves are

given as [52],

$$U_{FFM} \cong U_{FIM} \quad (6.1)$$

$$\phi_{FIM} \cong 0 \quad (6.2)$$

where, U_{FFM} , U_{FIM} and ϕ_{FIM} are respectively the translational component of the free field motion, the translational component of the FIM and the rocking component of the FIM. FIFs are expressed by using one of the two forms given below:

$$K_j = K_{Sj} [K_j(a_0) + ia_0 C_j(a_0)] \quad (6.3)$$

$$K_j = K_{j1}(a_0) + iK_{j2}(a_0) \quad (6.4)$$

where, K_j or K_{j1} are the frequency dependent dynamic stiffness and C_j or K_{j2} are the radiation damping coefficient of j^{th} wave mode, a_0 is the dimensionless frequency and K_{sj} is the static stiffness. Dimensionless frequency a_0 is defined by,

$$a_0 = \frac{\omega B}{V_s} \quad (6.5)$$

where, ω is the circular frequency, B is the half-width of the foundation, and V_s is the shear wave velocity. Shear wave velocity of the soil is calculated as,

$$V_s = \sqrt{\frac{G}{\rho}} \quad (6.6)$$

where, G is the shear modulus of the soil and ρ is the mass density of per unit volume of the soil.

Figures below represent the impedance functions for a rectangular footing resting on a homogenous half-space with Poisson's ratio of 0.33 [53]. In the figures, K_v is the normalized stiffness in the vertical direction, K_h is the normalized stiffness in the horizontal direction, K_r is the normalized stiffness about the horizontal direction and K_{hr} is the normalized coupling stiffness. Impedance functions for foundations with

different foundation types and soil properties can be found in [51–53].

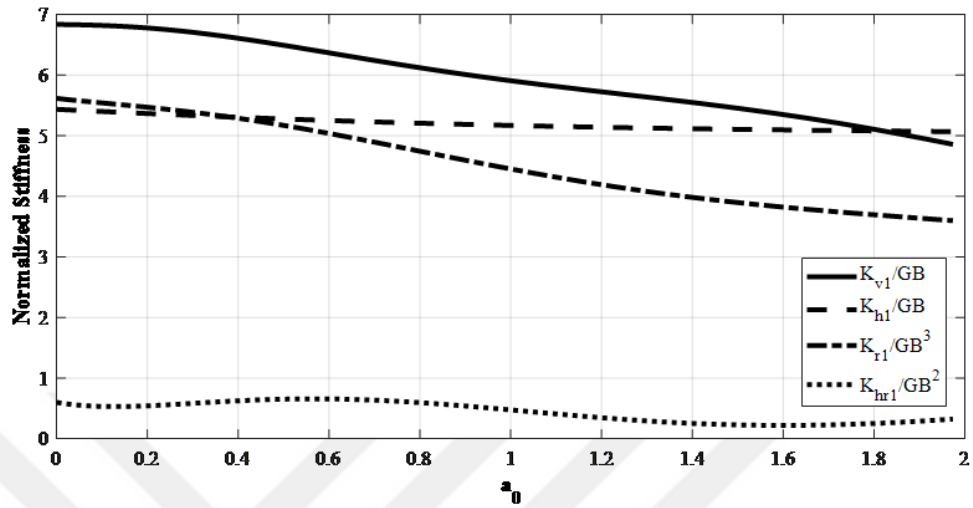


Figure 6.1. Normalized stiffness terms.

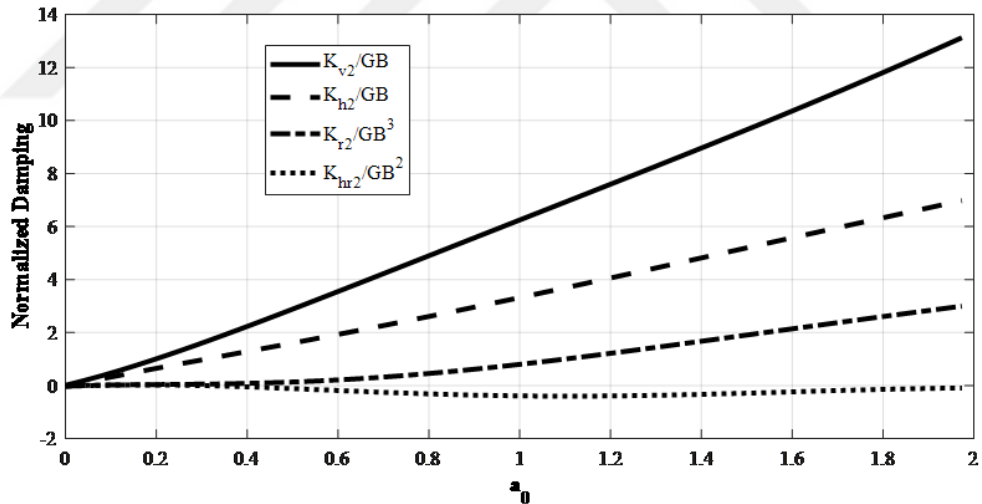


Figure 6.2. Normalized damping terms.

6.1. Coupling the Soil and the Structure

In soil-structure interaction analysis, the foundation is represented by springs and dashpots. The foundation impedance functions reflect the properties of the spring and dashpot system in accordance with the soil and foundation properties and the mode of the vibration. The soil-structure system is idealized as demonstrated in Figure 6.3.



Figure 6.3. Representation of soil-structure system.

Foundation impedance function in matrix form is written as follows,

$$\begin{Bmatrix} F \\ V \\ M \end{Bmatrix} = \begin{bmatrix} K_h & 0 & K_{hr} \\ 0 & K_v & 0 \\ K_{hr} & 0 & K_r \end{bmatrix} \begin{Bmatrix} u \\ v \\ \phi \end{Bmatrix} \quad (6.7)$$

In Eq. 6.7, u and v represent the displacements in the global x and y directions, respectively, and F and V are the forces related to them. ϕ is the rotation about z axis and M is the moment. K_h is the impedance function in the longitudinal direction, K_v is in the vertical direction, K_r is the rocking impedance and K_{hr} is the coupling term. In case of shallow foundations, the coupling term can be neglected.

In spectral element method, foundation impedance functions can be directly superimposed to the spectral element matrix of the superstructure.

In travelling wave method, soil structure interaction is defined by imposing the foundation impedance function into the equilibrium and boundary conditions. The load that produces the required displacement at that degree of freedom is added as an applied load and the internal force produced due to the imposed displacement is added to the force equilibrium. This is done by replacing the related terms of β matrix given in Eq. 4.28 by the foundation impedance.

In the calculation of energy flux, soil structure interaction is incorporated in the analysis as it is done for the TWM.

6.2. Numerical Examples

In this section the same plane frame presented in the Section 3.4 is analyzed under the effect of the same base excitation considering the soil structure interaction using SEM and TWM. In the SEM model, the soil is modeled as springs having the stiffness equal to the foundation impedance functions. The stiffness of the soil is superimposed to the stiffness of the superstructure. In the TWM model, the β matrix given by Eq. 4.28 is replaced with the foundation impedance function.

Two SEM and two TWM models are used in order to see the effects of adopting higher order theories on the dynamic response. In the first SEM and TWM models, elementary theories are adopted. In the second SEM and TWM models, higher order theories, namely, Love rod and Timoshenko beam theories, are used in the formulation of structural elements.

The foundation impedance functions are calculated for a square base with 1.0*1.0 m. dimensions. Normalized stiffness and damping terms are presented in the Figure 6.1 and Figure 6.2, respectively. Foundation impedance functions are derived using these charts, dimensions of the base and properties of the soil. In order to demonstrate the effect of the soil class on the calculated response, soils with the average shear wave velocities of 250 m/s. and 1000 m/s., which correspond to stiff soil and rock, are selected.

Frequency domain response calculated at the DOF= 52 of Figure 3.12, which corresponds to the top displacement in the global x direction. The response calculated from the first and the second SEM models with and without considering SSI are presented in Figure 6.4 and Figure 6.5, respectively. If the stiff soil case is considered, with the introduction of SSI the calculated displacement is both amplified and de-amplified at certain frequencies. On the other hand, when the soil class is assumed to be rock,

the calculated displacement becomes closer to the rigid base case. Besides the effects on the calculated displacement response, the modal properties of the structure are also changed by the SSI.

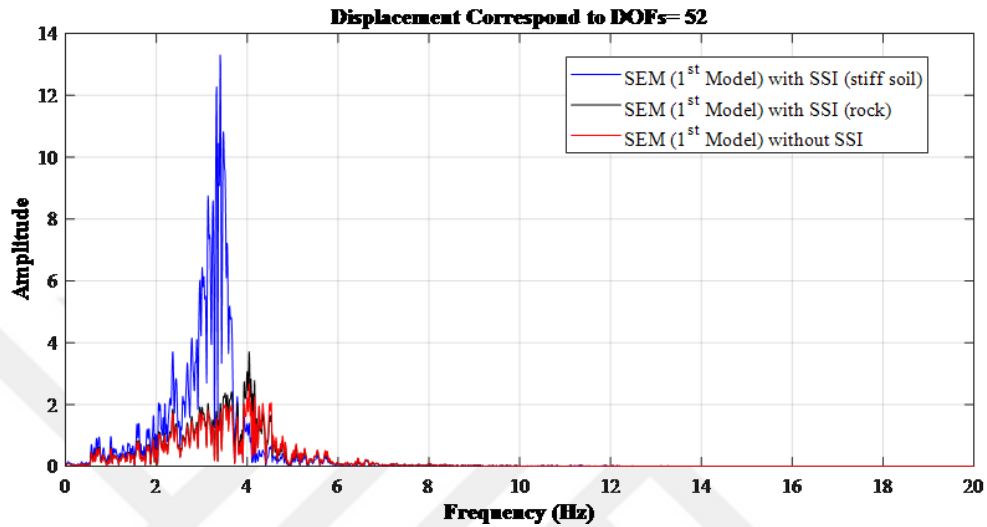


Figure 6.4. Frequency domain response at DOF= 52 calculated from the first SEM model with and without considering SSI.

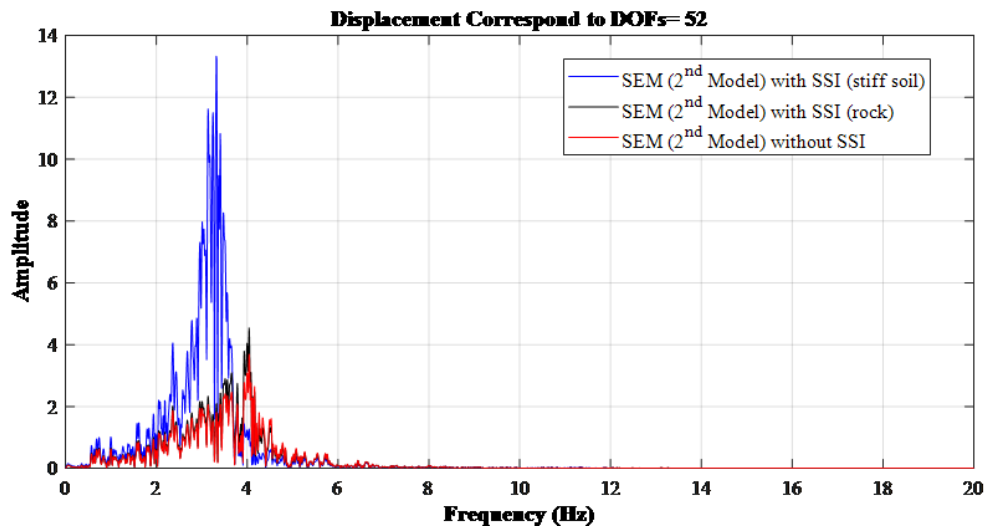


Figure 6.5. Frequency domain response at DOF= 52 calculated from the second SEM model with and without considering SSI.

Figure 6.6 and Figure 6.7 illustrate the response at DOF= 52 in the time domain. When the soil class is assumed to be stiff soil, SSI causes to increase the displacement considerably.

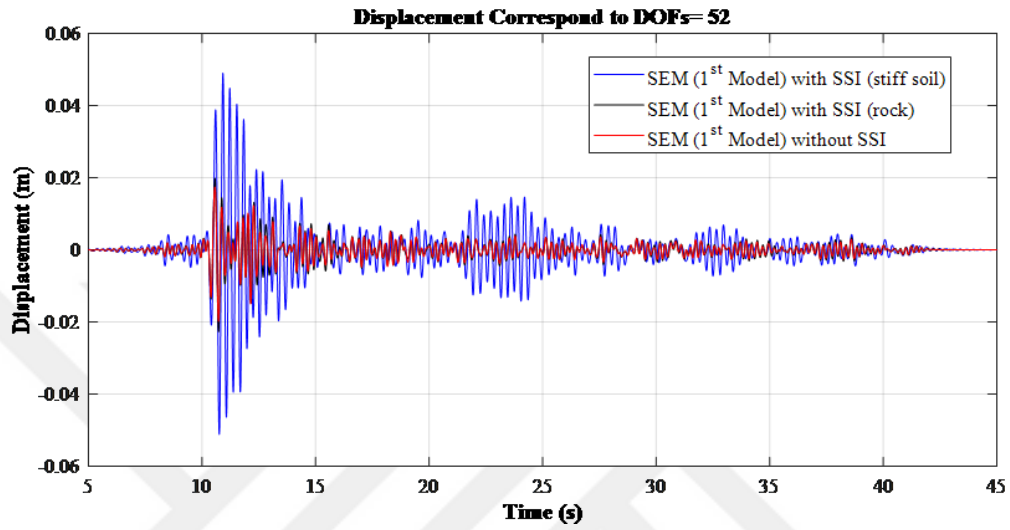


Figure 6.6. Time domain response at DOF= 52 calculated from the first SEM model with and without considering SSI.

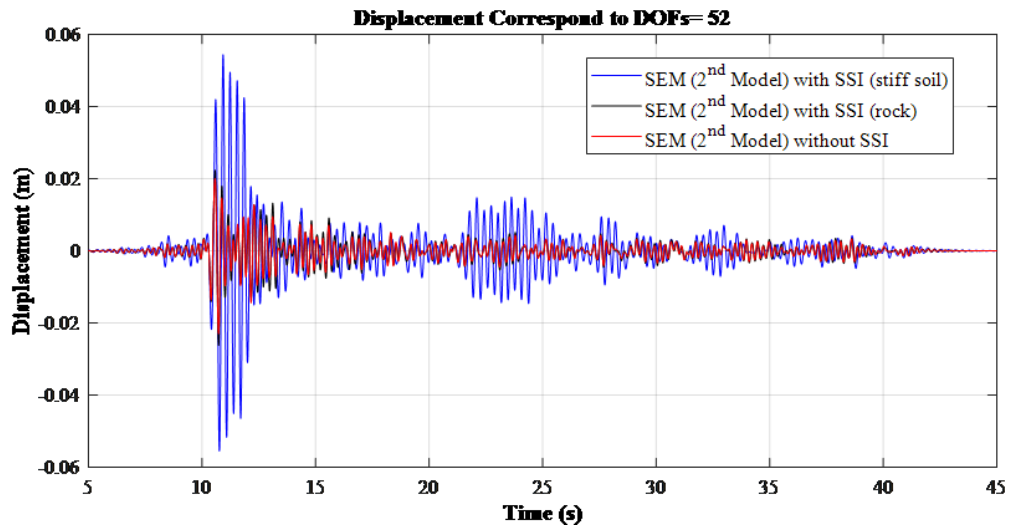


Figure 6.7. Time domain response at DOF= 52 calculated from the second SEM model with and without considering SSI.

Figure 6.8 and Figure 6.9 show the calculated base shear from the first and the second SEM models with and without considering the SSI. Introduction of SSI causes to decrease in the base shear whether the soil class is decided as stiff soil or rock.

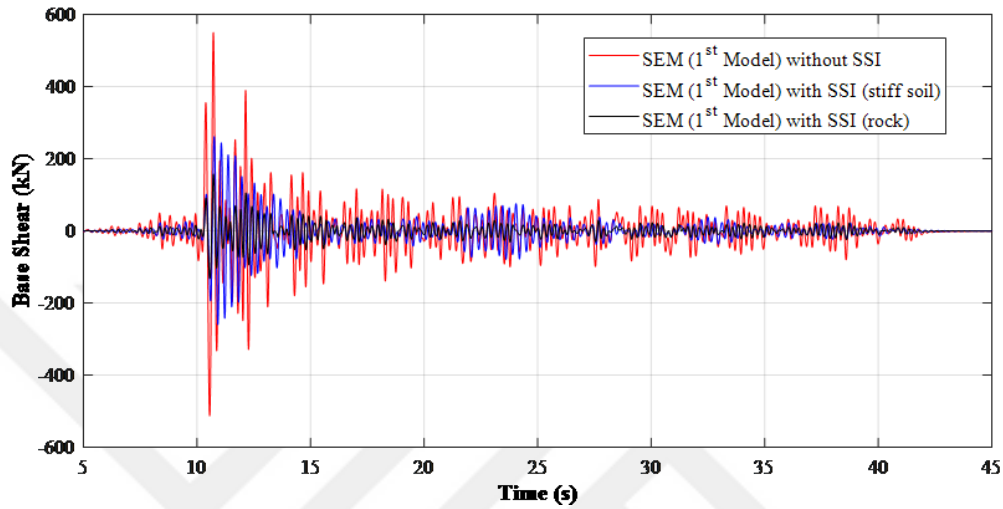


Figure 6.8. Base shear in the time domain calculated from the first SEM model with and without considering SSI.

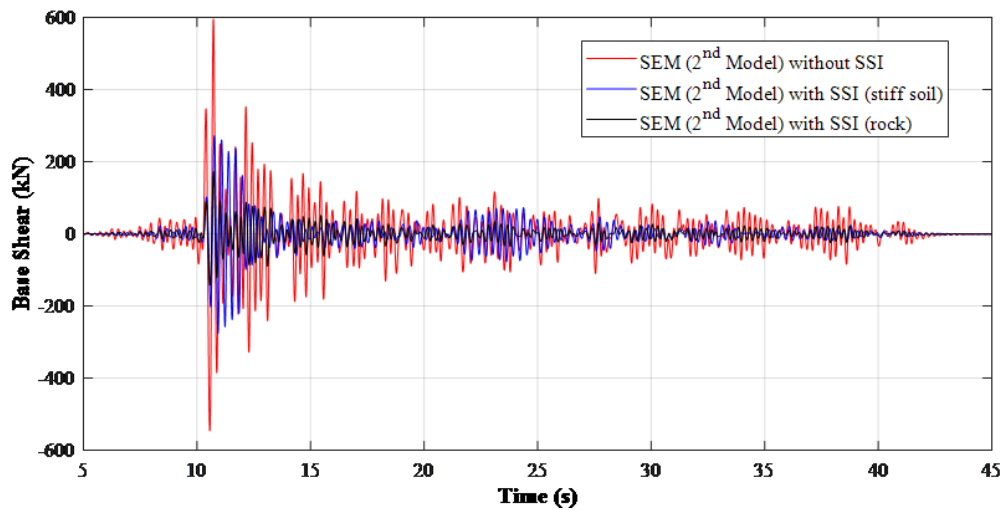


Figure 6.9. Base shear in the time domain calculated from the second SEM model with and without considering SSI.

The response calculated from the first and the second TWMM models with and without considering SSI are presented in Figure 6.10 and Figure 6.11, respectively. If the stiff soil is selected, introduction of SSI causes both amplification and de-

amplification of the response at certain frequencies. Besides the effects on the calculated displacement response, the modal properties of the structure are also changed by the SSI.

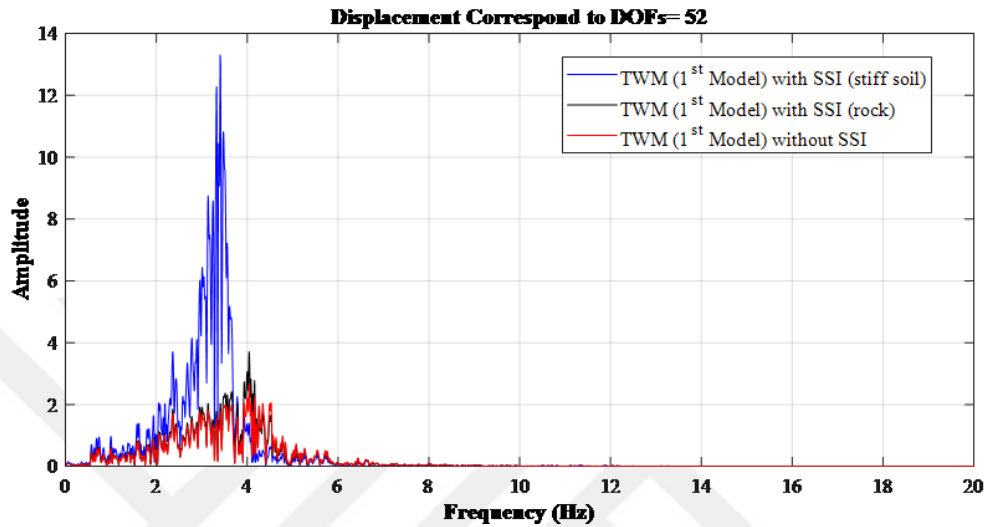


Figure 6.10. Frequency domain response at DOF= 52 calculated from the first TWM model with and without considering SSI.

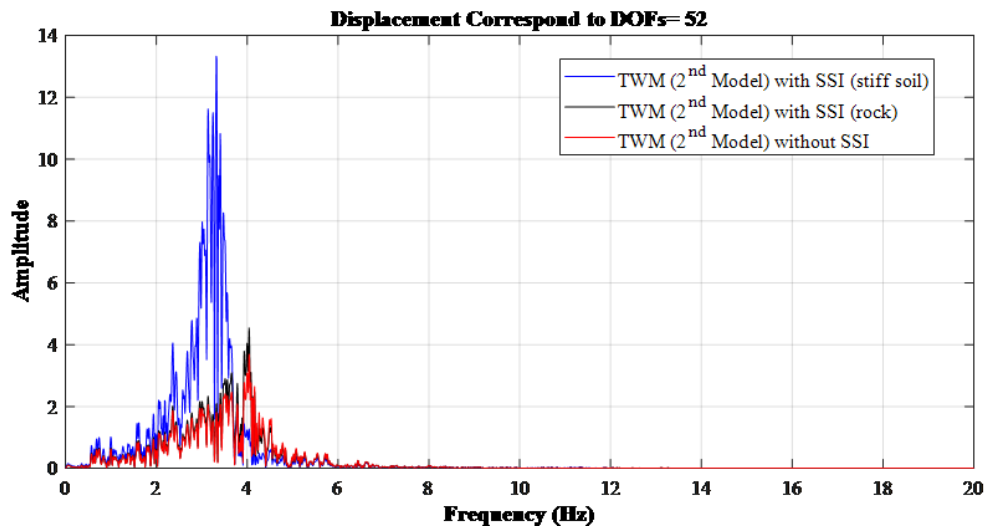


Figure 6.11. Frequency domain response at DOF= 52 calculated from the second TWM model with and without considering SSI.

Figure 6.12 and Figure 6.13 illustrate response at DOF= 52 in the time domain. When the SSI is considered, in case of stiff soil, the displacement is amplified considerably.

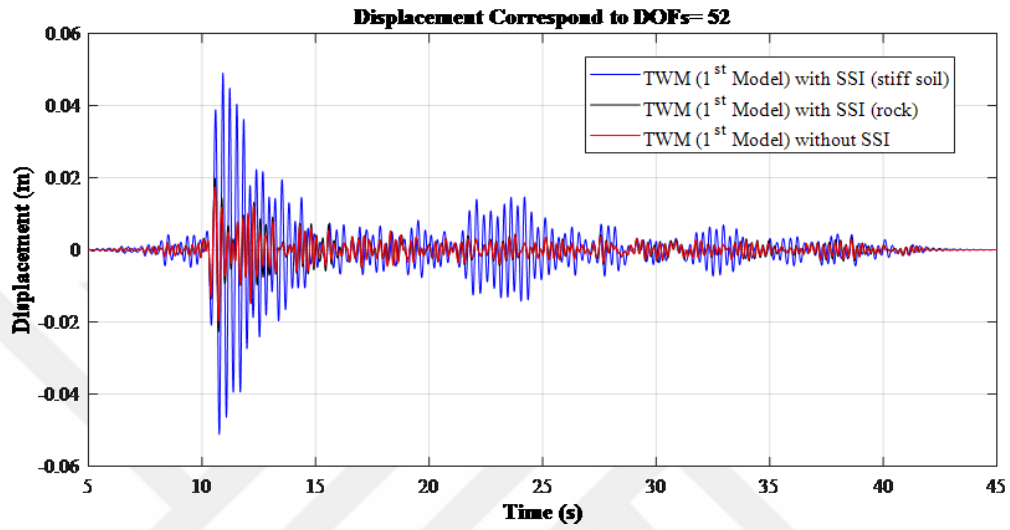


Figure 6.12. Time domain response at DOF= 52 calculated from the first TWM model with and without considering SSI.

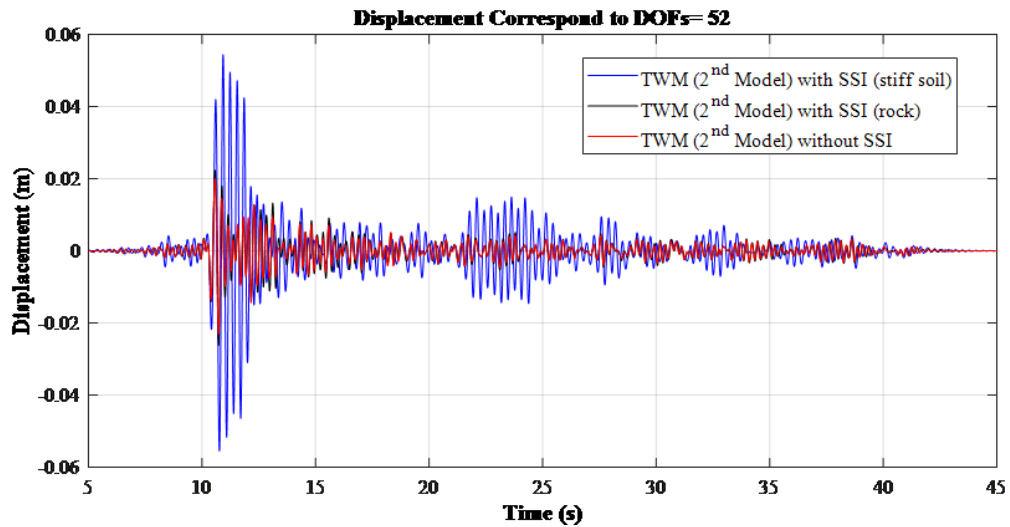


Figure 6.13. Time domain response at DOF= 52 calculated from the second TWM model with and without considering SSI.

The response calculated based on SEM and TWM analysis for both with and without considering SSI are approximately identical. Thus, the figures related to the base shear is not presented.



7. CONCLUSIONS

This thesis presents the methodology and the applications of the Spectral Element, Travelling Wave, and Energy Flux methods in the dynamic analysis of engineering structures. These methods are highly efficient in analyzing the dynamic response and identifying the dynamic characteristics of engineering structures in the frequency domain. Conventional Finite Element Method is not able to capture the dynamic response accurately in the medium to high frequency range, unless the mesh size used in modeling is smaller than the shortest wavelength. Thus, these new techniques are more reliable for the dynamic analysis and damage detection in structures at high frequencies.

The procedure to assemble arbitrarily oriented members, and the formulation of the spectral element matrices based on elementary and higher order theories are presented for planar frames. This assembly procedure can be extended to space frames. However, the space frame case is not covered in this thesis for simplicity. The dynamic response results obtained from the SEM analyses are compared with the FEM analyses' results. The FEM analysis predicts erroneous results in the medium to high frequency range, according to the given examples. The mesh size used in the FEM analysis is reduced in order to improve the accuracy. However, the improved FEM results are not as accurate as the SEM results. On the other hand, SEM cannot be applied directly to nonlinear systems since it is based on the superposition of the wave modes of different frequencies. Various techniques to implement SEM in non-linear analysis of structures can be found in the literature. Even if the method is presented only for one dimensional elements in this document, it can be extended to two dimensional elements. However, if the governing differential equation of the wave solution of an element does not exist, SEM cannot be used in the analysis of structures with such elements.

The TWM analysis, based on the elementary and higher order element theories, is presented in this document. The construction of the reflection, transmission and generation matrices are outlined. The assemblage procedure to handle two-dimensional

plane frame structures are also presented. This method can be extended to the analysis of three-dimensional plane frame elements, as well as to the analysis of two-dimensional waveguides, such as plates. Nonlinear dynamic analysis of structures can be done by using this method. However, since it is based on the superposition of the modes, it cannot be applied directly.

Reflection and transmission coefficients for the energy flux are obtained based only on the elementary theories. The procedure to assemble the elements for a structure is outlined. They can be derived for the higher order theories and assembled to construct a structural system. The derivation of the scattering and generation matrices, and assemblage process are analogous to TWM. Since the incoming and outgoing kinetic energies are stable parameters, energy flux becomes a convenient and reliable method in the dynamic analysis of structures. Moreover, it can be used both in linear and non-linear analysis. By means of the energy flux, the energy demand and energy absorption through a structure can be tracked with respect to frequency or time.

Another advantage of these methods is that Soil-Structure Interaction (SSI) effects can easily be incorporated in the analysis. SSI represents the influence of soil flexibility around the foundation on the response of a structure, and can change the dynamic response substantially. It is a critical factor controlling damage during earthquakes. SSI must be considered in the analysis of structures founded on soft soils. Foundation Impedance Functions (FIF), which represent the stiffness and damping properties of the soil-foundation system, are frequency dependent. Although, impedance functions can be approximated in time domain in the form of recursive filters [4], it is much easier to incorporate them in the frequency domain directly in SEM, TWM and Energy Flux analyses.

REFERENCES

1. Banerjee, J. R., “Dynamic Stiffness Formulation for Structural Elements: A General Approach”, *Computers & Structures*, Vol. 63, No. 1, pp. 101–103, 1997.
2. Gopalakrishnan, S., M. Martin and J. F. Doyle, “A Matrix Methodology for Spectral Analysis of Wave Propagation in Multiple Connected Timoshenko Beams”, *Journal of Sound and Vibration*, Vol. 158, No. 1, pp. 11–24, 1992.
3. Şafak, E., “Characterization of Seismic Hazard and Structural Response by Energy Flux”, *Soil Dynamics and Earthquake Engineering*, Vol. 20, No. 1–4, pp. 39–43, 2000.
4. Şafak, E., “Time-Domain Representation of Frequency-Dependent Foundation Impedance Functions”, *Soil Dynamics and Earthquake Engineering*, Vol. 26, No. 1, pp. 65–70, 2006.
5. Clough, R. W. and J. Penzien, *Dynamics of Structures*, Computers & Structures, Inc., Berkeley, CA, USA, 2003.
6. Doyle, J. F., *Static and Dynamic Analysis of Structures: with an Emphasis on Mechanics and Computer Matrix Methods*, Kluwer Academic Publishers, Dordrecht, Netherlands, 1991.
7. Love, A. E., *A Treatise on the Mathematical Theory of Elasticity*, Dover Publications, New York, NY, USA, 1927.
8. Mindlin, R. D. and G. Herrmann, “A One Dimensional Theory of Compressional Waves in an Elastic Rod”, *In Proceedings of the First U.S. National Congress on Applied Mechanics*, p. 187–191, 1951.
9. Viktorow, I. A., *Rayleigh and Lamb Waves in Physical Theory and Applications*,

Plenum Press, New York, NY, USA, 1967.

10. Krawczuk, M., J. Grabowska and M. Palacz, “Longitudinal Wave Propagation. Part I— Comparison of Rod Theories”, *Journal of Sound and Vibration*, Vol. 295, No. 3–5, pp. 461–478, 2006.
11. Martin, M., S. Gopalakrishnan and J. F. Doyle, “Wave Propagation in Multiply Connected Deep Waveguides”, *Journal of Sound and Vibration*, Vol. 174, No. 4, pp. 521–538, 1994.
12. Doyle, J. F., *Wave Propagation in Structures: Spectral Analysis Using Fast Discrete Fourier Transforms*, Springer Science & Business Media, LLC, New York, NY, USA, 1997.
13. Timoshenko, S. P., “On the Correction for Shear of the Differential Equation for Transverse Vibrations of Prismatic Bars”, *Philosophical Magazine*, Vol. 41, pp. 744–746, 1921.
14. Doyle, J. F., *Wave Propagation in Structures: an FFT-Based Spectral Analysis Methodology*, Springer-Verlag, New York, NY, USA, 1989.
15. Gopalakrishnan, S., *Spectral Analysis of Wave Propagation in Connected Waveguides*, Ph.D. Thesis, Purdue University, 1992.
16. Rizzi, S. A. and J. F. Doyle, “A Spectral Element Approach to Wave Motion in Layered Solids”, *Journal of Vibration and Acoustics*, Vol. 114, No. 4, pp. 569–577, 1992.
17. Rizzi, S. A. and J. F. Doyle, “Spectral Analysis of Wave Motion in Plane Solids with Boundaries”, *ASME, Transactions, Journal of Vibration and Acoustics*, Vol. 114, No. 2, pp. 133–140, 1992.
18. Rose, J. L., *Ultrasonic Guided Waves in Solid Media*, Cambridge University Press,

Cambridge, UK, 2014.

19. Usik, L., *Spectral Element Method in Structural Dynamics*, Wiley, Singapore, 2009.
20. Bathe, K. J., *Finite Element Procedures in Engineering Analysis*, Prentice Hall, Englewood Cliffs, NJ, USA, 1996.
21. Chopra, A. K., *Dynamics of Structures*, Prentice Hall, Englewood Cliffs, NJ, USA, 1995.
22. The MathWorks, I., *MATLAB*, 2018, <http://www.mathworks.com>.
23. Computers and Structures, I., *SAP2000*, 2018, <https://www.csiamerica.com>.
24. Graff, K. F., *Wave Motion in Elastic Solids*, Ohio State University Press, Columbus, OH, USA, 1975.
25. Cremer, L., M. Heckl and B. A. T. Petersson, *Structureborne Sound: Structural Vibrations and Sound Radiation at Audio Frequencies*, Springer-Verlag, Berlin, 2005.
26. Mace, B. R., “Wave Reflection and Transmission in Beams”, *Journal of Sound and Vibration*, Vol. 97, No. 2, pp. 237—246, 1984.
27. Milne, H. K., “A Note on Beam Reflection Matrices and Reciprocity”, *Journal of Sound and Vibration*, Vol. 114, No. 1, pp. 149–151, 1987.
28. Mei, C. and B. R. Mace, “Wave Reflection and Transmission in Timoshenko Beams and Wave Analysis of Timoshenko Beam Structures”, *Journal of Vibration and Acoustics*, Vol. 127, No. 4, pp. 382–394, 2005.
29. Doyle, J. F. and S. Kamle, “An Experimental Study of the Reflection and Transmission of Flexural Waves at Discontinuities”, *Journal of Applied Mechanics*, Vol. 52, No. 3, pp. 669–673, 1985.

30. Doyle, J. F. and S. Kamle, “An Experimental Study of the Reflection and Transmission of Flexural Waves at an Arbitrary T-Joint”, *Journal of Applied Mechanics*, Vol. 54, No. 1, pp. 136–140, 1987.
31. Mei, C., “Comparison of the Four Rod Theories of Longitudinally Vibrating Rods”, *Journal of Vibration and Control*, Vol. 21, No. 8, pp. 1639–1656, 2015.
32. Nagem, R. J. and J. H. W. Jr., “Dynamic Analysis of Large Space Structures Using Transfer Matrices and Joint Coupling Matrices”, *Journal of Structural Mechanics*, Vol. 17, No. 3, pp. 349–371, 1989.
33. Howard, S. M. and Y.-H. Pao, “Analysis and Experiments on Stress Waves in Planar Trusses”, *Journal of Engineering Mechanics*, Vol. 124, No. 8, pp. 884–891, 1998.
34. Mace, B. R., D. Duhamel, M. J. Brennan and L. Hinke, “Finite Element Prediction of Wave Motion in Structural Waveguides”, *The Journal of the Acoustical Society of America*, Vol. 117, No. 5, pp. 2835–2843, 2005.
35. Waki, Y., B. R. Mace and M. J. Brennan, “Free and Forced Vibrations of a Tyre Using a Wave/Finite Element Approach”, *Journal of Sound and Vibration*, Vol. 323, No. 3–5, pp. 737–756, 2009.
36. Flotow, A. H. V., “Disturbance Propagation in Structural Networks”, *Journal of Sound and Vibration*, Vol. 106, No. 3, pp. 433–450, 1986.
37. Miller, D. V. and A. H. V. Flotow, “A Travelling Wave Approach to Power Flow in Structural Networks”, *Journal of Sound and Vibration*, Vol. 128, No. 1, pp. 145–162, 1989.
38. Beale, L. S. and M. L. Accorsi, “Power Flow in Two- and Three Dimensional Frame Structures”, *Journal of Sound and Vibration*, Vol. 185, No. 4, pp. 685–702, 1995.

39. Housner, G. W., “Limit Design of Structures to Resist Earthquakes”, *Proceedings of the First World Conference on Earthquake Engineering*, pp. 5.1–5.13, 1956.
40. Akiyama, H., “Earthquake Resistant Design Based on the Energy Concept”, *Proceedings of 9th WCEE*, 1988.
41. Lyon, R. H., *Statistical Energy Analysis*, MIT Press, Cambridge, MA, USA, 1975.
42. Carcaterra, A. and A. Sestieri, “Energy Density Equations and Power Flow in Structures”, *Journal of Sound and Vibration*, Vol. 188, No. 2, pp. 269–282, 1995.
43. Wohlever, J. C. and R. J. Bernhard, “Mechanical Energy Flow Models of Rods and Beams”, *Journal of Sound and Vibration*, Vol. 153, No. 1, pp. 1–19, 1992.
44. Lase, Y., M. N. Ichchou and L. Jezequel, “Energy Flow Analysis of Bars and Beams: Theoretical Formulations”, *Journal of Sound and Vibration*, Vol. 192, No. 1, pp. 281–305, 1996.
45. Ichchou, M. N., A. L. Bot and L. Jezequel, “Energy Models of One-Dimensional, Multi-Propagative Systems”, *Journal of Sound and Vibration*, Vol. 201, No. 5, pp. 535–554, 1997.
46. Mace, B. R. and P. J. Shorter, “Energy Flow Models From Finite Element Analysis”, *Journal of Sound and Vibration*, Vol. 233, No. 3, pp. 369–389, 2000.
47. Park, Y.-H. and S.-Y. Hong, “Vibrational Energy Flow Analysis of Corrected Flexural Waves in Timoshenko Beam—Part I: Theory of an Energetic Model”, *Shock and Vibration*, Vol. 13, No. 3, pp. 137–165, 2006.
48. Kausel, E., “Early History of Soil–Structure Interaction”, *Soil Dynamics and Earthquake Engineering*, Vol. 30, No. 9, pp. 822–832, 2010.
49. Gazetas, G., “Analysis of Machine Foundation Vibrations: State of the Art”, *International Journal of Soil Dynamics and Earthquake Engineering*, Vol. 2, No. 1,

pp. 2–42, 1983.

50. Stewart, J. P., G. L. Fenves and R. B. Seed, “Seismic soil-structure interaction in buildings. I: Analytical methods”, *Journal of Geotechnical and Geoenvironmental Engineering*, Vol. 125, No. 1, pp. 26–37, 1999.
51. Gazetas, G., “Formulas and Charts for Impedances of Surface and Embedded Foundations”, *Journal of Geotechnical Engineering*, Vol. 117, No. 9, pp. 1363–1381, 1991.
52. Mylonakis, G., S. Nikolaou and G. Gazetas., “Footings Under Seismic Loading: Analysis and Design Issues with Emphasis on Bridge Foundations”, *Soil Dynamics and Earthquake Engineering*, Vol. 26, No. 9, pp. 824–853, 2006.
53. Sieffert, J. G. and F. Cevaer, *Manuel des Fonctions d’Impedance, Fondations Superficielles*, Ouest Editions, Presses Academiques, France, 1992.